

Proton-Conducting Copolymers, Blends and Composites with Phosphonic Acid as Protogenic Group

Dissertation

zur Erlangung des Grades

Doktor der Naturwissenschaften

am Fachbereich Chemie,

Pharmazie und Geowissenschaften

der Johannes Gutenberg-Universität Mainz

vorgelegt von

Fengjing Jiang

geboren in Zhejiang (P. R. China)

Mainz, 2009

LIST OF ABBREVIATIONS

Chemicals

4VP	4-vinyl pyridine
BA	composite of SiO ₂ -Cl-4VP and PVPA
DIPVBP	diisopropyl-p-vinylbenzyl phosphonate
HMTETA	N,N,N',N'',N''',N''''-hexamethyltriethylenetetramine
Me ₆ TREN	Tris[2-(dimethylamino)ethyl]amine
P4VP	poly(4-vinyl pyridine)
PBI	polybenzimidazole
PEO	polyethylene oxide
PVPA	poly(vinyl phosphonic acid)
PVPE	Blends of PEO and PVPA
PVBPA	poly(vinylbenzyl phosphonic acid)
PVBPE	Poly(diisopropyl-p-vinylbenzyl phosphonate)
PMDETA	N,N,N',N'',N''-pentamethyldiethylenetriamine
VBPA	vinylbenzyl phosphonic acid
VPA	vinyl phosphonic acid

Methods and related acronyms

DSC	Differential scanning calorimetry
EA	Elemental analysis

FTIR	Fourier transfer infrared spectroscopy
GPC	gel permeation chromatography
^{13}C NMR	^{13}C nuclear magnetic resonance spectroscopy
^1H -NMR	^1H nuclear magnetic resonance spectroscopy
^1H -MAS-NMR	^1H magic-angle-spin NMR
^{31}P -MAS-NMR	^{31}P magic-angle-spin NMR
PFG-NMR	Pulsed-field gradient NMR
SEM	Scanning electron microscopy
TEM	Transmission electron microscopy
TGA	Thermal Gravimetric Analysis
XRD	X-ray diffraction
WAXS	wide angle x-ray scattering

ABSTRACT

In this work, proton conducting copolymers, polymer blends and composites containing phosphonic acid groups have been prepared. Proton conduction mechanisms in these materials are discussed respectively in both, the anhydrous and humidified state.

Atom transfer radical copolymerization (ATRCP) of diisopropyl-p-vinylbenzyl phosphonate (DIPVBP) and 4-vinyl pyridine (4VP) is studied for the first time in this work. The kinetic parameters are obtained by using the $^1\text{H-NMR}$ online technique. Proton-conducting statistical copolymers (poly(vinylbenzyl phosphonic acid-stat-4VP)) are then successfully obtained by complete hydrolysis of the phosphonate groups. Proton conduction in poly(vinylbenzyl phosphonic acid) (PVBPA) homopolymer and its statistical copolymers with 4-vinyl pyridine (poly(VBPA-stat-4VP)s) are comprehensively studied in both, the “dry” and “wet” state. Effects of temperature, water content and polymer composition on proton conductivities are studied and proton transport mechanisms under various conditions are discussed. The proton conductivity of the polymers is in the range of 10^{-6} - 10^{-8} S/cm in nominally dry state at 150°C . However, proton conductivity of the polymers increases rapidly with water content in the polymers which can reach 10^{-2} S/cm at the water uptake of 25% in the polymers. The highest proton conductivity obtained from the polymers can even reach 0.3 S/cm which was measured at 85°C with 80% relative humidity in the measuring atmosphere.

Self-condensation of the phosphonic acid groups has been quantified with ^{31}P -MAS-NMR. Proton exchanges between water molecules, phosphonic acid moieties and pyridine groups are determined by ^1H -MAS-NMR.

Poly(4-vinyl pyridine) was grafted from the surface of SiO_2 nanoparticles using ATRP in this work for the first time. Following this approach, silica nanoparticles with a shell of polymeric layer are used as basic particles in a polymeric acidic matrix. The proton conductivities of the composites are studied under both, humidified and dry conditions. In dry state, the conductivity of the composites is in the range of $10^{-10}\sim 10^{-4}$ S/cm at 150 °C. While in humid state, the composites show much higher proton conductivity. The highest proton conductivity obtained with the composites is 0.5 S/cm measured at 85°C with 80% relative humidity in the measuring atmosphere.

The ratio of protons solvated by pyridine moieties are quantitatively determined by ^1H -MAS-NMR. The effect of blending on proton conduction is discussed on the basis of both activation energy and charge carrier concentration.

The miscibility of poly (vinyl phosphonic acid) and PEO is studied for the first time in this work and a phase diagram is plotted based on a DSC study and optical microscopy. With this knowledge, homogeneous PVPA/PEO mixtures are prepared as proton-conducting polymer blends. The mobility of phosphonic acid groups and PEO in the blends is determined by ^1H -MAS-NMR in temperature dependent measurements. The effect of composition and the role of PEO on proton conduction are discussed.

TABLE OF CONTENTS

1. INTRODUCTION.....	1
1.1 Introduction	1
1.2 Types of fuel cells.....	1
1.2.1 Polymer electrolyte membrane fuel cell (PEMFC)	2
1.2.2 Solid oxide fuel cell (SOFC)	3
1.2.3 Alkaline fuel cell (AFC)	4
1.2.4 Molten-carbonate fuel cell (MCFC)	4
1.2.5 Phosphoric-acid fuel cell (PAFC)	4
1.2.6 Direct-methanol fuel cell (DMFC)	5
1.3 Polymer electrolyte membrane (PEM) for fuel cells.....	5
1.3.1 Ionomer membrane for fuel cells.....	6
1.3.2 Developments on intermediate temperature PEMs	11
1.4 Mechanisms of proton transport.....	18
1.4.1 Structure diffusion in water and aqueous solutions	19
1.4.2 Structure diffusion in imidazole	20
1.4.3 Structure diffusion in phosphonic acid	21
2. MOTIVATION	23
3. ATOM TRANSFER RADICAL COPOLYMERIZATION OF DIISOPROPYL-P-VINYLBENZYL PHOSPHONATE AND 4-VINYL PYRIDINE.....	27
3.1 Introduction	27
3.2 Monomer Conversion.....	30
3.3 ATRCP of DIPVBP and 4VP	32
3.4 Monomer Reactivity Ratio Determination	35

3.5 DIPVBP-stat-4VP Copolymers	37
3.5.1 Solution ¹ H NMR spectra	37
3.5.2 Copolymer Compositions	38
3.5.3 Molecular weight and polydispersity	40
3.6 Hydrolysis of DIPVBP-stat-4VP copolymers	40
3.7 Thermal analysis.....	42
4. PROTON CONDUCTION IN VINYL BENZYL PHOSPHONIC ACID - 4-VINYL PYRIDINE COPOLYMERS.....	43
4.1 Introduction	43
4.2 Characterization of PVBPA and Poly(VBPA-stat-4VP)s	44
4.2.1 Water Sorption	44
4.2.2 Anhydride content	46
4.3 Temperature dependence of proton conductivity.....	47
4.3.1 Proton conduction under dry conditions.....	53
4.3.2 Proton conduction under humidification	58
4.3.3 Proton conduction of Copo3 blended with phosphoric acid.....	62
5. PROTON CONDUCTION IN BLENDS OF PVPA AND P4VP GRAFTED SILICA NANOPARTICLES	66
5.1 Introduction	66
5.2 Poly(4-vinyl pyridine) grafting from silica nanoparticles	68
5.2.1 Initiator immobilization.....	69
5.2.2 ATRP of 4VP grafting from silica nanoparticles	72
5.2.3 Characterization of SiO ₂ -Br-4VP and SiO ₂ -Cl-4VP.....	74
5.3 Proton conduction in the blends of SiO ₂ -Cl-4VP and PVPA.....	78
5.3.1 Proton conduction under dry conditions.....	78
5.3.2 Proton conduction with humidification	86

6. PHASE BEHAVIOR AND PROTON CONDUCTION OF PVPA/PEO BLENDS	89
6.1 Introduction	89
6.2 Thermal analysis of PVPA and PEO blends	92
6.3 Phase diagram of PVPA and PEO blends	100
6.3.1 Phase separation observed by optical microscopy	100
6.3.2 Phase separation observed by DSC	103
6.4 Proton Magic-Angle-Spinning NMR	108
6.5 Proton conduction of PVPA/PEO blends	115
7. SUMMARY	121
8. EXPERIMENTAL	124
8.1 Materials	124
8.2 Preparation of poly(vinylbenzyl phosphonic acid).....	125
8.2.1 Synthesis of DIPVBP	125
8.2.2 Atom transfer radical polymerization of VBPE and hydrolysis of PVBPE	126
8.3 Atom Transfer Radical Copolymerization.....	127
8.4 Preparation of poly(vinylbenzyl phosphonic acid-stat-4VP)	128
8.5 Initiator synthesis and immobilization	128
8.5.1 Synthesis and immobilization of (3-(2-Bromoisobutyryl)propyl)dimethyl chlorosilane.....	128
8.5.2 Immobilization of 4-(chloromethyl)phenyltrichlorosilane	130
8.6 ATRP of 4-vinyl pyridine grafting from silica nanoparticles	130
8.7 Characterization.....	131
8.7.1 Gel Permeation Chromatography (GPC).....	131
8.7.2 Nuclear Magnetic Resonance (NMR)	131
8.7.3 Thermal Gravimetric Analysis (TGA).....	132
8.7.4 Differential Scanning Calorimetric (DSC)	132

8.7.5 Optical microscopy.....	132
8.7.6 Elemental analysis (EA).....	132
8.7.7 Infrared spectroscopy	133
8.7.8 Electron microscopy.....	133
8.7.9 Proton Conductivity Measurements	133
References.....	136
Acknowledgements.....	146

CHAPTER 1

INTRODUCTION

1.1 Introduction

Nowadays, energy shortage is a severe problem due to the limitation of fossil energy and steadily increasing energy demand.

Fuel cells have the potential to be an important alternative energy conversion technology due to the properties such as high energy density, high efficiency, and environmental friendliness. The theoretical efficiency of fuel cells is around 90% which is substantially higher than that of a combustion engine. One of the most attractive benefits of fuel cells is that they can produce clean energy from renewable sources.

1.2 Types of fuel cells

Fuel cells are classified primarily by the kind of electrolyte they employ which determine the kind of chemical reactions that take place in the cell, the kind of catalysts required, the temperature range in which the cell operates, the fuel which is used, and other factors. These characteristics, in turn, affect the applications for which these cells are most suitable. Some types of fuel cells work well for small portable applications or for powering cars. Others may be useful for use in stationary power generation plants. There are several types of fuel cells currently under development,

each with its own advantages, limitations, and potential applications. A few of the most promising types of fuel cells include:

1.2.1 Polymer electrolyte membrane fuel cell (PEMFC)

PEMFC ^[1-3] is the most likely candidate for transportation applications. The PEMFC has a high power density and a relatively low operating temperature (ranging from 20 to 100 °C). The low operating temperature means that the PEMFC is self-starting without the need of external warm up and readily generating electricity which makes it particularly promising.

A hydrogen-powered PEMFC consists of two electrodes and a separator polymer membrane as shown in Fig 1.1.

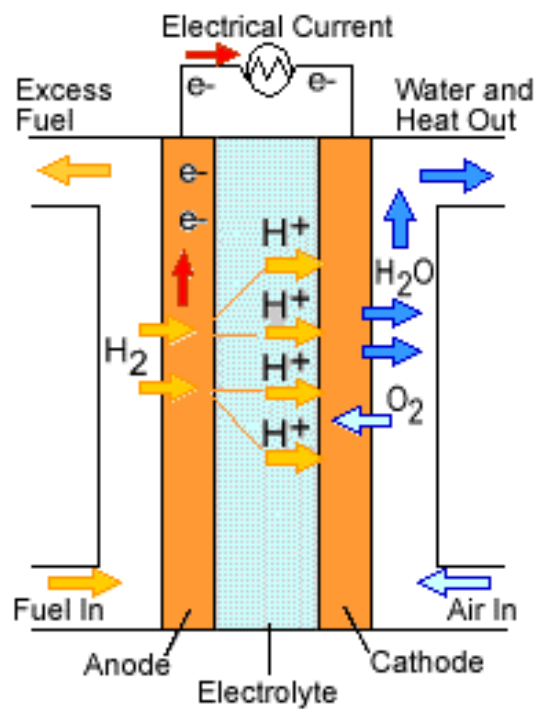
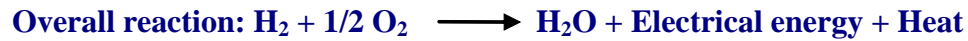
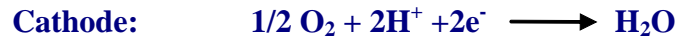
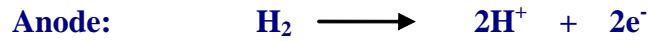


Fig. 1.1: Polymer Electrolyte Membrane Fuel Cell (PEMFC)

Hydrogen is supplied to the anode and air is channeled to the cathode. The electrochemical reactions taking place at the electrodes are:



At the anode, a platinum catalyst causes the hydrogen to split into positive hydrogen ions (protons) and negatively charged electrons. The polymer electrolyte membrane (PEM) allows only the protons to pass through it to the cathode. The electrons travel along an external circuit to the cathode, creating an electrical current. At the cathode, the electrons and protons combine with oxygen to form water which is the only waste product of hydrogen fueled PEMFCs.

1.2.2 Solid oxide fuel cell (SOFC)

Solid oxide fuel cells ^[4] are best suited for stationary power generators that could provide electricity and heat for houses, factories or towns. This type of fuel cell operates at very high temperatures (between 700 and 1000 °C). This high temperature makes reliability a problem, because parts of the fuel cell can break down after cycling on and off repeatedly. However, solid oxide fuel cells are very stable under continuous use. In fact, the SOFC has demonstrated the longest operating life of any fuel cell under certain operating conditions. The high temperature also has an advantage: the steam produced by the fuel cell can be channeled into turbines to generate more electricity and the heat can be used for heating purposes. This process

is called co-generation of heat and power and it improves the overall efficiency of the system.

1.2.3 Alkaline fuel cell (AFC)

Alkaline fuel cell ^[5] is one of the oldest designs for fuel cells; the United States space program has used them since the 1960s. The AFC is very susceptible to contamination, so it requires pure hydrogen and oxygen.

Alkaline fuel cells use an aqueous solution of potassium hydroxide in a porous stabilized matrix as an electrolyte. The operating temperature ranges from 65 to 200 °C. It is also very expensive, so this type of fuel cell is unlikely to be commercialized, but research has revisited this type of fuel cells recently again.

1.2.4 Molten-carbonate fuel cell (MCFC)

Like the SOFC, molten-carbonate fuel cells ^[6] are also best suited for large stationary power generators. The fuel cells use molten alkaline carbonate (e.g., sodium bicarbonate NaHCO_3) as electrolyte. They operate at 600 °C, so they can generate steam that can be used to improve the overall efficiency. They have a lower operating temperature than solid oxide fuel cells, which means they don't need such exotic materials. This makes the design a little less expensive.

1.2.5 Phosphoric-acid fuel cell (PAFC)

The phosphoric-acid fuel cell ^[7] has its potential use in small stationary

power-generation systems.

The fuel cells use molten phosphoric acid (H_3PO_4) as electrolyte. The operating temperatures of the fuel cell would be around 150 to 200 °C. It operates at a higher temperature than polymer electrolyte membrane fuel cells, so it has a longer warm-up time. This makes it unsuitable for use in cars.

1.2.6 Direct-methanol fuel cell (DMFC)

Methanol fuel cells ^[8] are comparable to a PEMFC in regards to its operating temperature (90-120 °C), but yet are not as efficient. They use a polymer membrane as electrolyte. Also, the DMFC requires a relatively large amount of platinum to act as a catalyst, which makes these fuel cells expensive. Methanol as fuel must be reformed to yield H_2 prior to the electrochemical processes. This is also true for the use of natural gas. Yet the PEMs are not sufficiently tight, methanol crossover is a problem.

1.3 Polymer electrolyte membrane (PEM) for fuel cells

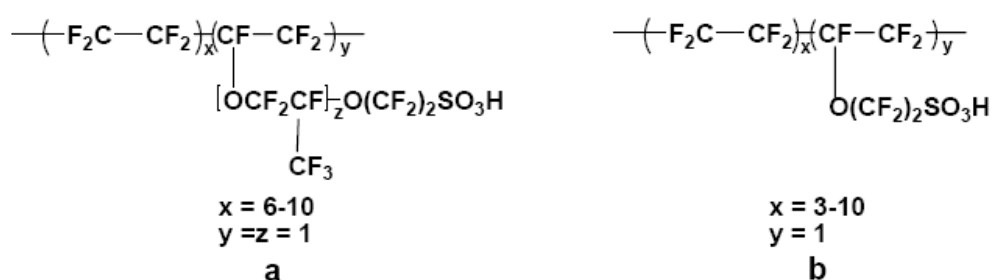
The Membrane-electrode-assembly (MEA) is the electrochemical heart of any fuel cell. The anode and cathode gases or liquids need to be effectively separated by the PEM. A PEM needs to be a good electronic isolator and a proton conductor. Different applications have different requirements for PEMs. General issues which are critical to a high performance of the PEM include ^[9-13]:

- (1) High proton conductivity
- (2) Low water diffusion and electro-osmosis

- (3) Low permeability of fuel and oxidant
- (4) Reduced thermally or impurity induced instability
- (5) Good mechanical properties. The membrane in a fuel cell suffers from the stress which caused by the swelling and deswelling of the membrane in humidity.
- (6) Low cost and environmental friendly

1.3.1 Ionomer membrane for fuel cells

The current state-of-the-art proton electrolyte membranes are perfluorinated sulfonic acid ionomers such as Nafion[®] or Dow[®]. The chemical structure of Nafion[®] and Dow[®] are illustrated in Scheme 1.1.



Scheme 1.1: Chemical structure of (a) Nafion[®] and (b) Dow[®].

Nafion is an ionomer discovered in the late 1960s by Walther Grot of DuPont de Nemours. It belongs to a class of synthetic polymers with ionic properties which are called ionomers. Nafion's unique ionic properties are a result of incorporating perfluorovinyl ether groups terminated with sulfonic acid groups onto a tetrafluoroethylene backbone. Nafion has received a considerable amount of attention as a proton conductor for proton electrolyte membrane (PEM) fuel cells because of its

excellent thermal and mechanical stability.^[14, 15]

Trifluoromethanesulfonic acid ($\text{CF}_3\text{SO}_3\text{H}$) is a superacid. A superacid is an acid with acidity greater than that of 100% sulfuric acid. Trifluoromethanesulfonic acid is about a thousand times stronger than sulfuric acid. The combination of the stable hydrophobic perfluorinated hydrocarbon backbone with the sulfonic acid groups gives Nafion its characteristics:

It is highly conductive for cations, making it suitable for many membrane applications. The chemical basis of Nafion's superior conductive properties remains a focus of research.

It resists chemical attack. According to DuPont, only alkali metals (particularly sodium) can degrade Nafion under normal temperatures and pressures.

It is swellable and highly permeable to water. The higher the degree of hydration of the Nafion membrane is, the higher the ion permeability.

The morphology of Nafion membranes is a matter of continuing study to allow for greater control of its properties. The unique morphology of Nafion membrane is a result of the combination of the extremely hydrophobic polymer backbone with the extremely hydrophilic sulfonic acid functional groups, which leads to a hydrophilic/hydrophobic phase separation on the nano-scale (Figure 1.2).^[16] When the material comes in contact with water, the hydrophilic domains spontaneously take up water and swell to form nanochannels with a liquid water phase. These nanochannels are formed by the aggregation of sulfonic acid functional groups and are responsible for the transport of water and protons. In these nanochannels, charge

carriers (Hydronium ions, Zundel ions (H_5O_2^+) and Eigen ions (H_9O_4^+)) are formed by dissociation of the acidic functional groups and the interaction with water, and ion transport takes place through the hydrophilic channels. On the other hand, hydrophobic domains provide the polymer with thermal stability, chemical stability, dimensional stability and insolubility in water.

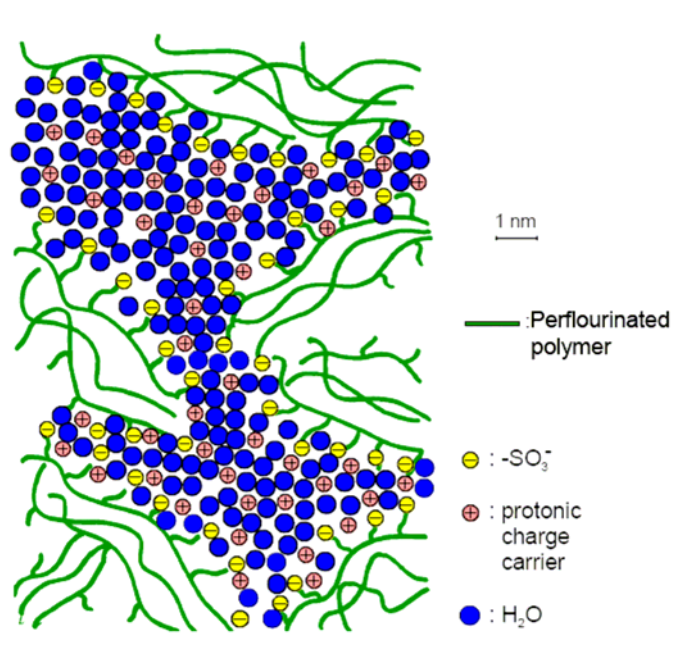


Figure 1.2: Microstructure of Nafion. ^[16]

Several models have been applied to describe the properties of Nafion in view of membrane morphology. ^[17-21] The first model for Nafion, called the Cluster-Channel or Cluster-Network model, consisted of an equal distribution of sulfonate ion clusters (also described as inverted micelles) with a 40 Å (4 nm) diameter held within a continuous fluorocarbon matrix. Narrow channels about 10 Å (1 nm) in diameter interconnect the clusters, which explains the transport properties. ^[17] Several other models for the morphology of Nafion which have been proposed including a modified

core-shell model ^[18], a lamellar model ^[19] and a rodlike model ^[20]. Recently, Schmidt-Rohr et al. found that in hydrated Nafion, there are long, parallel but otherwise randomly packed water channels surrounded by the partially hydrophilic sidebranches, forming inverted micelle cylinders (see Figure 1.3). The channels are stabilized by the considerable rigidity of helical Nafion backbones. ^[21]

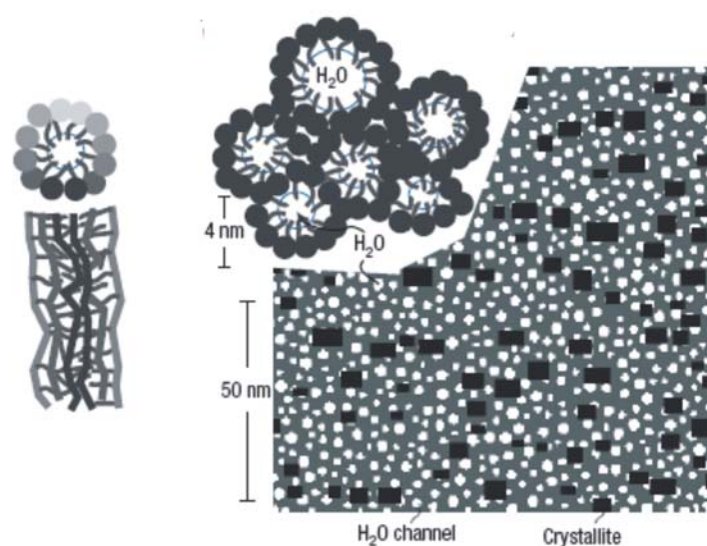


Figure 1.3: Inverted-micelle cylinder (water channel) model of Nafion. ^[21]

The difficulty in determining the exact structure of Nafion stems from insufficient solubility and ill-defined order with long range. More recent morphological models have included a core-shell model where the ion-rich core is surrounded by an ion poor shell, a rod model where the sulfonic groups arrange into crystal-like rods, and a sandwich model where the polymer forms two layers whose sulfonic groups attract across an aqueous layer where transport occurs. ^[22] Consistency between the models includes a network of ionic clusters; the models differ in the cluster geometry and distribution. Although no model was yet shown to be fully correct, some scientists

have demonstrated that as the membrane hydrates, Nafion's morphology transforms from the Cluster-Channel model to a rod-like model. [22]

Due to the high cost of Nafion, great efforts have been made to provide cheaper alternative sulfonated polymers. Some of the works are selectively listed in Table 1.1.

Table 1.1: Selected sulfonated polymers for PEMs

Sulfonated Polymer	Chemical Structure	Ref.
BAM [®]	<p style="text-align: center;">$(-\text{CF}_2\text{CF}-)_{\text{a}} (\text{CF}_2\text{CF}-)_{\text{b}} (\text{CF}_2\text{CF}-)_{\text{c}} (\text{CF}_2\text{CF}-)_{\text{d}}$</p> <p style="text-align: center;">$\text{R}_1, \text{R}_2, \text{R}_3 = \text{alkyls, halogens, OR, CF}=\text{CF}_2, \text{CN, NO}_2, \text{OH}$</p>	[23]
Sulfonated styrene ethylene-butylene-styrene (SEBS)		[24]
Sulfonated poly(arylene ether)s	<p style="text-align: center;">$\text{X} = \text{O, S}$</p> <p style="text-align: center;">$\text{Y} = \text{a bond, SO}_2, \text{-C(CH}_3\text{)}_2\text{-, -C(CF}_3\text{)}_2\text{-, -P(=O)(C}_6\text{H}_5\text{)-}$</p> <p style="text-align: center;">$\text{Z} = \text{SO}_2, \text{-C(=O)-, -P(=O)(C}_6\text{H}_5\text{)-}$</p> <p style="text-align: right;">[*]</p>	[25]
Sulfonated poly(imide)s		[26]
		[27]

*These are the chemical structures of poly(arylene ether)s before sulfonation. After postsulfonation of the existing polymer, partially sulfonated poly(arylene ether)s can be obtained.

The conductivity of sulfonated membranes is dependent on the presence of water to solvate the protons dissociated from the sulfonic acid groups. Consequently, the operating temperature is limited to below the boiling point of water (100 °C), typically 60-90 °C, at atmospheric pressure. This is a severe drawback because the use of a polymer membrane electrolyte at temperatures above 100 °C is desirable for several reasons. Firstly, the reaction kinetics is enhanced and the catalytic activity increased at higher temperatures for both electrodes. Secondly, there is reduced poisoning of catalysts by fuel impurities such as carbon monoxide (CO). This poisoning effect has been shown to be very temperature-dependent; that is, CO adsorption is less pronounced with increasing temperature.^[31]

1.3.2 Developments on intermediate temperature PEMs

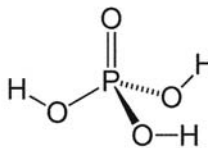
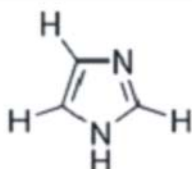
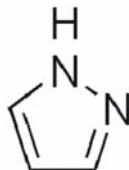
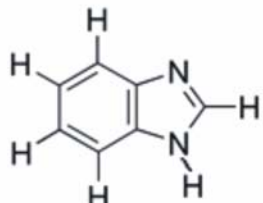
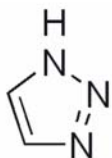
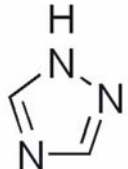
Because the high proton conductivity of a hydrated PEM is predominantly dependent on adequate amount of water in the membrane, the operating temperature is limited by the boiling point of water. A proton-conducting polyelectrolyte that can provide high proton conductivity at high temperatures (120-150°C) in a low humidity environment is considered to be a promising progress in PEMFC technology.

A molecule that can be used as a proton solvent alternative to water should present several specific characteristics. First of all, it should have a higher boiling point than water. Secondly, it should be amphoteric in the sense that it can behave both as a protogenic group and proton acceptor group, a property, which can be expressed in terms of the pKa value, which defines the self-dissociation of the

molecule. Thirdly, it must form a dynamic hydrogen bond network which is important for fast proton transport (details will be discussed in section 1.4).

Typical amphoteric molecules are phosphoric acid and heterocycles such as imidazole, pyrazole, benzimidazole and triazole. The chemical structures are shown in Table 1.2 respectively.

Table 1.2: Chemical structures of typical amphoteric molecules

Proton Solvent	Chemical Structure
Phosphoric acid	
Imidazole	
Pyrazole	
Benzimidazole	
Triazole	<div style="display: flex; justify-content: space-around; align-items: center;"> <div style="text-align: center;">  <p>1,2,3- triazole</p> </div> <div style="text-align: center;">  <p>1,2,4- triazole</p> </div> </div>

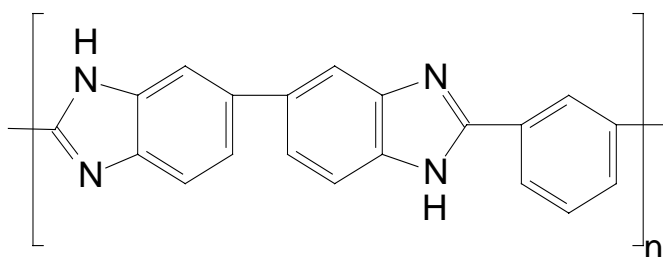
They all have quite high proton conductivity in the liquid state. Kreuer et al. [32] claimed that most of the proton transport takes place by hydrogen bond breaking and forming processes. For instance, the proton transport in imidazole via bond breaking and forming processes are shown in Figure 1.4 which were proposed by Daycock [33] and Kawala. [34] In Daycock's model, the proton transfer step takes place through hydrogen bonds as a cooperative process, while in Kawala's model, the proton transfer step happens by charge migrating through hydrogen bonds. The reorientation step in both models involves a coherent rotation of all the imidazole molecules in the hydrogen bonded chains to achieve the long-range transport of protons.

Among these amphoteric proton solvents, imidazole and phosphoric acid are considered to be the most promising substitutes due to their high intrinsic proton conductivity. For pure imidazole at the melting point of $T_m=90\text{ }^\circ\text{C}$, the proton conductivity reaches 10^{-3} S/cm . [34] The conductivity of phosphoric acid at the melting point ($T=42\text{ }^\circ\text{C}$) is $7.7\times 10^{-2}\text{ S/cm}$. [35]

The state of the art in phosphoric acid based PEM is polybenzimidazole (PBI) doped with phosphoric acid. PBI (Scheme 1.2) is considered to be relatively rigid and thermally very stable and has both proton donor and acceptor sites. It is an amorphous polymer with a reported glass transition temperature of $420\text{ }^\circ\text{C}$. [36] The H_3PO_4 blended PBI exhibits an excellent thermal stability. It also shows good conductivities even at low water contents. [37, 38] Originally, the term "doping" is the process of intentionally introducing impurities into an extremely pure semiconductor to change

its electrical properties. In this chapter, phosphoric acid doped with PBI means PBI swollen with phosphoric acid.

However, PEM on the basis of doping with imidazole or phosphoric acid has the problem of draining of from the membrane body during fuel cell operation. [39]



Scheme 1.2: Chemical structure of polybenzimidazole

Immobilization of imidazole or phosphonic acid residues has been proposed to eliminate the draining out of proton solvents. Because of the hydrolytic sensitivity of the P-O-C bond (the O-C bond is sensitive to acid and can be easily hydrolyzed), phosphonic acid ($\text{HPO}(\text{OH})_2$), which also has high intrinsic proton conductivity, has been tethered to some polymeric backbones as a replacement of phosphoric acid. Many imidazole-based and phosphoric acid-based oligomers have firstly been made to investigate their intrinsic proton conductivities. [40-45] Some typical compounds and their proton conductivities are listed in Figure 1.5.

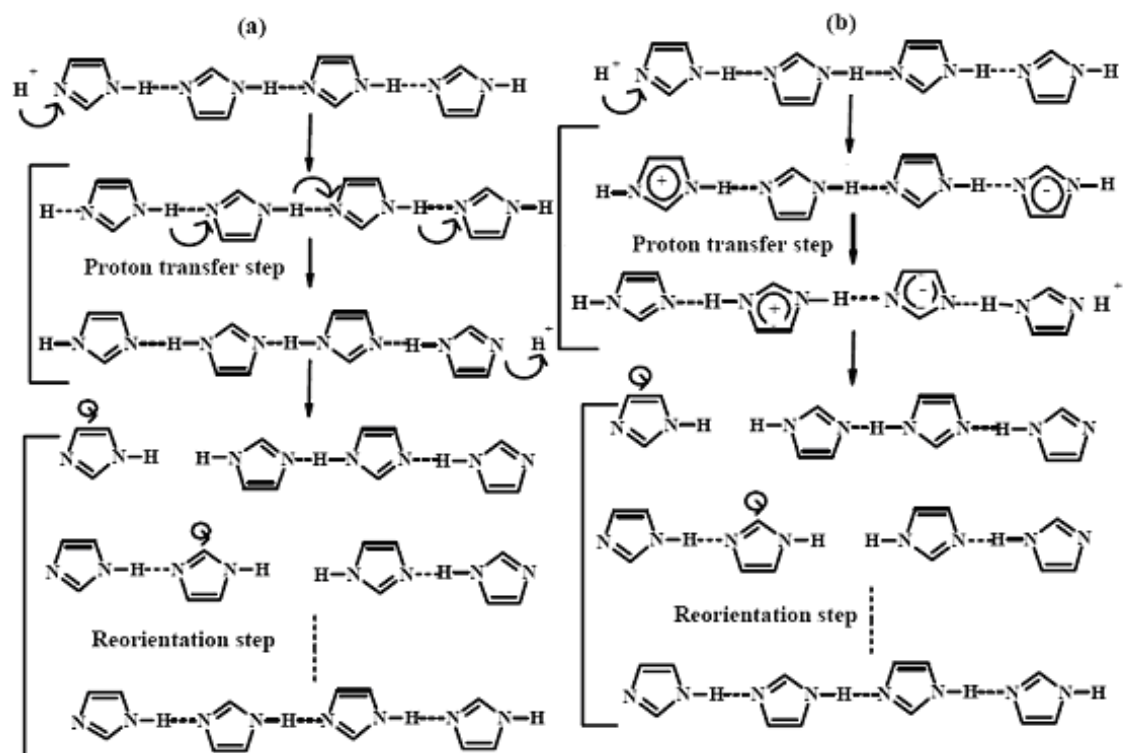


Figure 1.4: The proton transfer process as proposed (a) by Daycock (b) by Kawala.

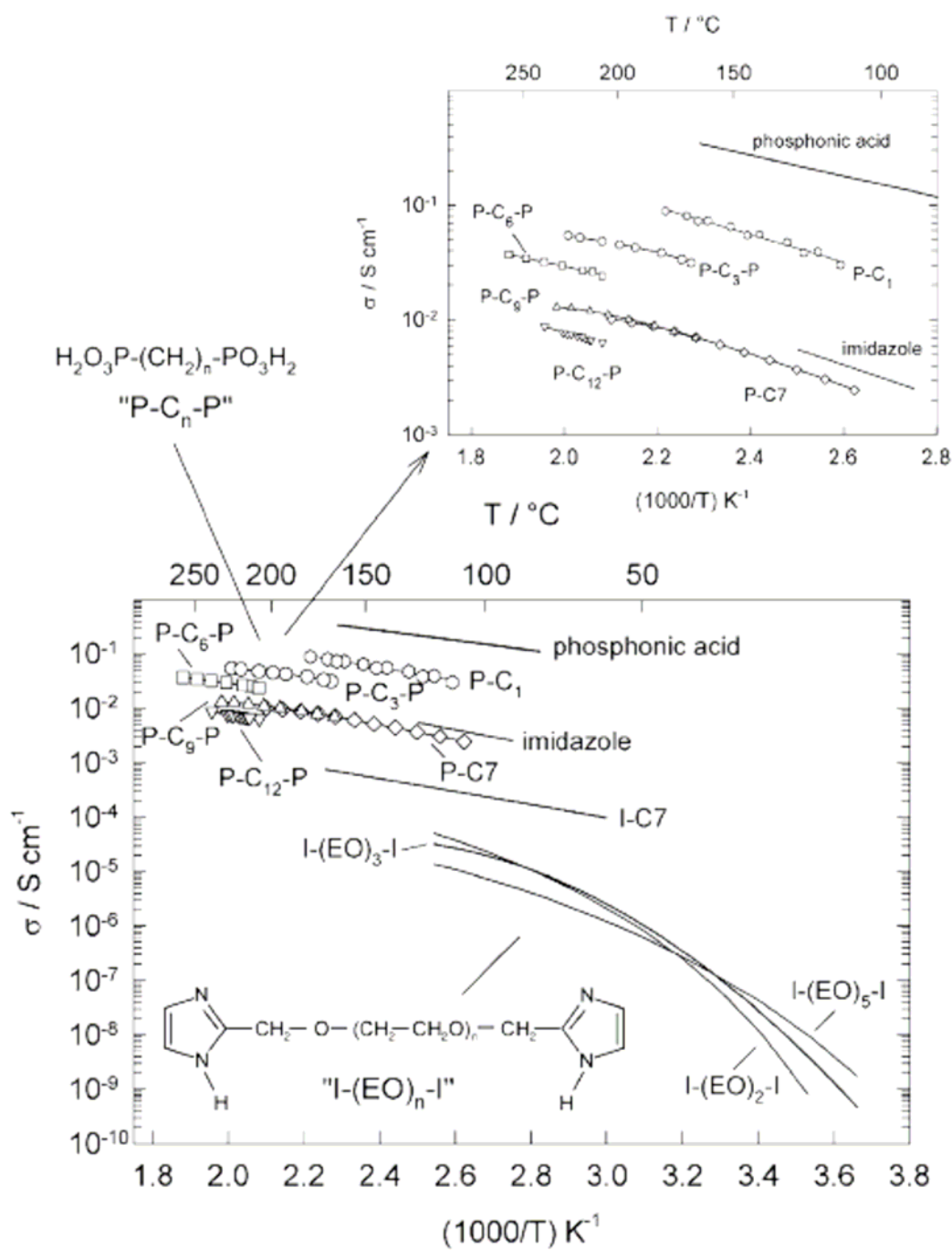
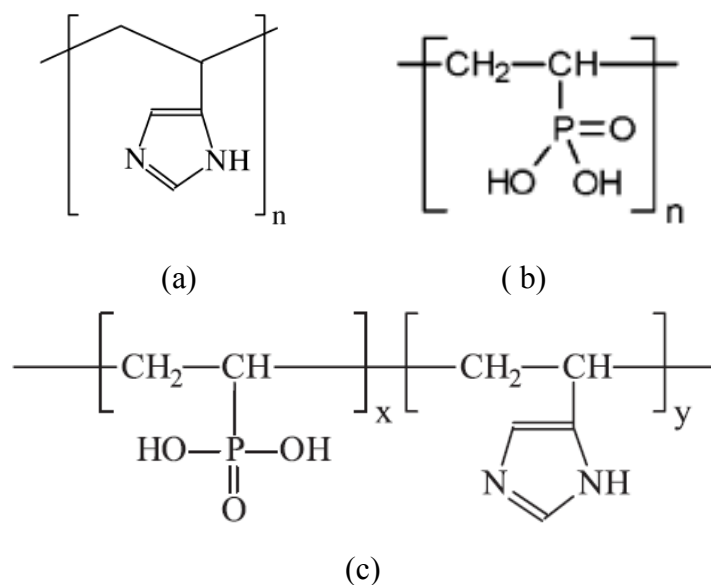


Fig 1.5: Ionic conductivities of different hydrocarbon molecules functionalized with one or two phosphonic acid groups in the liquid state as obtained by ac-impedance spectroscopy. The conductivities of imidazole functionalized molecules, and neat phosphonic acid and imidazole are shown for comparison. ^[46]

Some low molecular weight compounds, especially those containing phosphonic acid moieties, show high proton conductivity in the anhydrous state which proves that tethering a protogenic group to a spacer does not disturb the chemical interaction of the proton donor (acid) site and proton acceptor (base) site and still allows for fast proton transfer via hydrogen bond breaking and forming process (structure diffusion). The structure diffusion of protons in imidazole has been discussed in Figure 1.4. However, the steps of structure diffusion in phosphoric acid are not clear yet.

With this in mind, a lot of heterocycle and/or phosphonic acid containing polymers have been prepared with the aim to create solid state PEM for application at intermediate temperatures. Poly(4-vinyl imidazole) (P4VI) was synthesized and studied as a proton conductor by Bozkurt et al.^[47] The proton conductivity of pure P4VI turned out to be very low under anhydrous conditions (lower than 10^{-10} S/cm). The proton conductivity of the anhydrous copolymer of vinyl pyridine and 4-vinyl imidazole was also reported and conductivities were quoted to range from 10^{-6} - 10^{-12} S/cm.^[48] Bingöl et al have investigated the proton conductivity of poly(vinyl phosphonic acid) (PVPA) under dry conditions.^[49] The highest proton conductivity of nominally dry PVPA was around 10^{-4} S/cm at 150 °C and time dependent proton conductivities were observed. “Time dependent proton conductivities” means that proton conductivity changes with measuring time due to the loss of solvent or the formation of anhydride during the measurement.



Scheme 1.3: Molecular structure of poly((4-vinyl imidazole), Poly(vinyl phosphonic acid) and their copolymer.

1.4 Mechanisms of proton transport

Proton transport can be carried out either by a vehicle mechanism diffusion or by rapid hydrogen bond breaking and forming processes (structure diffusion). In the presence of mobile proton solvents such as water, phosphoric acid and heterocycles, both the vehicle mechanism diffusion and the structure diffusion contribute to proton conduction.^[50] Nevertheless, to what extent each mechanism contributes is still difficult to distinguish. But it was demonstrated by Kreuer et al that, in the case of Nafion, this depends on the degree of solvation (λ -value), here, λ refers to the molar ratio of water and sulfonic acid groups.^[50] In a working fuel cell, due to the electric osmotic drag, water diffuse from the anode side to the cathode side together with protons. Additional water need to be supplied on the anode side to maintain the membrane humid. Typically, humid fuel gas is used. As a result, λ fluctuates in the

water swollen polymer.

1.4.1 Structure diffusion in water and aqueous solutions

Proton conduction in water and aqueous solutions have been studied extensively. Proton transport mechanism in water has been discussed. ^[51-53] (see Figure 1.6) The region with a single excess proton within the hydrogen-bond network corresponds to either a Zundel-ion (H_5O_2^+ , one proton complexes with two water molecules) or an Eigen-ion (H_9O_4^+ , one proton complexes with four water molecules). Interestingly, the center of the region of excess charge coincides with the center of symmetry of the hydrogen-bond pattern. ^[54] Therefore, proton diffusion in this case is almost barrierless. There is experimental proof that water has a high self-diffusion coefficient ($2.25 \times 10^{-5} \text{ cm}^2/\text{s}$ at room temperature) and the diffusion of protonated water molecules makes some contribution to the total proton conductivity (vehicle mechanism) which is ~22% when assuming that the diffusion coefficients of water and hydronium (or Zundel) ions are identical. ^[50] Kreuer et al. demonstrated that the contribution of vehicle mechanism diffusion and structure diffusion change with degree of solvation. Figure 1.6 shows the structure diffusion of protons in water. Apart from the bonds with the common shared proton, each water molecule of the Zundel ion acts as a proton donor through two hydrogen bonds; each of the three outer water molecules of the Eigen ion behaves as a proton donor in two hydrogen bonds and as an acceptor for a hydronium ion and an additional water molecule. Through hydrogen-bond breaking and forming processes and displacements of the center of

symmetry in space and, also the center of the region of excess charge, a Zundel ion can be converted to an Eigen ion, which then transfers into one of three possible Zundel ions (see Figure 1.6).

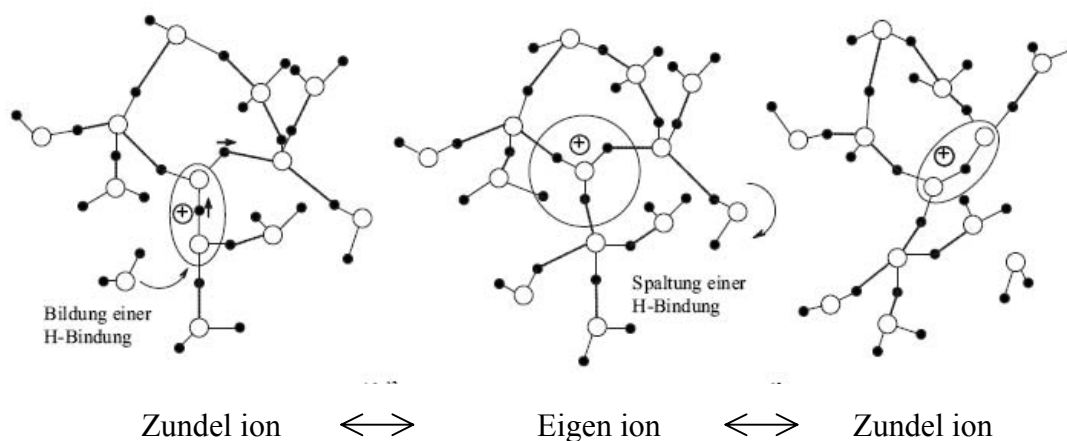


Figure 1.6: Proton transport in water. ^[50]

1.4.2 Structure diffusion in imidazole

Imidazole is a typical amphoteric heterocyclic molecule with both, proton donor and proton acceptor functions. The low barrier hydrogen bonding between the highly polarizable N atoms provides the possibility for fast proton transfer via hydrogen bond breaking and forming processes. The mechanism of proton transport by structure diffusion was first proposed by Daycock and Kawala (see Figure 1.4). Kreuer et al. ^[55] promoted a proton conduction mechanism in liquid imidazole according to a Car-Parrinello molecular dynamics simulation ^[55] (see Figure 1.7)

The proton mobility was found to be a factor of ~ 4.5 higher than the molecule diffusion coefficient at the melting point of imidazole. ^[56] This is a direct indication of

the existence of the structure diffusion in liquid imidazole.

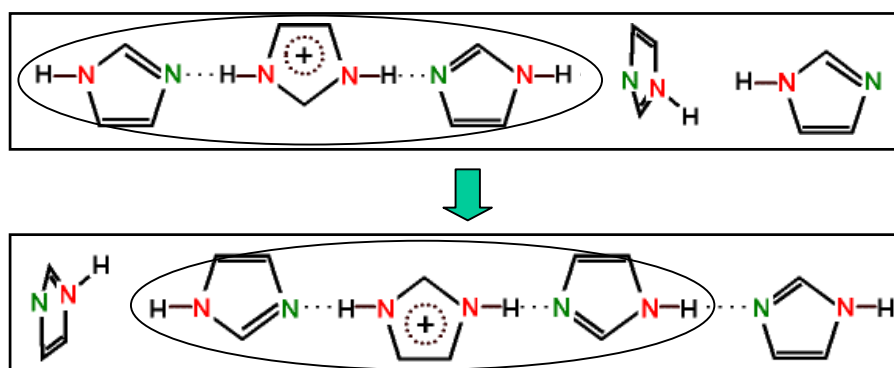


Figure 1.7: Proton transport mechanism in pure liquid imidazole proposed by Kreuer et al. ^[55]

1.4.3 Structure diffusion in phosphonic acid

Pure phosphoric acid (H_3PO_4) is a viscous liquid with a melting point of $T_m=42$ °C. Phosphoric acid shows very high degree of self-dissociation of $\sim 7.4\%$. ^[57] However, the proton conduction mechanism of phosphoric acid yet has not been investigated to the same extent as for water or imidazole.

Nevertheless, the proton mobility has been calculated from the total conductivities by the Nernst-Einstein equation (equation 1.1) which is almost 2 orders of magnitude higher than the diffusion coefficient of phosphate species detected by ^{31}P PFG NMR. ^[35]

$$\frac{\sigma T}{D} = \frac{nq^2}{k} \quad [1.1]$$

where σ is ion conductivity, T is temperature, D is diffusion coefficient of the charge carrier, n is the number of the charge carriers per unit volume, q is the number

of charges per carrier and k is the Boltzmann constant.

The very high proton mobility indicates that proton transfer between phosphate species and structure diffusion must be involved.

CHAPTER 2

MOTIVATION

Making copolymers, composites and polymer blends are powerful techniques which have been widely applied in material science to achieve unique performance like for mechanical, optical, and electrical properties and so on. A more recent but rapidly evolving field in materials science refers to materials to be used for energy production, energy storage and conservation. For all of these, ion conductivity in polymer plays a major role. Although a lot of proton-conducting polymers have been prepared, the knowledge of how protons are transported in those materials is still deficient. Especially in copolymers, organic-inorganic composites and polymer blends, the mechanisms of proton conduction are more complicated. Knowledge needs to be extended as for influences of acid-base interactions and relative humidity on proton conduction, the temperature dependence of proton conductivity, the relation between conductivity and mechanical properties and the effect of morphology and phase separation on proton conduction.

With the purpose of obtaining more information as mentioned above, the following proton-conducting materials will be prepared and more details of proton conduction in these materials will be elucidated:

1. Copolymers. There have been reports on the concept of mixing proton acceptors (like imidazole derivatives) with proton donors like phosphonic acid

derivatives.^[1-5] However, limited knowledge is available on how the composition and acid-base interactions affect the proton conduction in such materials.

In this work, vinylbenzyl phosphonic acid and 4-vinyl pyridine statistical copolymers (poly(VBPA-stat-4VP)s) will be prepared for the first time by ATRP at various comonomer compositions. Phosphonic acid moieties are chosen as protogenic groups while the pyridine groups act as proton acceptors. By variation of the comonomer composition, the effect of acid-base interaction (salt formation) of the acidic groups and the basic groups on proton conduction will be investigated in both, the dry state and if humidified. More information as the temperature dependence of proton transport and presence of mobile proton solvents (such as water and phosphoric acid) in such acid-base copolymers is expected from a comprehensive study of these copolymers.

2. Inorganic/organic nanocomposites. PVPA has been considered to be a promising proton-conducting polyelectrolyte to be used above 100 °C as proton-conducting membrane material for fuel cells. However, PVPA is very hygroscopic and soluble in water. Under humid conditions, the mechanical strength of a PVPA membrane is poor and PVPA even becomes liquid if being exposed to humidity for a long time. Therefore, the application of PVPA is limited.

In order to improve the mechanical strength of PVPA in the presence of humidity, a nanocomposite will be prepared with PVPA as the matrix and P4VP-grafted SiO₂ as the filling particles. This P4VP-grafted SiO₂ particle will be prepared by ATRP of 4VP grafting from silica nanoparticle surface. The P4VP shell is expected to enhance

the cohesion of the matrix and the filler by the acid-base interaction between P4VP and PVPA, and therefore, to improve the mechanical strength of PVPA under humid conditions. To the best of my knowledge, the effect of blending “basic” nanoparticles into an acidic polymer matrix on proton conduction has never been reported. Therefore, a study of proton conduction in such composites will be interesting, which will be carried out in this work.

3. Polymer blends. Making polymer blends is another powerful technique to tailor materials with improved properties. Although PVPA is a promising polyelectrolyte for proton conduction, the membrane of pure PVPA is too brittle for application. Moreover, the proton conductivity of PVPA in anhydrous state is not as high as expected (the same magnitude as molten phosphoric acid), probably due to the limited mobility of the polymer chain. The proton conductivity of PVPA in nominally dry condition at 150 °C is around 10^{-4} S/cm, while that of phosphoric acid at 42 °C can reach 7.7×10^{-2} S/cm.

Amorphous PEO is known as a flexible polymer with very low glass transition temperature (-19 °C) and contains abundant oxygen atoms in the backbone chain which can form hydrogen bonds with protons. These characteristic properties may be helpful to improve the mechanical property of PVPA to form homogeneous and flexible PVPA/PEO mixture membranes and may also be able to enhance the formation of a dynamic hydrogen bond network for proton conduction.

With this purpose in mind, PVPA/PEO blends will be prepared. The miscibility of PEO and PVPA will be studied and the proton conduction in PVPA/PEO blends will

be investigated as well.

CHAPTER 3

ATOM TRANSFER RADICAL COPOLYMERIZATION OF DIISOPROPYL-P-VINYLBENZYL PHOSPHONATE AND 4-VINYL PYRIDINE

3.1 Introduction

Controlled/living radical polymerizations, including atom transfer radical polymerization (ATRP), are receiving increasing attention because they are powerful tools for macromolecular design: the synthesis of homopolymers or copolymers with narrow molecular weight distribution, ^[1-3] the synthesis of end-functionalized polymers by selective termination of the chain ends with various reagents,^[4,5] the synthesis of novel statistical copolymers by the controlled addition of comonomers (e.g., semi-batch copolymerization) ^[6-8] and the synthesis of polymers with interesting properties simply by varying the topologies (i.e., star, comb, dendritic, hyperbranched). ^[9-13]

ATRP has been used successfully to prepare homopolymers and copolymers (ATRCRP) with different topologies by using multifunctional initiators, inimers, or macroinitiators. ^[10, 13-15] Gradient copolymers, in which the instantaneous composition varies continuously along the chain, have been prepared by ATRP as well. ^[6] In a batch copolymerization using a controlled/living polymerization technique such as ATRP, a gradient is produced spontaneously due to the feed composition drift that

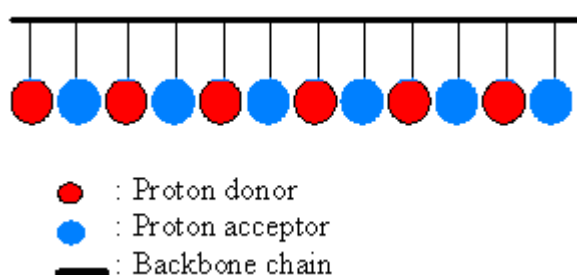
occurs during the reaction. ^[16, 17] In conventional free radical polymerization this drift is manifested in a change in composition among the chains, whereas in living polymerization the change in composition occurs in each chain provided that chain transfer can be suppressed. In systems which obey the terminal model the composition drift can be explained by the equation (Eq. 3.1),

$$F_1 = \frac{r_1 f_1^2 + f_1 f_2}{r_1 f_1^2 + 2 f_1 f_2 + r_2 f_2^2} \quad (3.1)$$

where r_1 and r_2 are the reactivity ratios, f_1 and f_2 are the molar fractions of monomers 1 and 2 in the monomer feed and F_1 is the molar fraction of units from monomer 1 in the copolymer. ^[18] Therefore, the design and simulation of a gradient copolymer with expected composition should be possible on the basis of an accurate estimation of the reactivity ratio of the monomers. Several pairs of comonomers have been polymerized by ATRP and their reactivity ratios have been determined under certain conditions. ^[16, 19-21] It has been reported that monomer pairs must have similar reactivity ratios as in a conventional radical polymerization because propagation occurs through the same free radical steps. ^[21, 22] However, some discrepancies in the value of reactivity ratios from ATRP and conventional radical polymerization have been observed. ^[23]

To the best of our knowledge, there is no report about the kinetic study of either atom transfer radical homopolymerization or copolymerization of vinylbenzyl phosphonates in which the ester group can be completely hydrolyzed to obtain phosphonic acids. The phosphonic acid containing polymers are important for some applications. For example, phosphonic acid containing materials are considered to be

most promising proton-conducting polyelectrolytes. ^[24-27] Heterocycle containing polymers such as poly (4-vinylpyridine) are also proton conductive in the presence of proton donors. For proton conduction, an ideal model of copolymers with both, proton donor and acceptor units would be a strong alternating copolymer. Scheme 1 shows the ideal model of a proton conducting copolymer with both, proton donors and proton acceptors.



Scheme 3.1: Schematic representation of the “ideal model” of proton conducting copolymer with both, proton donors and proton acceptors.

Among several procedures available to determine monomer reactivity ratios, the methods of Mayo-Lewis, ^[18] Finemann-Ross, ^[28] inverted Finemann-Ross, ^[29] Kelen-Tudos (K-T), ^[30] extended Kelen-Tudos, ^[31, 32] Tidwell-Mortimer, ^[33] and Mao-Huglin ^[34] are extensively used. The extended K-T method is a linear least squares (LLS) method that can be applied both, at low conversions (<15%) and medium-high conversions (<40%). ^[35] In conventional free radical polymerization, high polymers are formed even at the beginning of the reaction and the composition of the polymer is established at low conversion, while in ATRP, a high polymer is formed stepwise. At the beginning of the reaction, one monomer may react preferentially affected by the initiator. Therefore, in ATRP, a medium-high

conversion (20%-50%) is appropriate for the determination of the reactivity ratios of the comonomers. [6]

Table 3.1: Reaction conditions for ATRCP of DIPVBP and 4VP.

Experiment	Monomer feed molar ratio (DIPVBP/ 4VP)	$[M]_0:[I]_0: [CuCl]_0:[ligand]_0$
1	100 / 100	200:1:1*:1 (PMDETA)**
2	100/100	200:1:1*:1 (PMDETA)
3	100/ 100	200:1:1:1 (PMDETA)
4	100/100	200:1:1:1 (Me ₆ -TREN))
5	100 / 100	200:1:1:1 (HMTETA)
6	180/20	200:1:1:1 (HMTETA)
7	140/60	200:1:1:1 (HMTETA)
8	60/140	200:1:1:1 (HMTETA)
9	20/180	200:1:1:1 (HMTETA)

*: CuBr **: at 60 °C

In the present work, the ¹H-NMR technique has been applied online to investigate the kinetic parameters of ATRCP of DIPVBP and 4VP. This technique is informative and effective when the vinylic proton signals from each monomer are nonoverlapping with each other. Feed ratios and reaction conditions of ATRCP are listed in Table 3.1.

3.2 Monomer Conversion

Figure 3.1 shows the ¹H NMR spectrum of a reaction mixture at the beginning of the measurement. The vinylic proton signals from each monomer were well separated and the variety of each monomer concentrations can be continuously collected by comparing the integral of the vinylic proton signals from the monomers

to a standard which remain constant during the reaction. In this work, we set the peak ($\delta=4.57$ ppm) which refers to the single proton of the isopropyl group as internal standard. The conversion at each time (χ_t) for monomers can be calculated according to the following equation (Eq. 3.2),

$$\chi_t = \frac{A_0 - A_t}{A_0} \quad (3.2)$$

where A_0 is the primary normalized integral of the characteristic monomer peak ($t=0$) and A_t is the normalized integral of the characteristic monomer peak at time t . The cumulative composition of monomer 1 (F_t^1) and monomer 2 (F_t^2) at time t could be found using the following equations (Eq. 3.3-3.4),

$$F_t^1 = \frac{A_0^1 - A_t^1}{[A_0^1 - A_t^1] + [A_0^2 - A_t^2]} \quad (3.3)$$

$$F_t^2 = \frac{A_0^2 - A_t^2}{[A_0^1 - A_t^1] + [A_0^2 - A_t^2]} \quad (3.4)$$

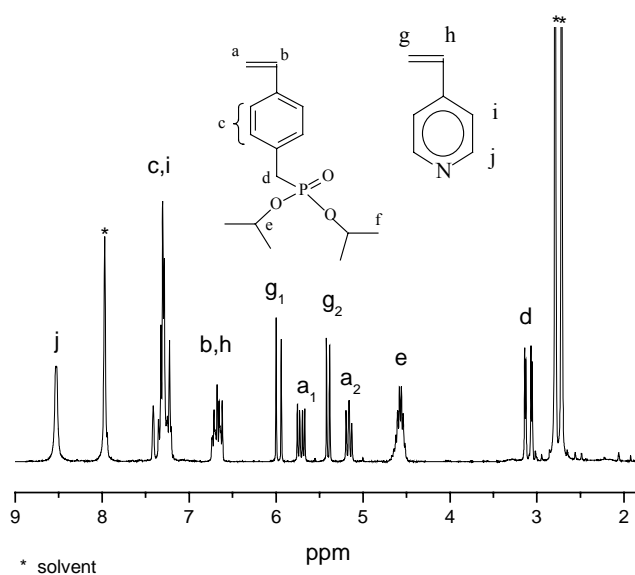


Figure 3.1: ^1H NMR spectrum of the reaction mixture of ATRCP of DIPVBP and 4VP at $t=0$.

3.3 ATRCP of DIPVBP and 4VP

Successful ATRP of DIPVBP could be achieved by using copper(I) complexes as catalyst and PMDETA, HMTETA, or Me₆TREN as ligand at 90°C in the bulk. However, 4VP is a coordinating monomer and the nucleophilic part will effect the reaction in different ways.^[36-37] DMF was used in order to obtain homogeneous reaction mixtures due to the bad solubility of 4VP and its polymer in less polar solvents. ATRCP of DIPVBP and 4VP using CuBr as catalyst has a faster reaction rate than that using CuCl due to the higher activity of the bromide complex (see Figure 3.2). However, significantly fast termination was observed when the reaction was carried out at 90°C in DMF using CuBr as catalyst. Several factors presumably contribute to the chain termination. Generally, nonpolar solvents are preferred for ATRP because certain polymer end groups, such as polystyryl halides, can undergo solvolysis or elimination of HX at elevated temperature.^[13] A slower chain termination was observed when the same reaction was performed at a lower temperature (60°C); however, the reaction rate of monomer addition was very slow. Another possible reason is that interactions between the halide-terminated chains and pyridine groups also make contributions to the chain termination. For this study, the effect of different copper(I) halide complexes and 4VP concentrations were investigated. As can be derived from Figure 3.2, a slower chain termination could be observed when catalyst CuBr was replaced by CuCl. The reaction of bromide-ended poly(4VP) chains with pyridine units was also observed and investigated by Matyjaszewski and coworkers^[37] who claimed that this reaction could be avoided

when CuCl was used. Various deviations from the initial reaction rates in the first order plots can be seen in Figure 3.3 with different 4VP concentrations. The curvatures appearing in the first order plots indicate the occurrence of chain termination. As we can derive from Figure 3.3, chain termination rates increase with the increasing concentration of 4VP which shows that pyridine units do affect the chain termination.

Due to the specialities of ATRCP of DIPVBP and 4VP, appropriate ligands should be selected to achieve the copolymerization. The kinetic chain length of a radical polymerization is proportional to the ratios of the monomer-to-radical concentrations and of propagation-to-termination rate constants. In order to increase the monomer conversion, an elevated reaction rate was expected when using an appropriate ligand. CuCl/PMDETA, CuCl/HMTETA, CuCl/Me₆TREN was used respectively as catalyst system in ATRCP of DIPVBP-co- 4VP carried out in DMF at 90°C. By comparing these three ligands, higher monomer conversions and reaction rates were obtained by using CuCl/HMTETA as catalyst system (see Figure 3.4).

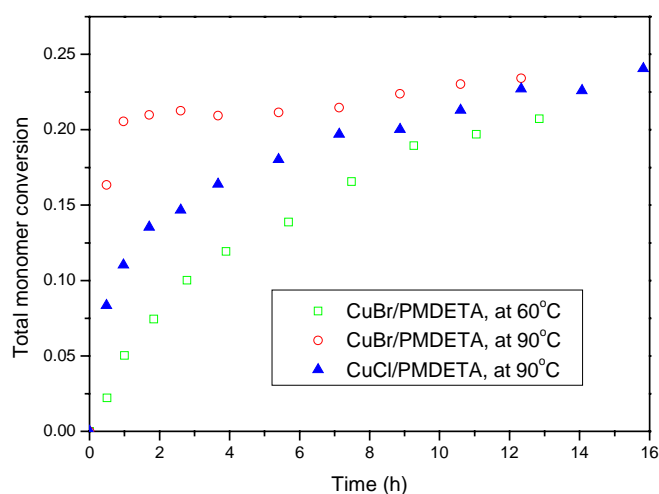


Figure 3.2: Total monomer conversions vs time of ATRCP of DIPVBP-co- 4VP carried out with the conditions shown in Table 3.1 (experiments 1-3).

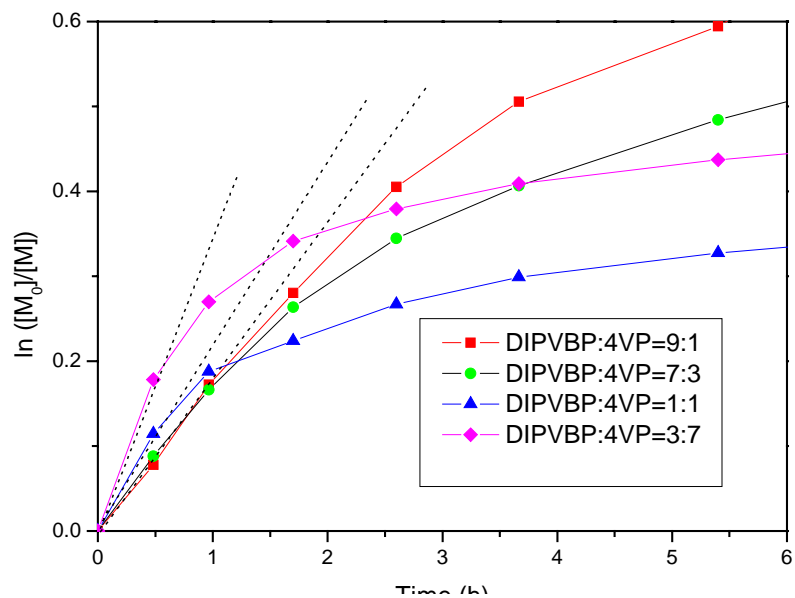


Figure 3.3: First order plots of ATRCP of DIPVBP-co- 4VP with various monomer feed ratios. Reaction conditions are given in Table 3.1 (experiments 5-8).

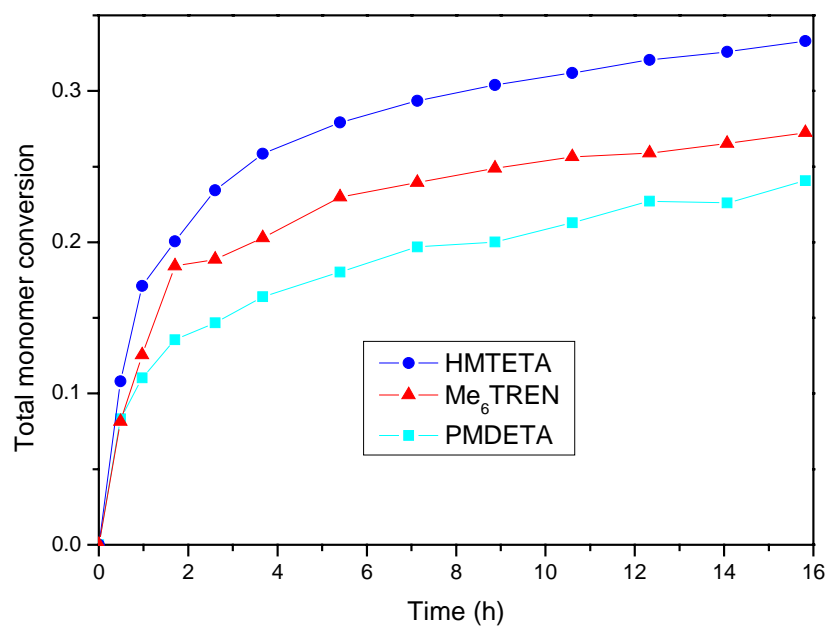


Figure 3.4: Total monomer conversions vs time of ATRCP of DIPVBP-co- 4VP using different ligands. Reaction conditions are given in Table 3.1 (experiments 3-5).

3.4 Monomer Reactivity Ratio Determination

The extended K-T method was applied to estimate the reactivity ratios of the comonomers. In this method, the reactivity ratio of monomer 1 (r_1) and monomer 2 (r_2) can be obtained by the following equations (Eq. 3.5-3.10),

$$\eta = (r_1 + \frac{r_2}{\alpha})\xi - \frac{r_2}{\alpha} \quad (3.5)$$

where

$$\xi = \frac{H}{\alpha + H} \quad \text{and} \quad \eta = \frac{G}{\alpha + G} \quad (3.6)$$

$$\alpha = (H_{\max} \cdot H_{\min})^{\frac{1}{2}} \quad (3.7)$$

$$H_{\max} = \text{MAX}(H_1, H_2, \dots, H_{n-1}, H_n) \quad \text{and} \quad H_{\min} = \text{MIN}(H_1, H_2, \dots, H_{n-1}, H_n) \quad (3.8)$$

$$H = \frac{F}{Z^2} \quad \text{and} \quad G = \frac{(F-1)}{Z} \quad (3.9)$$

then

$$Z = \frac{\log(\frac{A_t^1}{A_0^1})}{\log(\frac{A_t^2}{A_0^2})} \quad \text{and} \quad F = \frac{A_0^1 - A_t^1}{A_0^2 - A_t^2} \quad (3.10)$$

Relative concentrations of each monomer during the copolymerization process were obtained simultaneously by comparing the normalized integral of the vinylic proton signals from the monomers (see Figure 3.5). ATRCP of DIPVBP and 4VP with various feed ratios were carried out using CuCl/HMTETA catalyst system in DMF at 90 °C. All reactions were initiated by ethyl 2-bromoisobutyrate. The calculated parameters needed for the determination of reactivity ratios are shown in Table 3.2. The obtained reactivity ratio is 0.69 for DIPVBP and 1.17 for 4VP.

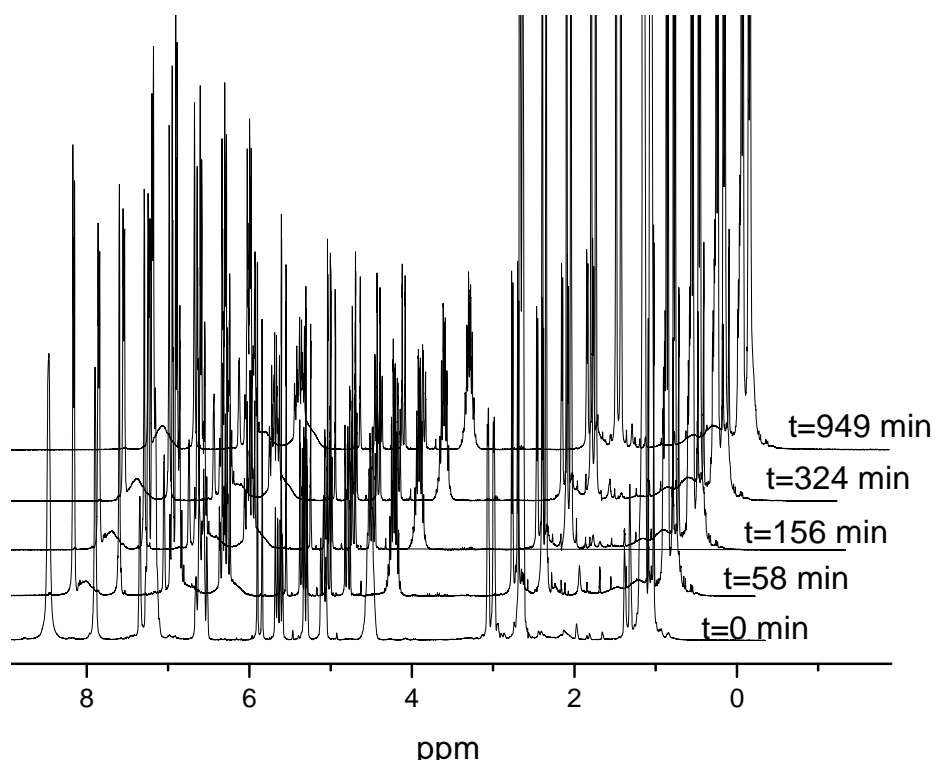


Figure 3.5: ATRCP of DIPVBP and 4VP detected using ^1H NMR technique-online.

Table 3.2: Parameters for the determination of reactivity ratios at high conversion by the extended K-T method

F	Z	G	H	ξ^a	η^a
8.28	1.09	6.65	6.90	0.93	0.93
3.00	1.40	1.42	1.52	0.74	0.73
1.44	1.52	0.29	0.63	0.54	0.36
0.67	1.87	-0.17	0.19	0.27	-0.50
0.26	2.52	-0.30	0.04	0.07	-1.27

^a The amount of a is 0.53

3.5 DIPVBP-stat-4VP Copolymers

All the copolymers obtained were isolated from the reaction mixtures and then purified and dried in a vacuum oven at 50 °C prior to characterizations.

3.5.1 Solution ^1H NMR spectra

Solution ^1H NMR was carried out to determine the chemical composition of the copolymers. Proper deuterated solvents were chosen according to the different solubility of the copolymers. The ^1H NMR spectra of the DIPVBP-stat-4VP copolymers were shown in Figure 3.6. In the ^1H NMR spectra, peak “a” is assigned to the pyridine ring and peak “e” is the characteristic peak form the isopropyl group of DIPVBP. By comparing these two peaks, we can learn that the 4VP molar ratio in the copolymer composition increases with the feed ratio of 4VP (ester1-5 are the file names of the corresponding copolymers listed in Table 3.3) in copolymerization.

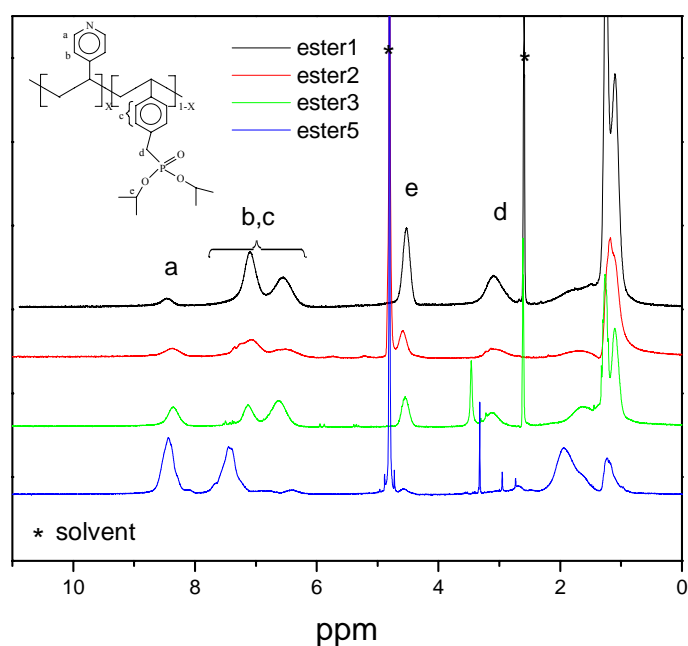


Figure 3.6: ^1H NMR spectra of the DIPVBP-stat-4VP copolymers.

3.5.2 Copolymer Compositions

The cumulative compositions of each monomer at a certain time t were calculated from monomer conversions during the copolymerization using Eq. (3.3, 3.4). The cumulative compositions (F_{cum}) of copolymers prepared with various monomer feed ratios are shown in Figure 3.7. The Figure shows that the compositions of the copolymers mostly depend on the monomer feed ratios due to the close value of reactivity ratios of DIPVBP (0.69) and 4VP (1.17). Therefore, various copolymer compositions can be achieved by simply changing the feed ratios of DIPVBP and 4VP.

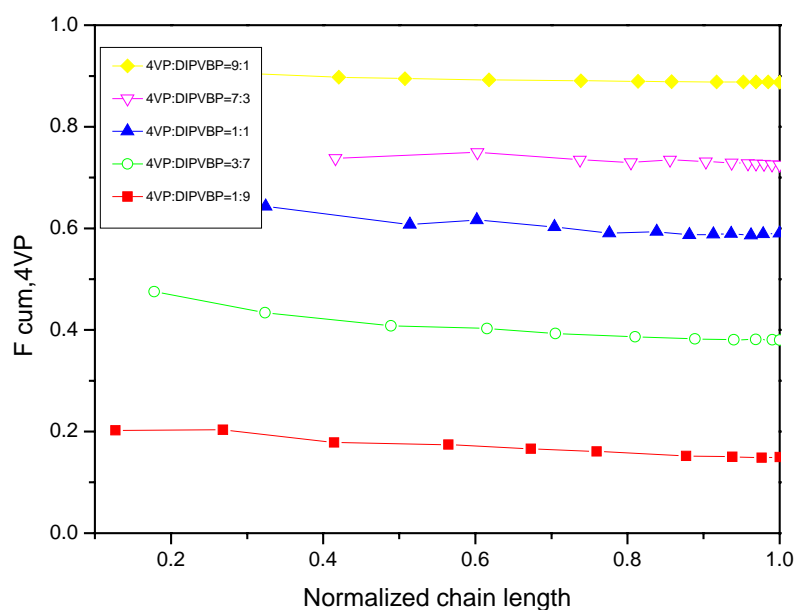


Figure 3.7: Cumulative copolymer composition vs normalized chain length for the ATRCP of DIPVBP-co-4VP with several monomer feed ratios. Reaction conditions are given in Table 3.1 (experiments 5-9).

The compositions of isolated copolymers were also calculated from the ^1H NMR spectra. Figure 3.8 shows the peaks used for the calculation of polymer compositions in the ^1H NMR spectrum of a DIPVBP-stat-4VP copolymer. From the integrations of the characteristic proton peak (a, b and c), the copolymer compositions can be calculated. The copolymer compositions from kinetic data are similar with that from ^1H NMR spectra (see Table 3.3).

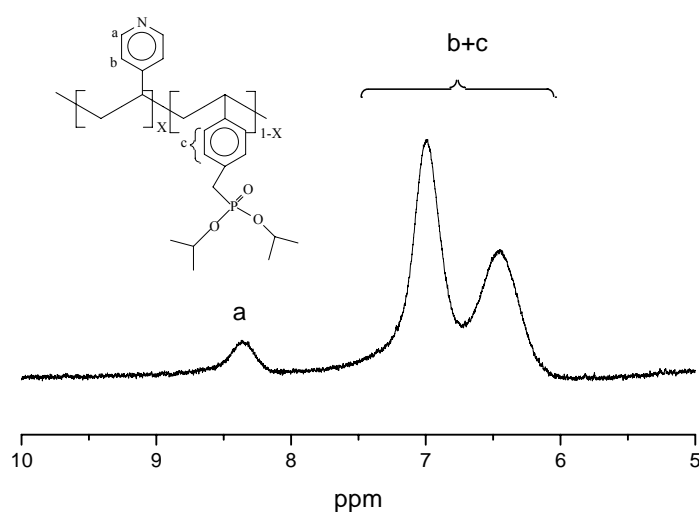


Figure 3.8: Peaks used for the polymer composition calculation in ^1H NMR spectra of typical DIPVBP-stat-4VP copolymers.

Table 3.3: Copolymer compositions from kinetic data and from ^1H NMR spectra

Experiment	File name	Monomer feed ratios DIPVBP: 4VP (molar ratio)	F (DIPVBP:4VP) (molar ratio)	
			Kinetic data	^1H NMR
5	ester3	50:50	41:59	43:57
6	ester1	90:11	85:15	83:17
7	ester2	70:30	62:38	61:39
8	ester4	30:70	27:73	25:75
9	ester5	10:90	11:89	8:92

3.5.3 Molecular weight and polydispersity

The copolymers for GPC measurements were isolated and purified after 22 hours' polymerization. The result (see Table 3.4) shows that the molecular weight distributions of the copolymers are broad ($M_w/M_n > 1.5$). However, in this work, no preformed deactivator (CuCl_2) was used to control the polymerization. The deactivator decreases the reaction rate, which may lower the monomer conversions and molecular weights in the presence of a significant chain termination or transfer reactions.

Table 3.4: Results of GPC of DIPVBP-stat-4VP copolymers*

Experiments	Monomer feed ratios DIPVBP: 4VP (molar ratio)	M_n (kg/mol)	M_w (kg/mol)	M_w/M_n
5	50:50	5.0	11.9	2.4
6	90:10	9.2	24.1	2.6
7	70:30	7.0	11.8	1.7
8	30:70	7.5	16.8	2.2
9	10:90	11.1	17.9	1.6

* Use polystyrene as standards

3.6 Hydrolysis of DIPVBP-stat-4VP copolymers

Poly(vinylbenzyl phosphonic acid-stat-4VP)s were prepared by complete hydrolysis of the phosphonate ester groups in DIPVBP-stat-4VP copolymers. Figure 3.9 shows the ^1H NMR spectrum of a typical DIPVBP-stat-4VP copolymer and its corresponding vinylbenzyl phosphonic acid-stat-4VP copolymer (VBPA-stat-4VP copolymer). The labeled peak ($\delta=4.57$ ppm) is the signal from the single proton of the isopropyl group. In the spectrum of VBPA-stat-4VP copolymer this peak can not be detected, which indicates a complete hydrolysis of DIPVBP-stat-4VP copolymer.

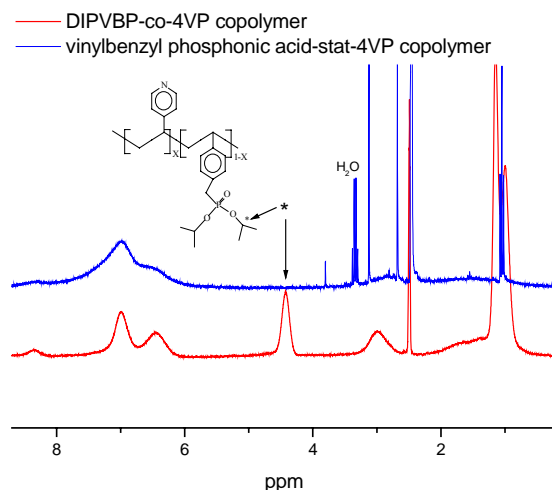


Figure 3.9: Solution ^1H NMR spectra of a typical DIPVBP-stat-4VP copolymer and its corresponding VBPA-stat-4VP copolymer.

The isopropyl phosphonate ester groups can be almost completely hydrolyzed by the approach applied in this work. Figure 3.10 shows the solution ^1H NMR spectra of Copo1, Copo3 and Copo5 (refer Table 4.1 for the file names). The peak from the single proton of the isopropyl group ($\delta=4.57$ ppm) almost disappeared in all these copolymers which proves the successful hydrolysis of the poly(DIPVBP-stat-4VP)s.

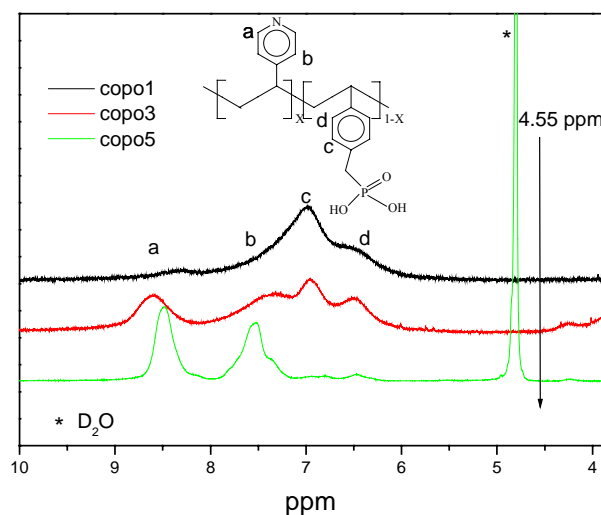


Figure 3.10: Complete hydrolysis of poly(DIPVBP-stat-4VP)s detected by solution ^1H NMR .

3.7 Thermal analysis

TGA was performed to investigate the thermal stability of the polymers. The polymers are stable below 150 °C; the weight loss starting at 150 °C refers to a self-condensation of the phosphonic acid groups (see figure 4.5). More details will be discussed in chapter 4.

Figure 3.11 shows the DSC result of all the copolymers (refer Table 4.1 for the file names). The shifting base line Copo1 and Copo2 is due to the self-condensation of the phosphonic acid groups. In curves of Copo3-Copo5, self-condensation is not as significant as in Copo1 because most of the acid groups stay with pyridine moieties and self-condensation can be reduced. No glass transition peak or degradation peak can be found in the temperature range of 25-145 °C. The glass transition temperature of the copolymers could be rather high because of strong acid-base interaction.

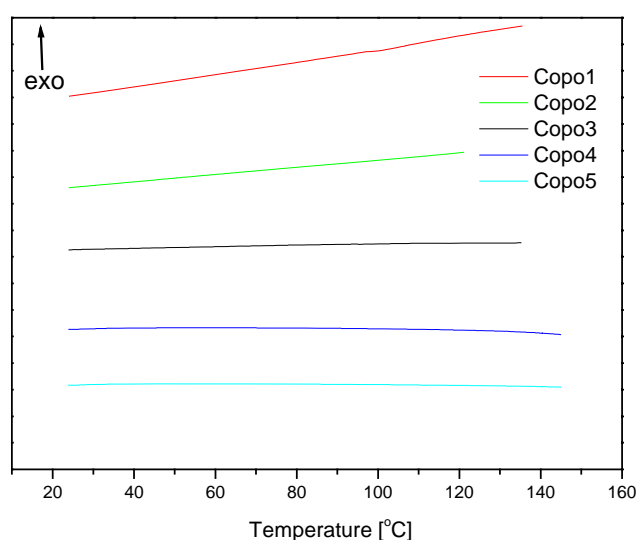


Figure 3.11: DSC curves of the copolymers.

CHAPTER 4

PROTON CONDUCTION IN VINYL BENZYL PHOSPHONIC ACID - 4-VINYL PYRIDINE COPOLYMERS

4.1 Introduction

In this chapter, a series of poly(VBPA-stat-4VP)s containing various compositions of phosphonic acid (VBPA) and pyridine moieties (4VP) has been investigated with respect to proton conductivity. Phosphonic acid is designed as protogenic group and the pyridine group as nucleophilic proton acceptor. The effects of polymer composition and water-content on proton conduction are discussed in this work.

The polymer compositions of poly(VBPA-stat-4VP)s were listed in table 4.1.

Table 4.1: Poly(VBPA-stat-4VP)s with different polymer compositions (* according to NMR analysis)

Poly(VBPA-stat-4VP)s	File name	Polymer composition in molar ratio* (VBPA:4VP)
Poly(VBPA-stat-4VP)-1	Copo1	83:17
Poly(VBPA-stat-4VP)-2	Copo2	61:39
Poly(VBPA-stat-4VP)-3	Copo3	43:57
Poly(VBPA-stat-4VP)-4	Copo4	25:75
Poly(VBPA-stat-4VP)-5	Copo5	8:92
Poly(vinylbenzyl phosphonic acid)	PVBPA	100:0

4.2 Characterization of PVBPA and Poly(VBPA-stat-4VP)s

4.2.1 Water Sorption

In order to determine the amount of water absorbed, the samples were stored under an atmosphere of fixed RH and temperature for several days until equilibrium weight was reached. The RH was set by saturated salt solutions according to literature data. ^[1] The uptake of water was measured on a Mettler MX5 micro balance. The water sorption was calculated from equation 4.1.

$$\text{water uptake (\%)} = \frac{W_{\text{wet}} - W_{\text{dry}}}{W_{\text{dry}}} \times 100 \quad [4.1]$$

All copolymers are hygroscopic and take up water that is expected to contribute significantly to the bulk proton conductivity under humidification. Fig. 4.1 shows the water uptake against relative humidity (RH) for the individual copolymers. The water uptake of the copolymers differs considerably at high RH, and appears to be strongest in copolymers with rather high 4VP content yielding liquid-like samples. It is still not clear why the water content of the membranes increases as the VBPA content in the copolymers decreases. However, PVBPA was not as hygroscopic as expected and was insoluble in water. Both, hydrogen-bonding and (possible) proton exchange among phosphonic acids, pyridine moieties and water were investigated by ¹H-MAS-NMR. The corresponding ¹H-MAS-NMR spectra of pristine PVBPA at different humidities are given in Figure 4.2(a). The fairly broad peak at 10.2 ppm observed for dried PVBPA is assigned to the protogenic group P(OH)₂ indicating moderately strong hydrogen-bonds. After being placed into 43% RH for 48h, water uptake shifts the POH peak to about 8.7 ppm reflecting fast proton exchange between P(OH)₂ units and

H₂O. In the case of copo5, the NH-peak shifts from 16.0 ppm to 12.7 ppm with increasing water content (cf. Figure 4.2(b)), thus suggesting proton exchange among NH and water molecules. The narrow peaks at 8.7 ppm and 7.8 ppm, respectively, nicely reveal mobility of the aromatic rings attached to the polyvinyl backbone.

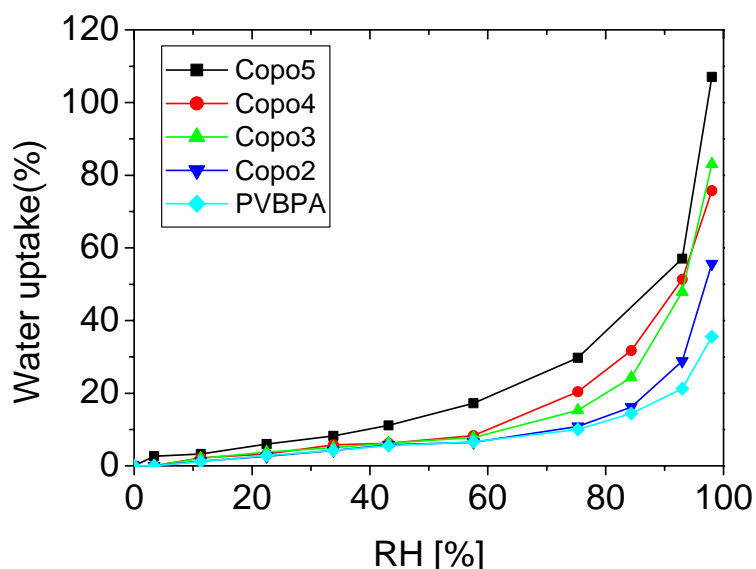


Figure 4.1: Water uptake (in weight %) at various RH at 25°C.

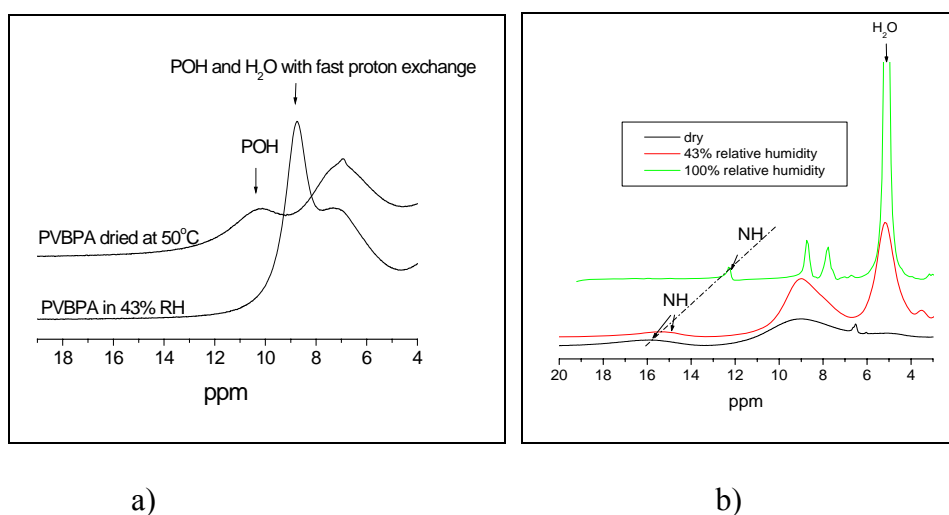


Figure 4.2: ¹H-MAS-NMR spectra of PVBPA (a) and Copo5 (b) with different water contents at 25°C.

4.2.2 Anhydride content

The ^{31}P -MAS-NMR spectra of PVBPA and Copo3 (43 mol% VBPA) are shown in Figure 4.3. The resonances at 29 ppm (a) and 24.5 ppm (b) are attributed to the phosphonic acid groups while the peaks at 19.4 ppm (a) and 16.9 ppm (b) are assigned to the phosphonic acid anhydride. This assignment is supported by annealing experiments that lead to increased anhydride formation. The overlapped peaks of phosphonic acid and anhydride were diluted and the deconvolution is performed with TopSpin $\text{\textcircled{R}}$ 2.0 (see in Figure 4.4). After annealing at 200 $^{\circ}\text{C}$ for 4 hours, considerable phosphonic acid anhydride can be observed in both PVBPA and Copo3; the fraction of phosphonic acid anhydride in PVBPA and Copo3 are 33.7% and 61% respectively. For the latter sample, prolonged annealing also lead to extended linewidths suggesting an increase of local structural disorder (e.g. sample deterioration). In contrast, only a tiny amount of self condensation of the phosphonic acid moieties is observed in the ^{31}P -MAS-NMR spectrum of Copo3 after annealing at 110 $^{\circ}\text{C}$ for 4 hours.

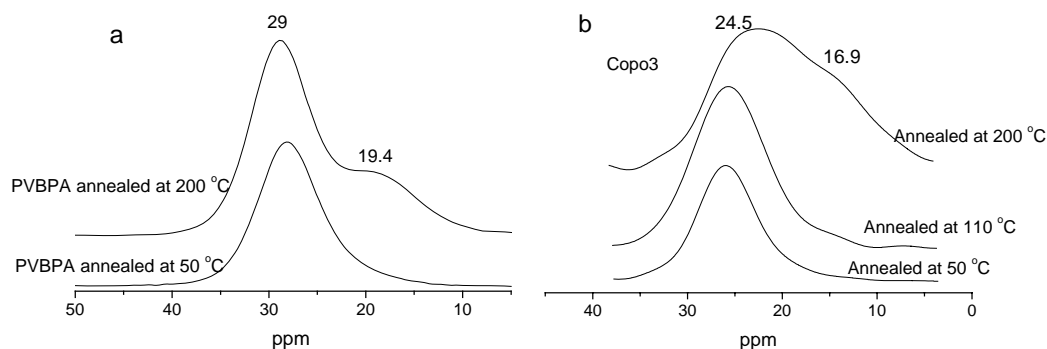


Figure 4.3: ^{31}P -MAS-NMR spectra of (a) PVBPA and (b) Copo3 after annealing.

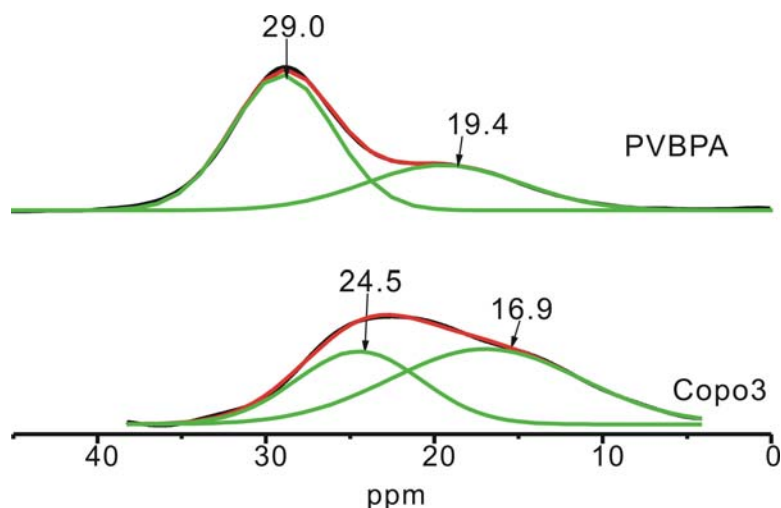


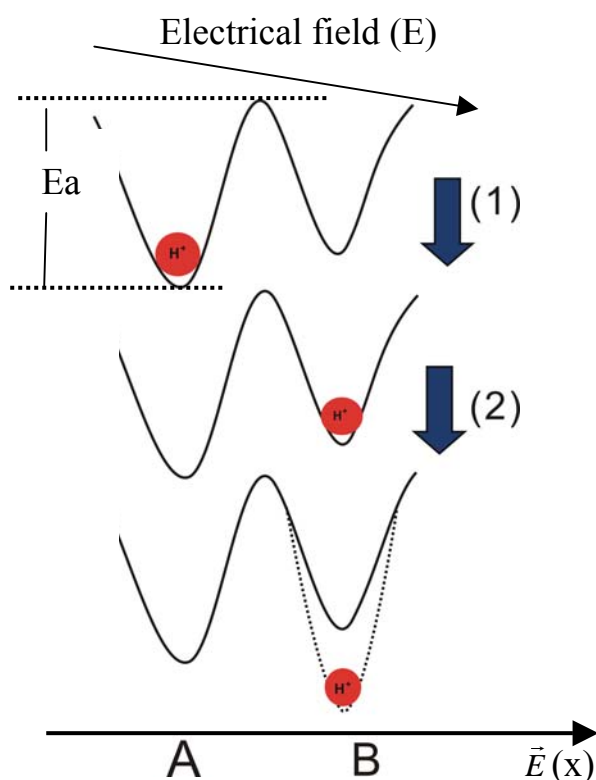
Figure 4.4: Deconvolution of ^{31}P -MAS-NMR spectra of (a) PVBPA and (b) Copo3 annealed at 200°C for 4 hours. (Black: measured peaks, red: fitted peaks and green: deconvoluted peaks)

TGA was also carried out to determine the water loss and self condensation of the phosphonic acid moieties. In Figure 4.5, the weight loss below 100°C may derive from absorbed water and the weight loss above 135°C (in PVBPA and Copo3) indicates significant self-condensation of the acid groups. However, no significant self-condensation can be observed in Copo5, because the concentration of phosphonic acid group is very low (8 mol %).

4.3 Temperature dependence of proton conductivity

Ion conduction is a phenomenon defined as long-distance ion migration which involves at least two steps (see Scheme 4.1): 1) translocation by hopping of the ion from site A to site B (given that the ion is exposed to a gradient of an electrical field); 2) reorganization of site B to form a lower energy configuration otherwise the proton will hop back to site A. The reason is that the hopping of ion from site A to B creates a local electrical field which will bring the ion back to site A; only if relaxation

happens in the same time scale and the energy of site B becomes lower than site A, the ion will stay at site B waiting for the chance to hop to the next vacancy along the field direction (“x” axis), otherwise, no long-distance ion migration will occur. [2, 3]



Scheme 4.1: Steps for proton transport in a model described by Funke et al. [2, 3] in energy versus space coordinates

The temperature dependence of the conductivity in polymer electrolytes has often been taken as being indicative of a particular type of conduction mechanism [4, 5] In particular, a distinction is generally made between systems which show an Arrhenius type of behavior and those which present a curvature in a logarithmic plot of conductivity versus inverse temperature.

An Arrhenius behavior of proton conductivity can be described by the Arrhenius equation (Equation 4.2)

$$\sigma = \sigma_0 \exp\left(\frac{-E_a}{RT}\right) \quad [4.2]$$

(E_a , R , T , σ_0 represent the activation energy scaled as a molar energy, gas constant, temperature and preexponential factor respectively)

The Arrhenius equation gives the dependence of the conductivity on the temperature T (in Kelvin) and activation energy E_a . When a conductivity obeys the Arrhenius equation, a plot of $\ln(\sigma)$ versus T^{-1} gives a straight line, whose slope and intercept can be used to determine E_a and σ_0 . The activation energy (energy barrier height) E_a is a rate determining factor of the conductivity process. The motion of ions is a thermally activated process and the ions need to have sufficient energy to overcome the energy barrier E_a . The preexponential factor σ_0 is the limiting conductivity of the system at temperature $T=\infty$ ($1/T=0$).

In many cases, a curvature in a logarithmic plot of conductivity versus inverse temperature has been observed. Several empirical equations have been used, as for example the Vogel-Tamman-Fulcher (VTF) equation (Equation 4.3) or Williams-Landel-Ferry (WLF) equation (Equation 4.4), to describe this particular type of conduction mechanism.

$$\sigma = \sigma_0 \exp\left\{\frac{-B}{T-T_0}\right\} \quad [4.3]$$

where σ_0 is a preexponential factor containing a $T^{1/2}$ term in addition to other constants; T_0 is the reference temperature which is generally placed ~ 50 K below the

experimentally observed glass transition temperature; B is a constant has the dimension of a temperature [K].

$$\sigma(T) = \sigma(T_r) \exp\left[\frac{C_1(T - T_r)}{C_2 + T - T_r}\right] \quad [4.4]$$

where T_r is the reference temperature (usually the Tg), $\sigma(T_r)$ is the conductivity at the reference temperature, C_1 and C_2 are empirical constants.

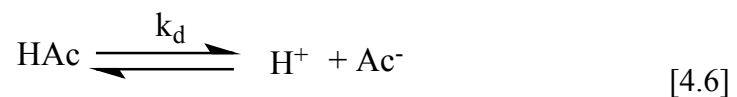
The VTF equation and the WLF equation are actually the same. Details can be found in literatures. [6-8]

The basic idea of ion conduction relating to the Free Volume theory is that the ion mobility is dictated by the available Free Volume at a given temperature.

According to Eq. 4.5, conductivity (σ) is proportional to the number of charge carriers (n) per unit volume (the charge carrier number density), the mobility of ions in an electric field (μ) and the number of charges per carrier.

$$\sigma(T) = n(T)\mu(T)q \quad [4.5]$$

Actually, in proton conductors, the number of charge carrier (proton) is not a constant but depends on the dissociation constant (k_d) of protons at a given Temperature. k_d is the equilibrium constant for a dissociation reaction, for example, as shown in Eq.4.6:



HAc is an acid which generates protons for proton conduction.

The equilibrium can be written symbolically as:

$$k_d = \frac{[H^+][Ac^-]}{[HAc]} \quad [4.7]$$

The relation between k_d and temperature T is:

$$\frac{\partial \ln k_d}{\partial T} = -\frac{\Delta H}{RT^2} \quad [4.8]$$

where R is the gas constant, ΔH is the enthalpy change. We can see that the temperature dependence of “total number” of dissociated protons follows Eq.4.8. However, only part of these protons participate proton conduction due to the energy barriers. The protons need energy to become “activated” that can overcome the energy barriers for proton conduction. The temperature dependence of the number (n) of the “activated” protons obeys the Arrhenius equation in Eq. 4.9

$$n(T) = n_0 \exp\left(\frac{-Ea}{RT}\right) \quad [4.9]$$

where n_0 is a preexponential factor and Ea is the activation energy of proton motion.

In the later discussion of this work, the charge carrier number density (n) in Eq. 4.5 is always considered as the charge carrier number density of “activated protons” (protons that participate proton conduction). If we neglect the effect of temperature on the dissociation constant, then the charge carrier density (n) basically obeys the Arrhenius equation (Eq. 4.9)

The temperature dependence of mobility μ is complicated and particularly, there are two types of dependence: (1) when the temperature dependence of proton mobility

shows an Arrhenius behavior, the relation between μ and temperature can be expressed with the Arrhenius equation (Eq.4.10).

$$\mu(T) = \mu_0 \exp\left(\frac{-Ea}{RT}\right) \quad [4.10]$$

where μ_0 is a preexponential factor and Ea is the activation energy for proton motion. (2) If the temperature dependence of proton mobility shows a VTF behavior, which is the more frequently observed case, the relation between μ and temperature can be expressed with the VTF equation (Eq.4.11).

$$\mu(T) = \mu_0 \exp\left(\frac{-B}{T-T_0}\right) \quad [4.11]$$

where μ_0 is a preexponential factor, B is a constant and T_0 is a reference temperature (usually Tg).

Eq.4.5, Eq.4.9 combined with Eq.4.10, We can obtain Eq.4.2; With Eq.4.5, Eq.4.9 and Eq.4.11, we can get a new equation of temperature dependence of proton conductivity (see Eq.4.12)

$$\sigma(T) = \sigma_0 \exp\left(\frac{-E_a}{RT} + \frac{-B}{T-T_0}\right) \quad [4.12]$$

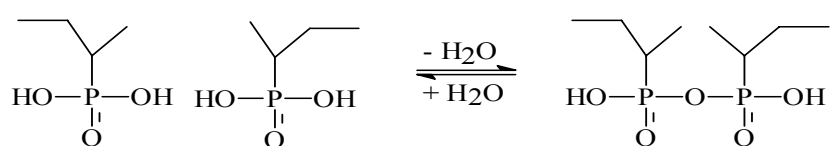
In both Eq. 4.2 and Eq. 4.12 the total number of dissociated protons is considered as constant. Given the number of “activated” protons is constant in Eq. 4.12, the proton conductivity has no relation with the activation energy (Ea) and the proton conduction is dictated by the available free volume. In this case, the temperature dependence of conductivity follows the VTF equation (Eq.4.3) which can be obtained out of Eq. 4.12.

We can conclude from the above discussion that, in most of the cases, different temperature dependence of ion conductivity in an Arrhenius plot mainly derives from the different temperature dependence of ion mobility.

Unfortunately, we can not use these equations to predict the temperature dependence of conductivity due to the limited experimental data. In the discussion of the results obtained in this work, we will refer to the validity and the usefulness of these equations.

4.3.1 Proton conduction under dry conditions

In a first experiment, data were recorded during a heating cycle from 20 to 150°C followed by a cooling cycle from 150 to 20°C. We always found a decrease in proton conductivity when comparing data from the heating to the cooling cycle. Possible reasons for the reduction of proton conductivity are the loss of residual absorbed water and self-condensation of the phosphonic acid moieties according to Scheme 4.2.



Scheme 4.2: Self-condensation (anhydride formation) between phosphonic acid groups.

TGA was also used to determine the water loss and self condensation of the phosphonic acid moieties. In Figure 4.5, the weight loss below 100°C may derive from the absorbed water and the weight loss starting from 135°C (in PVBPA and Copo3) indicates significant self-condensation of the acid groups. However, no significant self-condensation can be observed in Copo5, because the concentration of

phosphonic acid group is very low (8 mol%) and the acid-base interactions can reduce the self-condensation of phosphonic acid moieties.

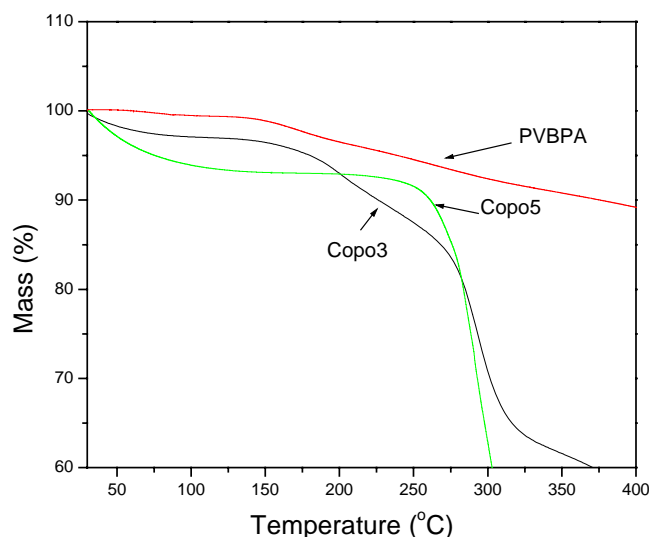


Figure 4.5: TGA of PVBPA, Copo3 and Copo5 with a heating rate of 1K/min in dry nitrogen atmosphere.

Therefore, we devised a special set of experiments to investigate the proton conductivity of PVBPA and poly(VBPA-stat-4VP)s under well defined conditions. Before the measurements were started, all the samples were placed in a sealed atmosphere of 33% RH for 48 h. Controls proved the samples being equilibrated after that time period with the humidity conditions. Then, in the first step, the samples were heated to 50°C and flushed with dry nitrogen for 24 hours. In the second step, the temperature was set to 110°C for a period of 7 days, and in the last step of the experiment, the samples were stored at 150°C for another 3 days (all under dry nitrogen). The conductivity of PVBPA was recorded continuously during the

experiment whereas the conductivity of the copolymers was sampled at intervals.

Figure 4.6 displays the results.

In the first step the conductivities of all samples decrease sharply which corresponds to water loss (compare Figure 4.5) and proves a strong dependence of the proton conductivity on the water content under these conditions. At the end of the second step annealing at 110°C under dry nitrogen, the proton conductivity almost reaches a constant level which is close to the value of proton conductivities of the polymers at 110°C when vacuum-dried samples are investigated. The relatively low intrinsic proton conductivities found in all the copolymers are presumable due to the limited proton mobility.

At 150°C, a further decrease of the proton conductivity is probably due to loss of charge carriers caused by anhydride formation of the phosphonic acid groups.

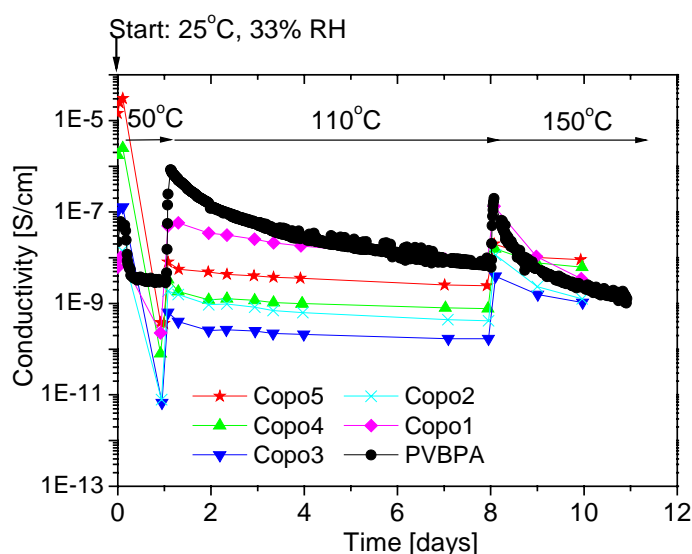


Figure 4.6: Time and temperature dependence of the conductivity of PVBPA and poly(VBPA-stat-4VP)s under dry N₂

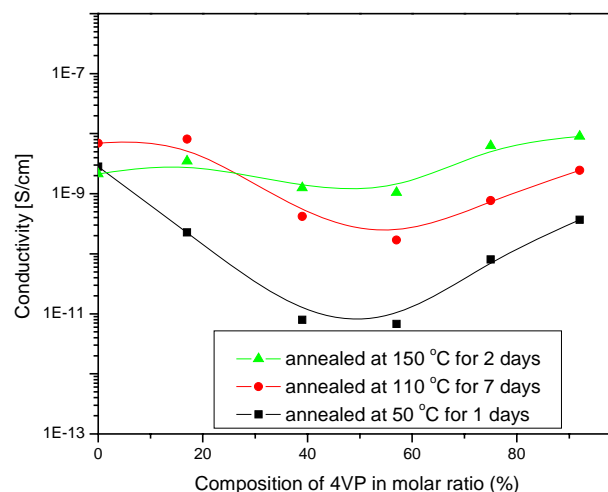


Figure 4.7: Composition dependence of the conductivity of poly(VBPA-stat-4VP)s in quasi equilibrium conditions.

In Figure 4.7, the composition dependence of the conductivity of the copolymers under quasi equilibrium conditions using the data of Figure 4.6 are displayed. It appears that a molar ratio of 4VP and VBPA of about 1:1 yield the lowest proton conductivities.

Under dry conditions, the proton conductivities show Arrhenius type behavior (see Figure 4.8). According to the Arrhenius equation 4.2, the activation energy for proton conductivity can be calculated from the temperature dependent conductivities shown in Figure 4.8 and σ_0 can be obtained from the intercept on the conductivity axis at $1/T=0$. The results are shown in Table 4.2.

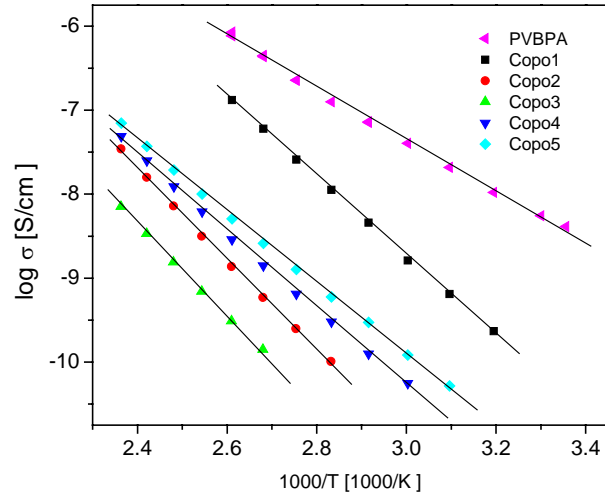


Figure 4.8: Temperature dependence of conductivities in poly(VBPA-stat-4VP) under dry conditions.

Table 4.2: E_a and σ_0 obtained from Figure 4.8

Samples	E_a (kJ/mol)	$\log \sigma_0$ (S/cm)
PVBPA	60.5	1.88
Copo1	90.2	5.45
Copo2	103.4	5.26
Copo3	106.4	4.59
Copo4	90.6	3.53
Copo5	81.9	2.82

Figure 4.9 shows the calculated activation energies derived from Table 4.2. The results indicate that the polymer composition has a strong effect on the activation energy for proton conduction. The activation energy reaches the maximum at a 1:1 molar ratio comonomer composition at which the acid-base interactions also reach the maximum extend. Therefore, it can be assumed that the salt formation in the copolymers increases the E_a for proton conduction. The maximum of activation

energy explains the minimum of the conductivity, when the composition dependence is considered. However, the reason why salt formation increases E_a for proton conduction is not clear yet.

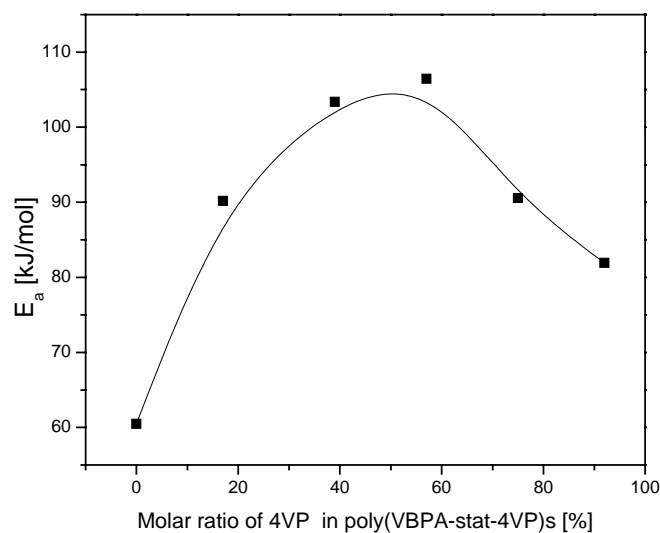


Figure 4.9: Composition dependence of the activation energy for conductivity in nominally dry poly(VBPA-stat-4VP)s

4.3.2 Proton conduction under humidification

In a fuel cell, water is constantly produced at the cathode so that fuel cells are operating under humidified conditions. Therefore, the conductivities of the poly(VBPA-stat-4VP)s and PVBPA in atmospheres with different degrees of relative humidity (RH) were also investigated. Figure 4.10 shows the proton conductivities of the polymers against RH at 25°C. We can see that all the conductivities increase rapidly with RH. The increasing water content (see the water uptake data displayed in Figure 4.1) leads to rapidly increasing conductivity which can reach 10^{-2} S/cm at high RH. Figure 10 shows the apparent effect of polymer compositions on proton conductivity when plotted against relative humidity. However, the data also shows

that water is significantly important for proton conduction in these polymers and proton conduction might mainly depend on water content in the polymers.

Therefore, we plotted the conductivity versus water content (water uptake) in the polymers (see Figure 4.11) based on the data in Figure 4.10 and Figure 4.1.

In Figure 4.11, we can see a master curve of the relation between proton conductivity and water content. It is demonstrated that, with the water uptake higher than 2%, protons can not “see” the underlying polymer structure and proton conduction happens in the water solvation. Therefore, we can conclude that, with the water uptake higher than 2%, proton conductivity is only based on water content in the polymer and the polymer structure does not affect the proton conduction.

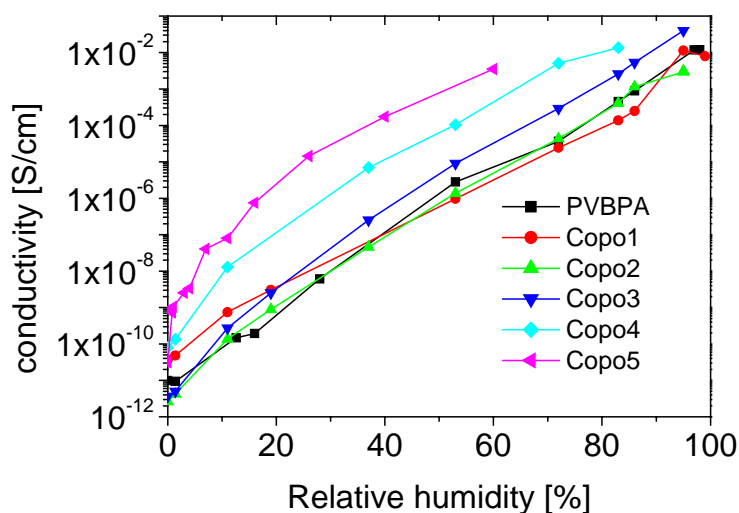


Figure 4.10: Proton Conductivities of the copolymers versus relative humidity at 25°C

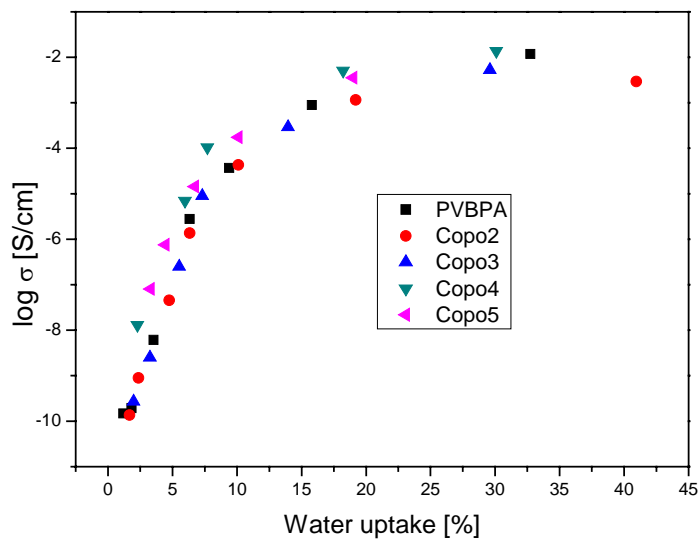


Figure 4.11: Master curve in the plot of conductivity versus water content (water uptake) in the polymer

The conductivities of Copo5, Copo3 and PVBPA at elevated temperatures determined under 1 bar water vapor pressure are compared in Figure 4.12. In such an experiment, the RH constantly decreases with increasing temperature. At 120°C, pure water vapor in the gas phase corresponds to about 50% RH and 150°C sets the RH to 20%. The rapid decrease of proton conductivity of Copo5 with increasing temperature indicates that water content in Copo5 decreases rapidly with increasing temperature. For PVBPA, the proton conductivity remains almost constant above 120 °C. The reason is that, at high temperatures (above 120 °C) self-condensation of the acid groups can produce water which can maintain the water content in the polymer and therefore, the proton conductivity. The behavior of Copo3 is in between of PVBPA and Copo5.

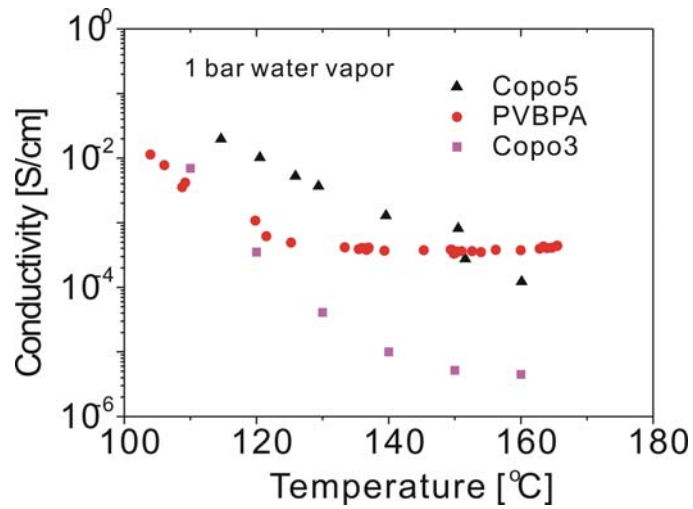


Figure 4.12: Proton conductivity of Copo5, Copo3 and PVBPA determined at elevated temperatures under 1 bar water vapor pressure.

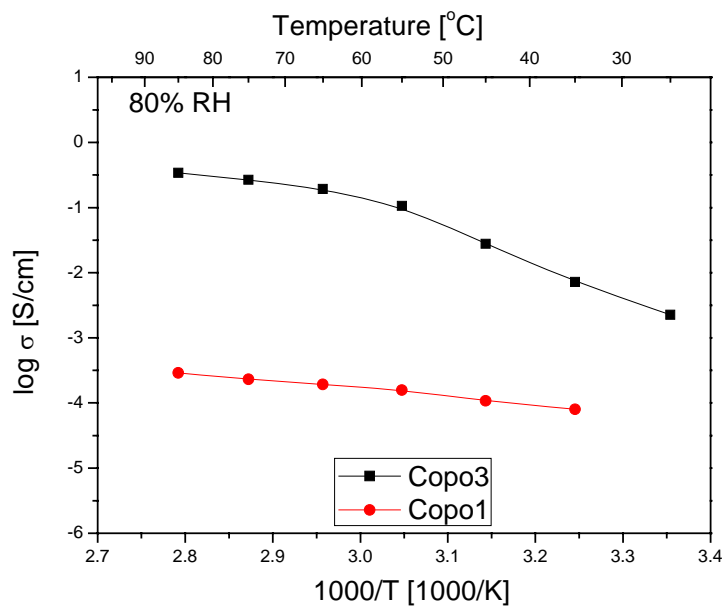


Figure 4.13: Proton conductivity of Copo1, Copo3 determined at various temperatures under 80% RH.

Figure 4.13 shows the proton conductivities of Copo1 and Copo3 as a function of temperature measured in 80% relative humidity. We can see that proton conductivity of Copo1 and Copo3 show different temperature dependence. According to the master curve in Figure 4.11, we can conclude that, the different conductivity of Copo1 and

Copo3 is only a result of different water contents which is caused by different water uptake properties of the polymers.

Under these conditions, Copo3 can absorb more water than Copo1, therefore, the conductivity of Copo3 is several magnitudes higher than that of Copo1. At 85 °C, 80% RH, the proton conductivity of Copo3 can reach 0.3 S/cm.

4.3.3 Proton conduction of Copo3 blended with phosphoric acid

Phosphoric acid (H_3PO_4) is an amphoteric compound which shows very high intrinsic proton conductivity as a pure liquid. Therefore, H_3PO_4 was often blended with polymer materials to obtain anhydrous proton conductors for the application above 100 °C. The state-of-the-art H_3PO_4 based proton conductor is a polybenzimidazole/ H_3PO_4 blend.

As being discussed above, Copo3 shows the lowest proton conductivity under dry conditions. However, after doping with H_3PO_4 , the proton conductivity increases dramatically with the doping level X (see Figure 4.14). Here, X refers to the molar ratio of H_3PO_4 to the total repeat units of Copo3. With the doping level of 0.42, the proton conductivity increases by more than 4 orders of magnitude which is as high as that of PBI with the doping level of 1.8. When increasing the doping level to 1.3, the proton conductivity of Copo3 can reach 10^{-2} S/cm at 120 °C.

Interestingly, we can see different types of behavior at different doping levels. In nominally “dry” state ($X=0$), due to the very high Tg of the polymer, the proton conductivity shows Arrhenius behavior.

When $X = 0.42$, the T_g of Copo3 is lowered to around $100\text{ }^\circ\text{C}$ (see Figure 4.15). Below T_g , the temperature dependence of conductivity is linear in the Arrhenius plot and shows an Arrhenius behavior; above T_g , a curvature appears. If we extrapolate the straight line to a higher temperature and subtract the conductivity of the linear part, we can see the additional conductivity which results from the additional proton mobility caused by the increased free volume.

With $x=1.3$, the T_g of the material is around $0\text{ }^\circ\text{C}$ according to Figure 4.15. Strikingly, we can see that the temperature dependence of conductivity is linear in the temperature range of $20\text{-}100\text{ }^\circ\text{C}$ which is far above the T_g . The influence of increased free volume with increasing temperature above T_g on proton conductivity is not indicated. An interpretation might be like that:

With the doping level of $x=1.3$, there are abundant of continuous hydrogen-bond networks within the material, formed among the polymer matrix and the added phosphoric acid. Fast proton conduction can be carried out by the cooperative proton migration through the several bonded hydrogen bonds (refer Figure 1.4, the Daycock's model, the proton transfer step) together with the reorientation step in the form of rotations of the side groups and phosphoric acid molecules and, if above T_g , the segmental motion. The rotation of the side groups or phosphoric acid molecules can take place even below T_g and shows an Arrhenius type behavior. While segmental motion only can take place above T_g . According to the Free Volume theory, above T_g , the increase of Free Volume can enhance the mobility of the chain segments and, therefore, the conductivity. If the segmental motion contributes significantly to proton

conduction, a curvature will appear in an Arrhenius plot of conductivity according to Eq.4.12. Particularly, when the number of charge carriers is constant, the curve fits the VTF equation (Eq.4.3).

However, the extent by which segmental motion contributes to the conductivity varies with the nature of the materials, temperature and pressure. Consequently, different temperature dependence of conductivity can be observed.

For example, with $x=1.3$, the effect of segmental motion on conductivity is small, therefore the temperature dependence of conductivity basically shows an Arrhenius behavior; with $x=0.42$, the segmental motion significantly contributes to proton conduction, therefore a curvature appears above T_g .

We can see that, with $x=1.3$, the conductivity above 100 °C becomes constant. This is probably an artifact due to loss of H_3PO_4 via self-condensation of the acid groups.

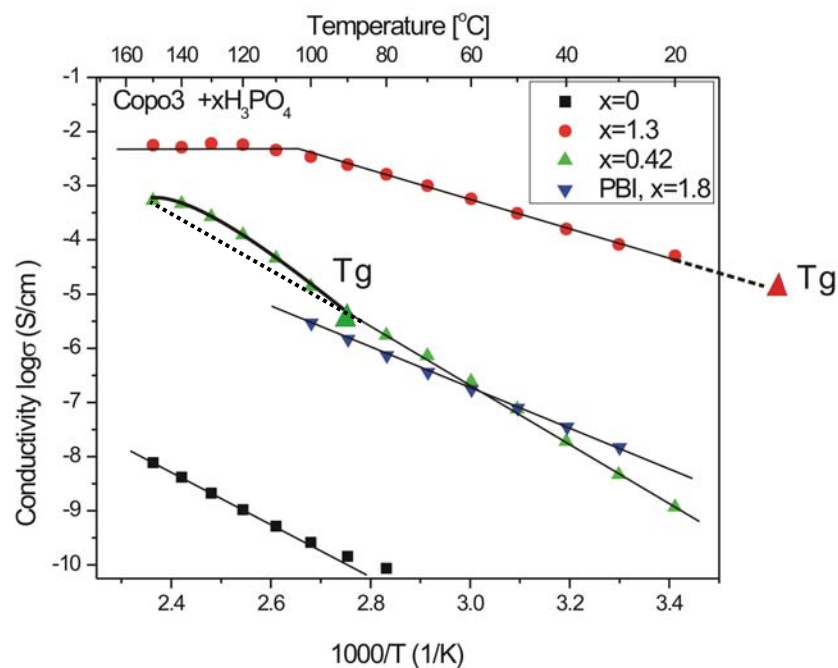


Figure 4.14: Proton conductivity of Copo3 doped with H_3PO_4 .

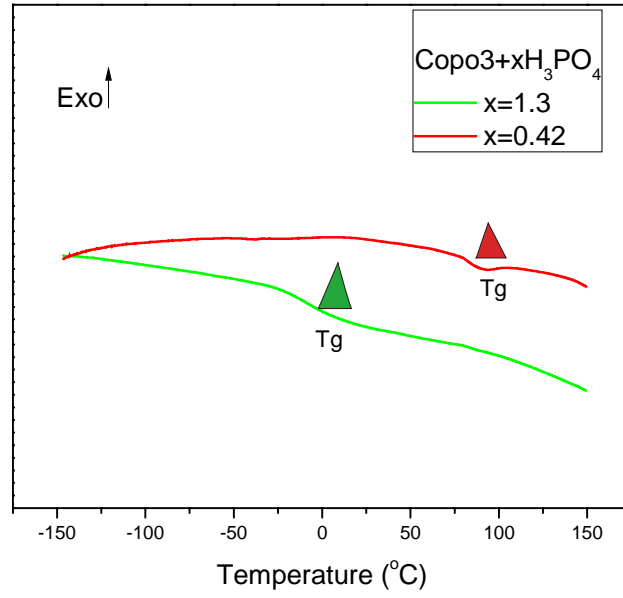


Figure 4.15: DSC curves of Copo3 doped with H₃PO₄.

CHAPTER 5

PROTON CONDUCTION IN BLENDS OF PVPA AND P4VP GRAFTED SILICA NANOPARTICLES

5.1 Introduction

The conductivities of poly(VBPA-stat-4VP)s been studied in the previous chapter. The result shows that strong acid-base interactions are not favorable for proton conduction. However, mobile proton carriers such as water and phosphoric acid can facilitate proton transport in these solid state polyelectrolytes and high proton conductivity up to 10^{-2} S/cm can be achieved.

With high water or phosphoric acid content, the mechanical properties of the materials are not sufficient for the application as a proton electrolyte membrane. The formation of inorganic/organic nanocomposites is a powerful technique to tailor materials that have unique properties, and thus maybe used to combine good conductivity with good mechanical properties.

Poly(vinyl phosphonic acid) (PVPA), for example, is promising as an proton-conducting polyelectrolyte. ^[1] PVPA shows high proton conductivity (10^{-2} S/cm) under humidity. However, PVPA is water soluble and the mechanical property is poor when exposed to water vapor. Most of the proton conductive groups (e.g. sulfonic acid, phosphonic acid and imidazole) are hydrophilic which leads to good water solubility of the polyelectrolyte. In order to improve the mechanical properties

of these proton conductive polyelectrolytes in the presence of mobile proton solvents, inorganic/polymer hybrids are considered to be an efficient approach.

It was reported that Nafion/SiO₂ nanocomposites are prepared and studied as compared to pure Nafion for the application of PEM for fuel cells. [2-9]

These nanocomposite membranes exhibited improved stability, reduced methanol crossover, higher fuel efficiency, and proton conductivity compared to pristine Nafion. Under humidity, the composite membrane showed a higher uptake of water compared to the Nafion recast membrane. The proton conductivities of the composite membranes appeared to be similar to that of the native Nafion membrane at high temperatures and at high relative humidity (RH), however, it was much higher at low RH.

In this work, a novel organic/inorganic nanoparticle was prepared via surface-initiated polymerization. This nanoparticle was then used as filler for the PVPA matrix. Surface-initiated polymerization from substrates such as silica gels and silica wafer is also called “grafting from” as compared to “grafting to” which refers to grafting of already preformed polymer chains to the substrate by anchoring groups.

Using the “grafting from” technique covalently attached polymer films can be obtained with high graft densities and thicknesses ranging from several nanometers up to more than one micrometer. [10] Different approaches can be applied for the polymerization of “grafting from”. [11-13] Living radical polymerization (LRP), as applied to surface-initiated graft polymerization, [14-28] has the overwhelming advantage over other grafting from techniques in that it allows grafting of homo- and

copolymers of controlled structures with an extremely high grafting density. On inorganic substrates, the grafting density can reach as high as 0.7 chains/nm² for common polymers such as poly(methyl methacrylate) (PMMA) and polystyrene (PS). This grafting density is almost 1 order of magnitude higher than those obtained by other techniques.

Atom transfer radical polymerization (ATRP) is one of the LRP techniques which allow good control of molecular weight and of molecular weight distribution. [29, 30]

Poly(4-vinyl pyridine) was grafted from the surface of SiO₂ nanoparticles using ATRP. ATRP of 4-vinyl pyridine (4VP) was firstly reported by Matyjaszewski et al. [31] However, grafting 4VP from the surface of silica nanoparticles by ATRP has not been reported before. Following this approach, silica nanoparticles with a shell of polymeric layer will be used to be incorporated into a polymeric acidic matrix. The knowledge of polymeric acid doped with basic nanoparticles is limited. In this work, 4VP was successfully grafted from silica nanoparticles and the effect of doping PVPA with this particle was studied under both humidified and dry conditions.

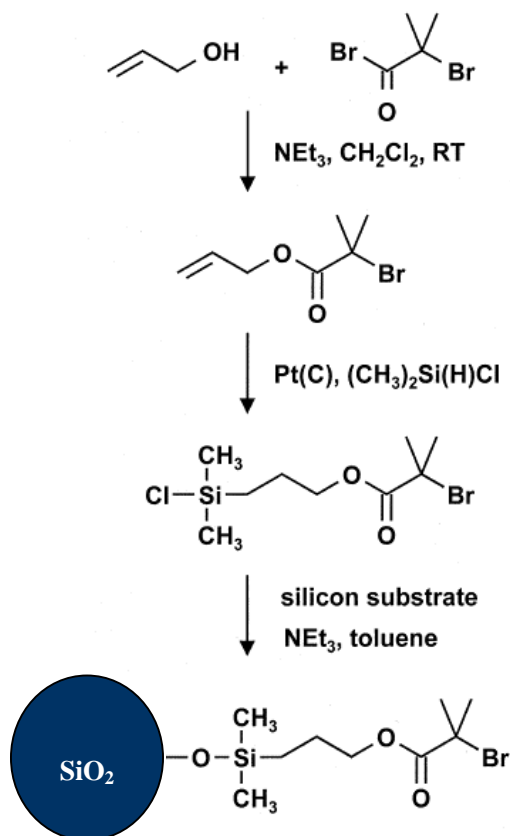
5.2 Poly(4-vinyl pyridine) grafting from silica nanoparticles

Polymer grafting from an inorganic substrate can be carried out by two steps. The first step is the immobilization of an initiator on the inorganic substrate. The initiator can be either covalently or physically grafted on the surface of a substrate. The second step is the in situ polymerization directly initiated from the substrate surface. Due to

the high graft density of the initiator, the polymer graft density is normally higher as compared with “grafting to” technique.

5.2.1 Initiator immobilization

The synthesis and covalent attachment of an α -bromo ester initiator to the silica gel surface are illustrated in Scheme 5.1. Esterification of 2-bromo-2-methylpropionyl bromide with allyl alcohol was followed by hydrosilation with dimethylchlorosilane. The initiator consists of a reactive chlorosilane group capable of bonding to the silica surface hydroxyl groups. FT-IR, NMR proved that both esterification and hydrosilation were effective and the desired product was obtained. New signals at 0.4 and 0.8 ppm in the ^1H NMR spectrum correspond to protons adjacent to the silicon. The absence of any signal above 5 ppm indicates the quantitative conversion of the allyl ester to the initiator. Reactions of the chlorosilyl groups of the initiator with surface silanol groups of silica particles were performed under inert conditions in the presence of triethylamine (NEt_3 , TEA) as a catalyst and acid scavenger. As a result, a monolayer of molecules containing an α -bromoester moiety was obtained (Scheme 5.1). The amount of grafted initiator was calculated according to the results of the elemental analysis.

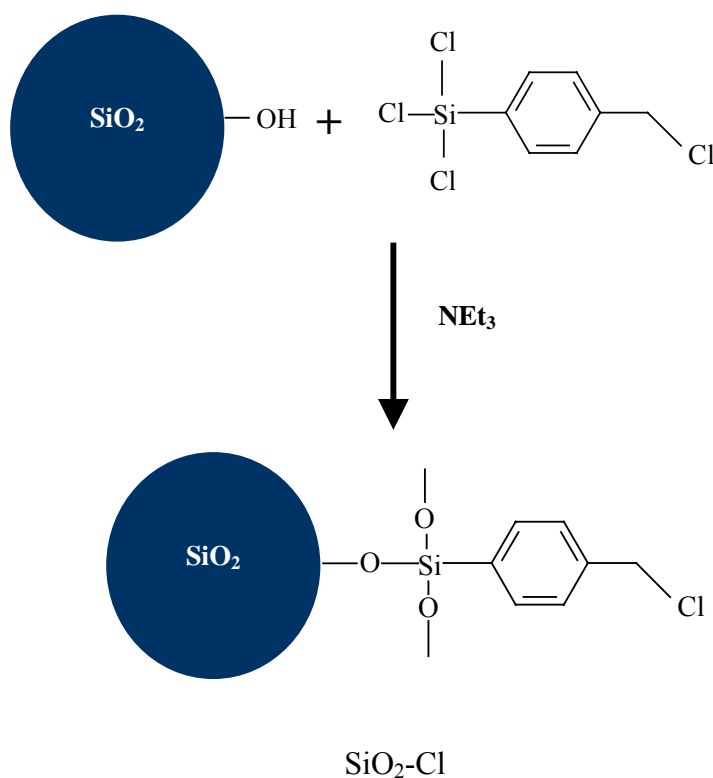


Scheme 5.1: Procedure of synthesizing SiO₂-Br.

As an other initiator, 4-(chloromethyl)phenyltrichlorosilane was immobilized to silica nanoparticles via the anchoring of the reactive chlorosilane groups with the surface hydroxyl groups. The procedure is illustrated in Scheme 5.2.

FT-IR, TGA, and elemental analysis (EA) were used to prove that an α -bromo ester and 4-(chloromethyl)phenyltrichlorosilane were successfully bonded to the surface of silica nanoparticles respectively. Figure 5.1 shows the FTIR spectra of bare SiO₂, SiO₂-Br and SiO₂-Cl. The additional organic peaks in the spectra after surface modification demonstrate that initiators were grafted on to the silica surface. Figure 5.2 shows the TGA results of SiO₂-Cl compared with that of bare SiO₂. Around 25% mass loss can be found in the curve of SiO₂-Cl which relates to the degradation of

organic component. This result meets well with the result of EA. The initiator graft densities (see Table 5.1) were calculated from the elemental analysis results.



Scheme 5.2: Reaction scheme for the generation of $\text{SiO}_2\text{-Cl}$.

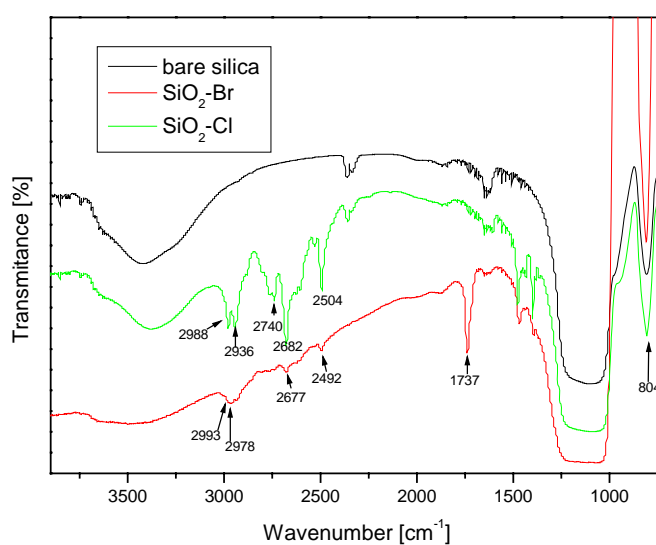


Figure 5.1: FTIR spectrum of bare SiO_2 , $\text{SiO}_2\text{-Br}$ and $\text{SiO}_2\text{-Cl}$.

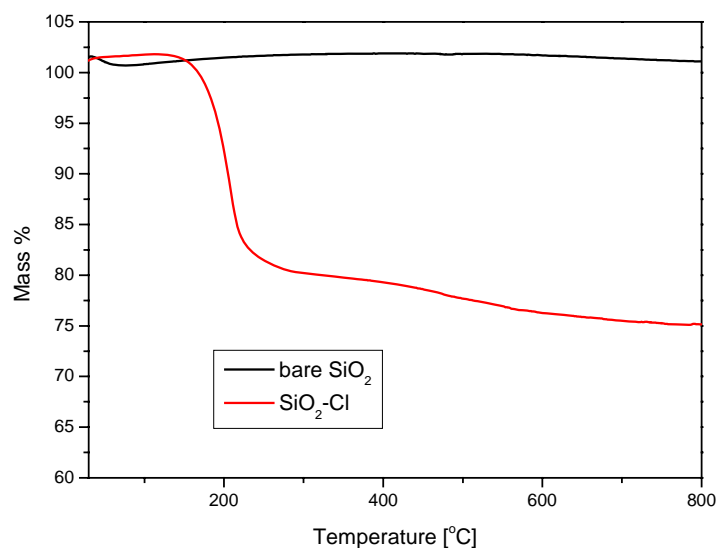


Figure 5.2: TGA curves of bare SiO₂ and SiO₂-Cl measured in nitrogen atmosphere.

Table 5.1: Initiator graft densities of SiO₂-Br and SiO₂-Cl.

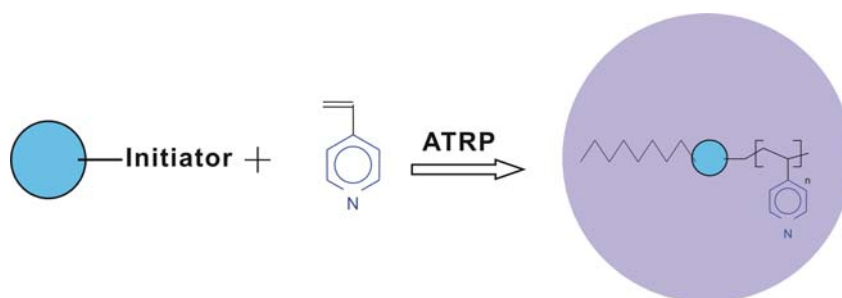
Samples	C %	H %	Graft density calculated from EA	Graft density calculated from TGA
SiO ₂ -Br	8.79	1.8	1.01 mmol/g SiO ₂	/
SiO ₂ -Cl	17.25	2.7	2.48 mmol/g SiO ₂	2.62 mmol/g SiO ₂

5.2.2 ATRP of 4VP grafting from silica nanoparticles

In recent years ATRP has been the most widely employed technique for the preparation of polymer brushes via surface initiated polymerization. ATRP is compatible with a variety of functionalized monomers, and the living/ controlled character of the ATRP process yields polymers with a low polydispersity (M_w/M_n) that are end functionalized and so can be used as macroinitiators for the formation of

di- and triblock copolymers. Equally important, surface-initiated ATRP is experimentally more accessible than for example, the living anionic and cationic polymerizations, which require rigorously dry conditions. The synthesis of thiol and silane derivatised surface-bound initiators is easier than the AIBN–silane derivative or the nitroxide silane derivative for free radical polymerizations. The controlled nature of ATRP is due to the reversible activation–deactivation reaction between the growing polymer chain and a copper–ligand species. Matyjaszewski and co-workers reported controlled polymerizations without added free initiator; [32] instead a CuII ligand complex was added to act as a deactivator. The addition of these complexes to the polymerization solution increased the initial CuII concentration to the same level as the addition of free initiator.

ATRP of 4VP was first reported by Matyjaszewski and his coworkers [31]. The silica surface initiated ATRP of 4VP was adopted from their work. SiO₂-Br and SiO₂-Cl were used as macroinitiators respectively and then poly(4-vinyl pyridine) grafted silica nanoparticles named SiO₂-Br-4VP and SiO₂-Cl-4VP correspondingly were obtained. The procedure for grafting is shown in Scheme 5.3.



Scheme 5.3: ATRP of 4VP grafting from silica surface.

5.2.3 Characterization of SiO₂-Br-4VP and SiO₂-Cl-4VP

The polymer compositions of SiO₂-Br-4VP and SiO₂-Cl-4VP were determined by TGA and EA respectively. Figure 5.3 shows the TGA results of SiO₂-Br-4VP and SiO₂-Cl-4VP. The weight loss of 81.25% in SiO₂-Br-4VP and 94.18% in SiO₂-Cl-4VP refers to the corresponding polymer compositions.

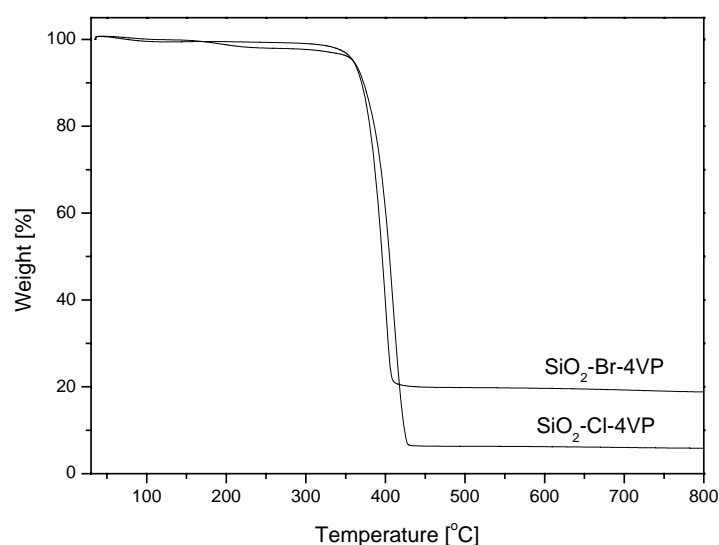


Figure 5.3: TGA curves of SiO₂-Br-4VP and SiO₂-Cl-4VP.

EA was also carried out to determine the polymer compositions in SiO₂-Br-4VP and SiO₂-Cl-4VP. The results of EA are shown in Table 5.2. The theoretical weight ratio of C and N is 6.0. The detected values by EA meet well which indicates the reliability of the calculated polymer composition from the EA results. The polymer compositions obtained by TGA and EA are quite similar which is around 82% for SiO₂-Br-4VP and 94% for SiO₂-Cl-4VP.

Table 5.2: EA results and polymer composition of SiO₂-Br-4VP and SiO₂-Cl-4VP

Sample	C %	H %	C/N	Polymer composition	
				EA	TGA
SiO ₂ -Br-4VP	65.6	10.95	6.02	82.22%	81.25%
SiO ₂ -Cl-4VP	75.28	12.5	5.99	94.41%	94.18%

The high polymer composition indicates a very efficient polymerization and high grafting densities. In this work the polymer grafting density can not be detected directly. We introduced a cleavable anchoring group (ester group) in SiO₂-Br-4VP in order to cut the polymer from silica particles. However, after hydrolysis in acid at elevated temperature, no free poly(4-vinyl pyridine) could be detected separately by GPC. A possible reason may be that, due to the high graft density, the acid can not reach the silica surface to induce the hydrolysis. Hydrofluoric acid was also used for etching the silica. However, no free polymer can be separated according to GPC results due to the same reason discussed above.

In order to estimate the graft density of SiO₂-Br-4VP and SiO₂-Cl-4VP, identical chain growth is assumed for the grafting ATRP from silica nanoparticles which means every initiator can induce polymerization and each chain growth with the same rate ($M_w/M_n=1$). This is a characteristic feature for ATRP which leads to narrow polydispersity of the obtained polymer. Based on this assumption, polymer density should be the same as initiator graft density. Therefore, the molecular weight can be estimated (see Table 5.3).

Table 5.3: Estimated polymer density and molecular weight of SiO₂-Br-4VP and SiO₂-Cl-4VP

Samples	Initiator (polymer) graft density		Polymer Composition				Molecular weight (g/mol)	
	mmol/g SiO ₂	chains/nm ²	Polymer/ (polymer+SiO ₂) (Wt %)		Polymer/SiO ₂ (g/g)			
			EA	TGA	EA	TGA	EA	TGA
SiO ₂ -Br-4VP	1.01	2.31	82.22	81.25	4.62	4.33	4574	4287
SiO ₂ -Cl-4VP	2.48	3.78	94.41	94.18	16.9	16.2	6810	6524

The silica particle used is fumed silica. The diameter of single silica nanoparticle is around 7 nm. TEM and SEM were applied to observe the morphology of the silica particles before and after grafting. Figure 5.4 is the SEM image of bare fumed silica. We can see that the primary diameter of a single particle is less than 10 nm with bad dispersability. However, SiO₂-Br and SiO₂-Cl show improved dispersability due to the surface modification (See Figure 5.5). The particle size remains the same as bare silica particles.

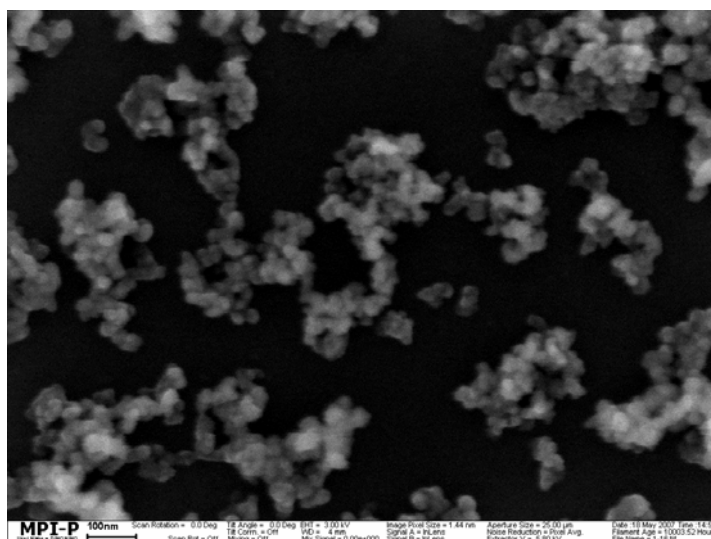


Figure 5.4: SEM image of bare fumed silica

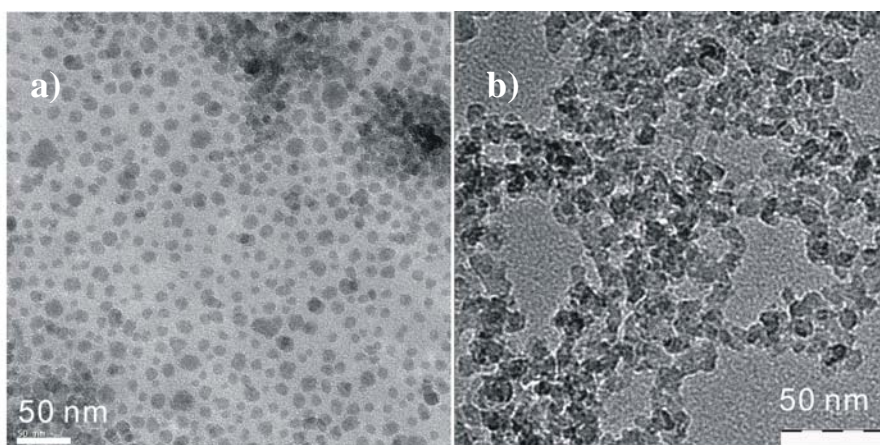


Figure 5.5: TEM images of a) SiO₂-Br and b) SiO₂-Cl.

The SEM and TEM images of SiO₂-Br-4VP are shown in Figure 5.6. The diameter of SiO₂-Br-4VP ranges from 40-60 nm. In the TEM images, slight cross-linking among the particles can be observed due to the coupling of end groups of the polymer chain during ATRP.

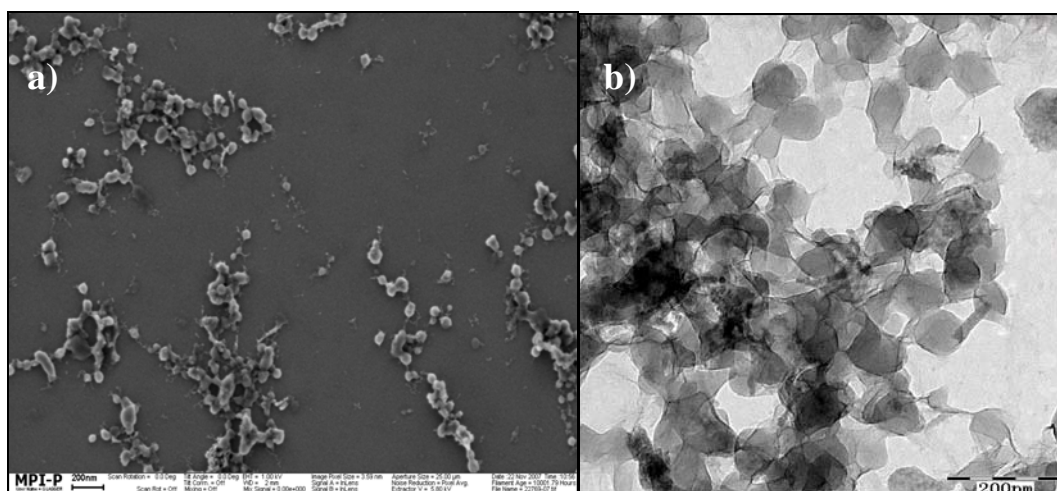


Figure 5.6: a) SEM and b) TEM of SiO₂-Br-4VP.

Figure 5.7 shows the SEM and TEM images of SiO₂-Cl-4VP. We can find that in the TEM image, the diameter of SiO₂-Cl-4VP ranges from 40-100 nm; the particles are more spherical than that of SiO₂-Br-4VP because of the much higher graft density of polymer chains.

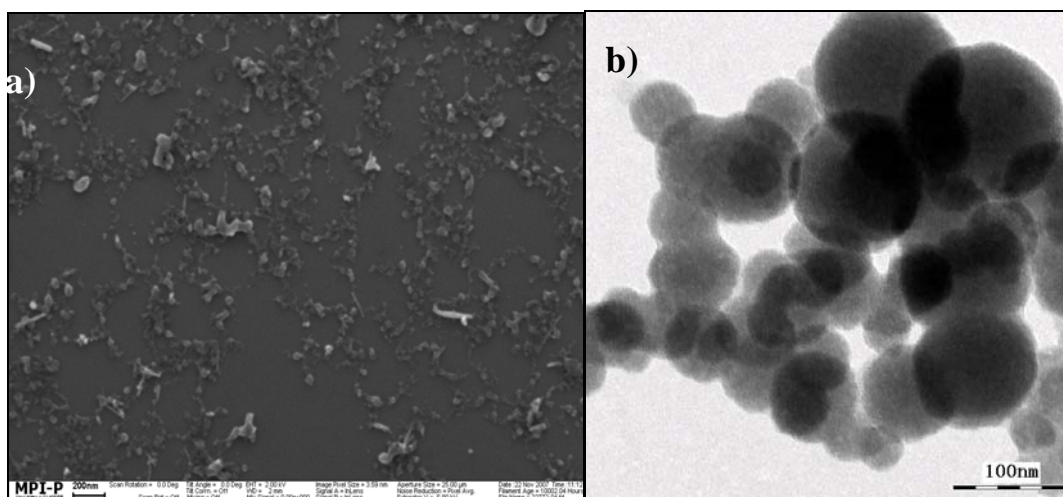


Figure 5.7: a) SEM and b) TEM images of SiO₂-Cl-4VP.

5.3 Proton conduction in the blends of SiO₂-Cl-4VP and PVPA

The blends were prepared by adding a SiO₂-Cl-4VP suspension to an aqueous solution of PVPA. Homogeneous mixtures were obtained after ultrasonication and freeze drying. Samples with various compositions are listed in Table 5.4. The mass ratio of SiO₂-Cl-4VP and PVPA turns out to be the same with the molar ratio of 4VP and VPA repeat units.

Table 5.4: Sample list of SiO₂-Cl-4VP and PVPA blends

Samples	File name	Composition (mass ratio) (SiO ₂ -Cl-4VP: PVPA)	molar ratio of 4VP: VPA
1	BA1	1:9	1:9
2	BA2	2:8	2:8
3	BA3	3:7	3:7
4	BA4	5:5	5:5
5	BA5	7:3	7:3
6	BA6	9:1	9:1

5.3.1 Proton conduction under dry conditions

Nominal dry proton conductivities of the blends were measured and shown in

Figure 5.8. The proton conductivity decreases with increasing content of P4VP grafted silica nanocomposite.

Scheme 5.4 schematically shows the morphology of the acid-base particle blends. In statistical acid-base copolymers, the acid-base interaction (salt formation) reaches a maximum around the molar ratio of 1:1 of the acid and base components which leads to a minimum conductivity at this ratio. However, in SiO₂-Cl-4VP blended with PVPA, the acid-base interphase increases with the particle component, because the SiO₂-Cl-4VP particles are surrounded by a PVPA-P4VP-complex and no continuous P4VP phase can be formed. Therefore, with increasing amount of basic particles, more and more acid-base complex interfaces need to be overcome for the long distance migration of protons, which means the activation energy for proton conduction will increase.

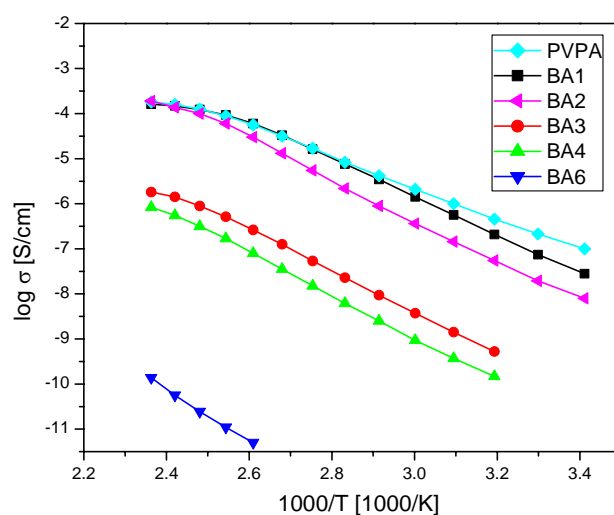
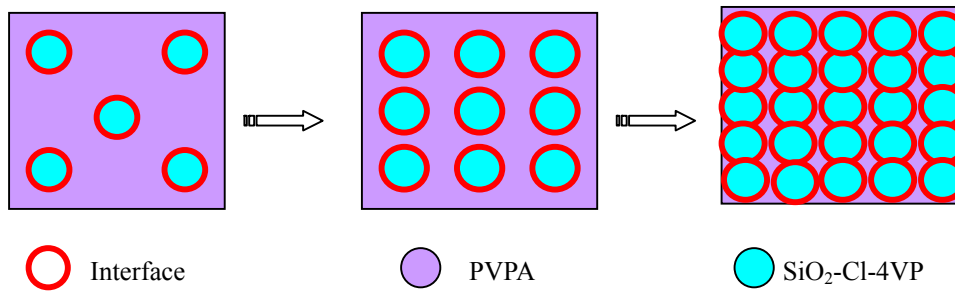


Figure 5.8: Arrhenius plot of the conductivities of SiO₂-Cl-4VP/ PVPA blends under dry conditions.



Scheme 5.4: Morphology of SiO₂-Cl-4VP/ PVPA blends with various compositions.

According to the Arrhenius equation 4.2, the activation energy (E_a) for proton conductivity can be obtained from the temperature dependent conductivities shown in Figure 5.8. Table 5.5 shows the obtained activation energies calculated from Figure 5.8. The results indicate that the activation energy increases with the SiO₂-Cl-4VP content which meets well with the prediction, and explains the decreasing proton conductivity.

Table 5.5: Activation energy calculated from Fig. 5.8

Samples	E_a (kJ/mol)
PVPA	65
BA1	81
BA2	87
BA3	89
BA4	92
BA5	117

Moreover, according to Eq. 4.5, conductivity (σ) is decided by both the number of charge carriers (n) and mobility (μ). The effect of SiO₂-Cl-4VP/ PVPA content on proton conductivity has been discussed above with respect to activation energy (E_a).

However, the number of mobile protons decrease dramatically with increasing volume filling of SiO₂-Cl-4VP due to the strong salt formation and, as a result, these captured protons do not participate in proton conduction within the measuring time scale. Solid state ¹H-NMR spectra were recorded to investigate the acid-base interactions in the composites of PVPA and SiO₂-Cl-4VP with various compositions. In the spectra (Figure 5.9), the peak around 15.5 ppm refers to NH (protonation of the pyridine unites); the peak around 11.7 ppm is the resonance of POH from the phosphonic acid group.

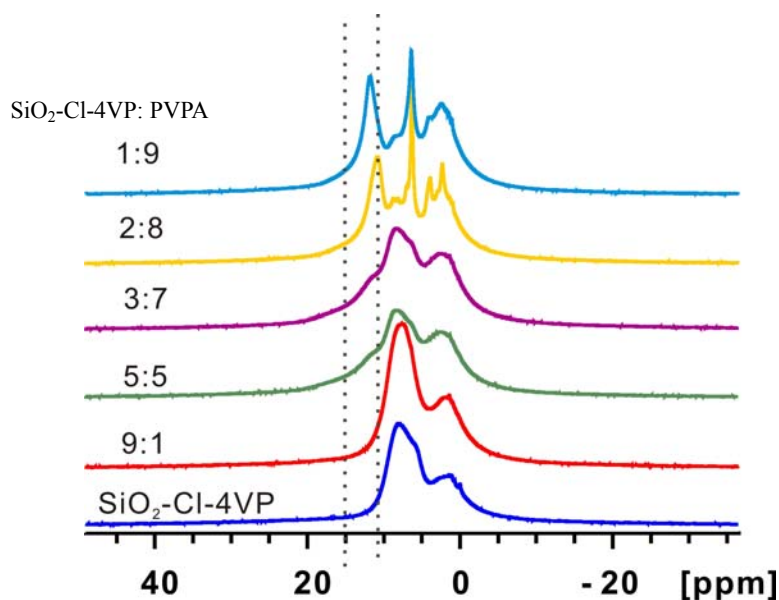
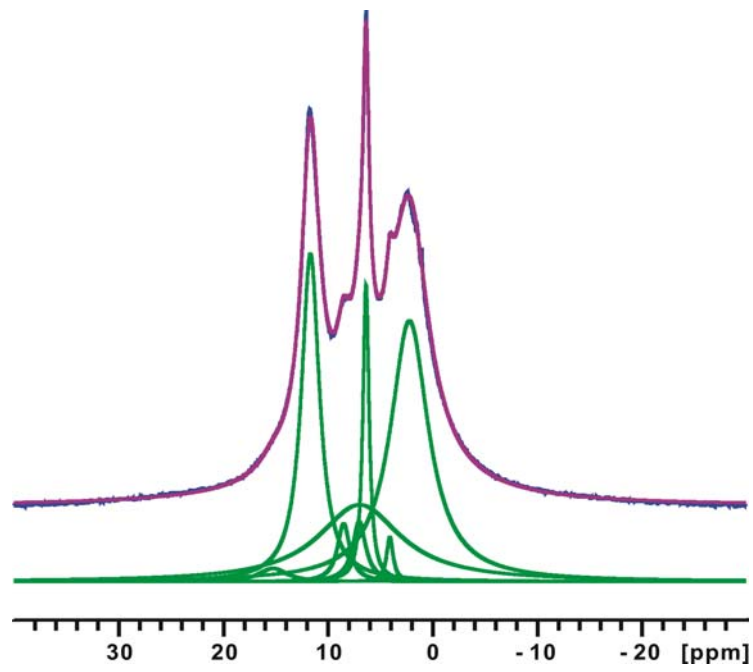
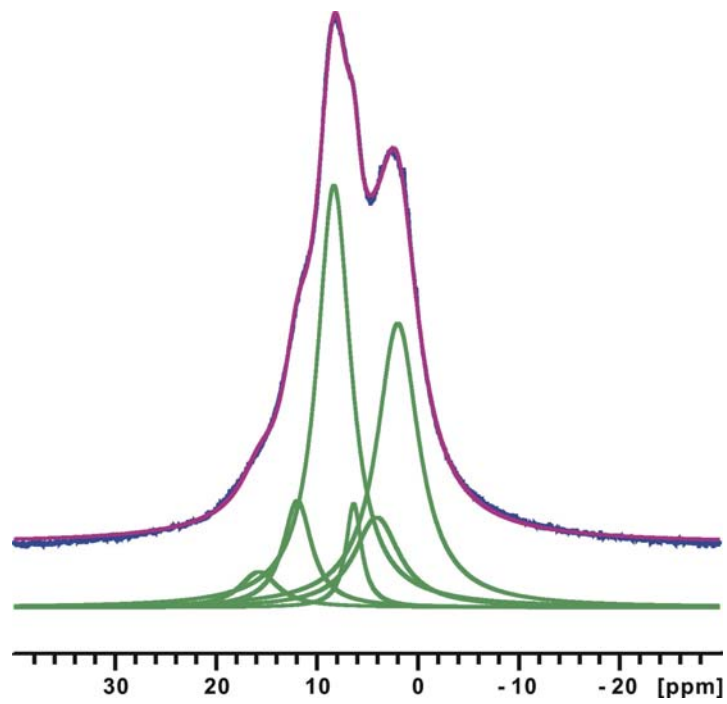


Figure 5.9: Solid state ¹H-NMR spectra of PVPA / SiO₂-Cl-4VP blends.

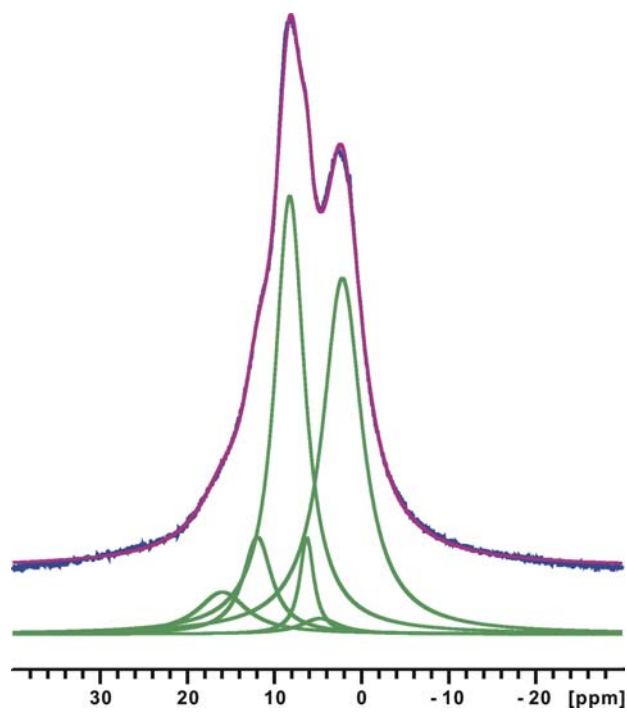
Due to the limited resolution, these peaks are not well separated. However, we can quantitatively determine the content of NH and “free” POH moieties in the composites from the deconvolution of the peaks (see Figure 5.10). The results are listed in Table 5.6.



(a)



(b)



(c)

Figure 5.10: Deconvolution of ^1H -MAS-NMR spectra of (a) BA1, (b)BA3 and (c) BA4.

However, we can see from the spectra that the intensity of the POH peak decreases rapidly with increasing amount of $\text{SiO}_2\text{-Cl-4VP}$ and even disappeared in BA6 ($\text{SiO}_2\text{-Cl-4VP: PVPA}=9:1$), probably, because most of the POH groups have interacted with the pyridine units. In BA6, the peaks of both, POH and NH can not be detected due to their relatively low concentration. We can see that, the number of POH moieties decrease from BA1 to BA4, with increasing $\text{SiO}_2\text{-Cl-4VP}$ content which can explain the decreasing proton conductivities if only the POH protons are considered as mobile charge carriers.

Table 5.6: Percentage of NH and POH existing in BAs over the total number of phosphonic acid units

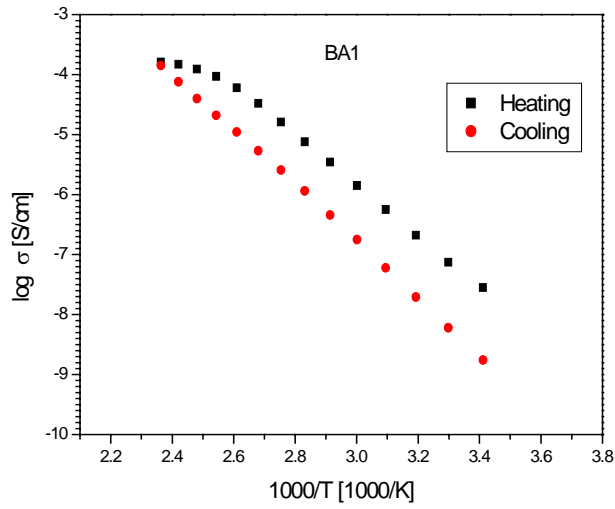
Sample	Molar ratio of VPA (%) [*]	NH (%)	POH (%)
BA1	90	6	94
BA3	70	30	70
BA4	50	42	58
BA6	10	/	/

* Molar ratio of VPA out of total repeat units (VPA+4VP)

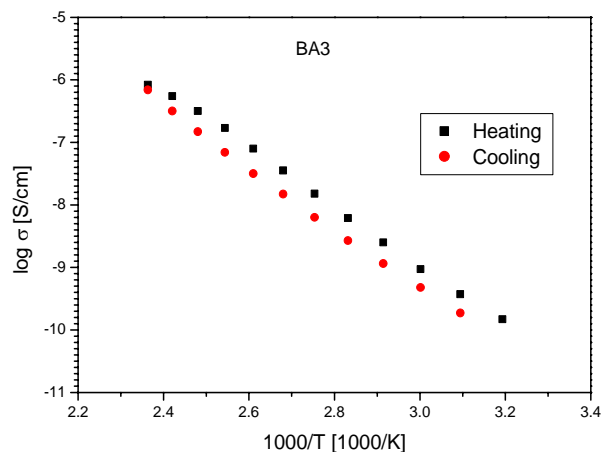
It is well known that phosphonic acid can condense at high temperature and form phosphonic acid anhydride. This reaction eliminates protons as charge carrier and, meanwhile, cause barriers for proton transport which consequently decreases proton mobility.

However, by blending with basic components, part of the POH groups react with basic units to form salts, which prevent themselves from condensing at elevated temperatures. This could be one of the advantages for blending SiO₂-Cl-VP in PVPA.

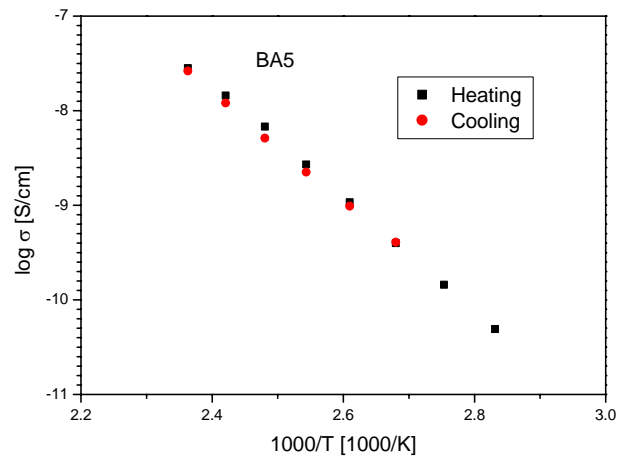
In order to compare the thermal stability of the materials, proton conductivity was measured with a heating-cooling program. We can see from Figure 5.11 that, in BA1, there is big discrepancy of conductivity measured in heating and cooling procedure which is caused by self-condensation of the phosphonic acid groups at high temperatures. However, the discrepancy decreases with increasing SiO₂-Cl-VP content due to the acid-base interactions as discussed above. In BA5, no obvious decrease of conductivity can be detected which means most of the POH groups are bonded to pyridine moieties.



(a)



(b)



(c)

Figure 5.11: Proton conductivity of (a) BA1, (b) BA3 and (c) BA5 measured in heating-cooling cycles.

5.3.2 Proton conduction with humidification

PVPA is a very hygroscopic polymer and can absorb a lot of water until a liquid phase is formed. After blending with SiO₂-Cl-VP, the water uptake is dramatically changed. As we can see in Figure 5.12, even at 100% relative humidity, the absorbed water content is less than 10%, probably because of the chemical and physical crosslinking between the polymer chains.

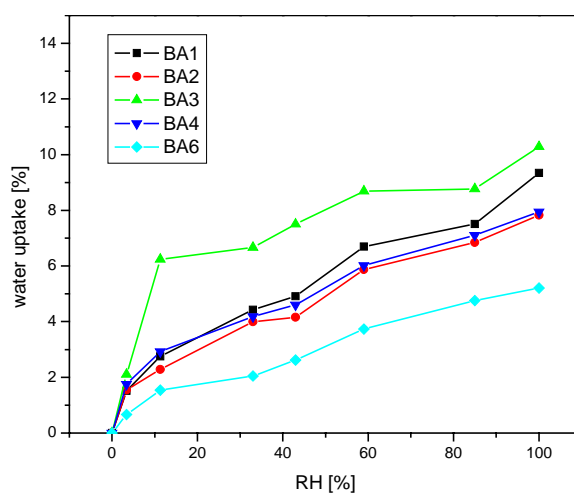


Figure 5.12: Water uptake properties of the SiO₂-Cl-VP/PVPA blends.

The humidity dependence of proton conductivities of SiO₂-Cl-VP/PVPA blends was studied in Figure 5.13. The conductivities were measured with different relative humidities at 25 °C. After being exposed to humidification, all the conductivities increase rapidly with relative humidity. BA1 shows similar conductivity as PVPA which can reach as high as 0.05 S/cm at 90% relative humidity.

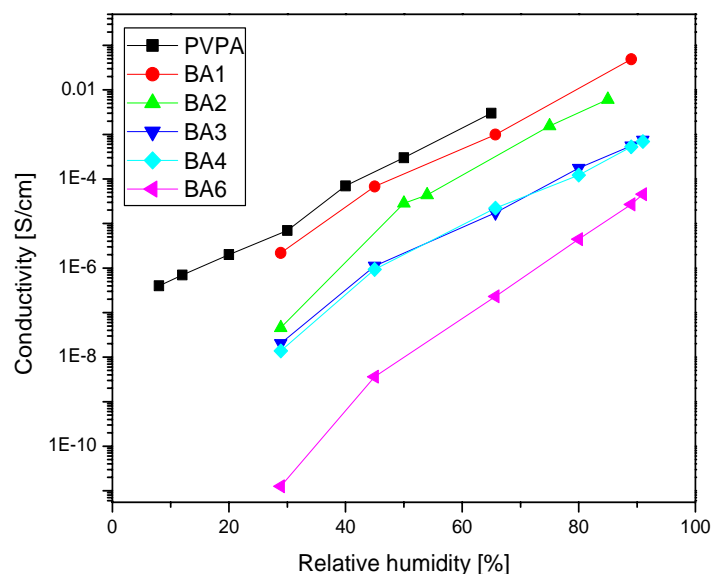


Figure 5.13: Proton conductivity of the SiO₂-Cl-VP/PVPA blends at 25 °C versus relative humidity.

Proton conductivities of BA1, BA2 and BA6 were also measured under 80% relative humidity at different temperatures. BA1 shows very high proton conductivity (0.5 S/cm) at 85 °C under 80% RH. All the conductivities show Arrhenius type behavior because under 80% RH. The activation energies for proton conduction are similar (~40 kJ/mol). The difference of proton conductivity in Figure 5.14 was caused by different free proton concentrations. Normally, the effect of dilution on proton conductivity is slight because the variation of proton concentration is typically within 1 order of magnitude. However in this case, most of the dissociated protons are likely to be trapped by pyridine moieties. Thus, the number of free protons could differ by several orders of magnitude in different composites.

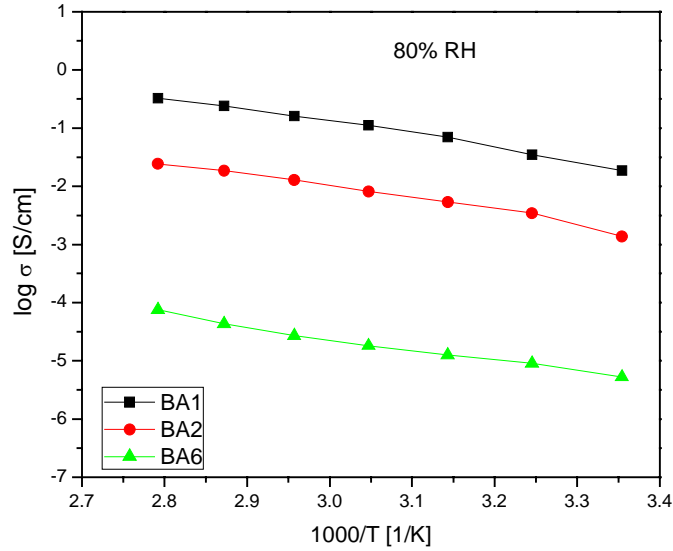


Figure 5.14: Arrhenius plots of conductivities measured under 80% RH.

Figure 5.15 shows the proton conductivities of BA2, BA4 and BA6 measured under 1 bar water vapor at elevated temperatures. For BA6, the conductivity at 120 °C is 1 order of magnitude higher as compared with that at 150 °C, which indicates that the proton conduction of BA6 is more sensitive to water.

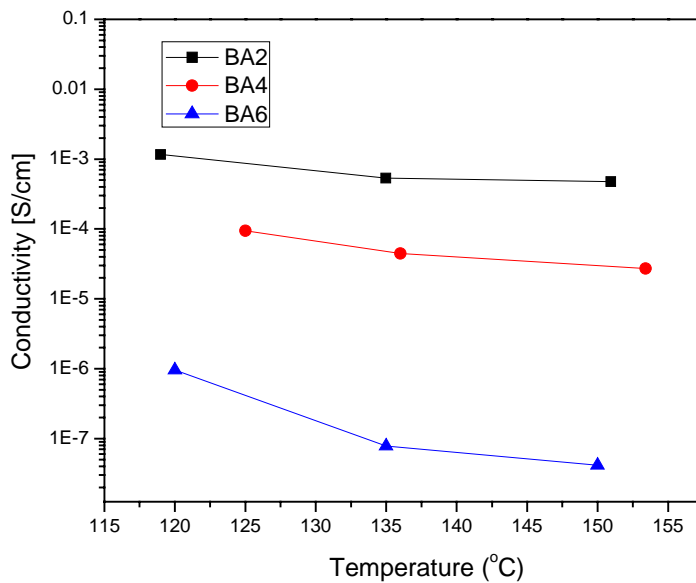


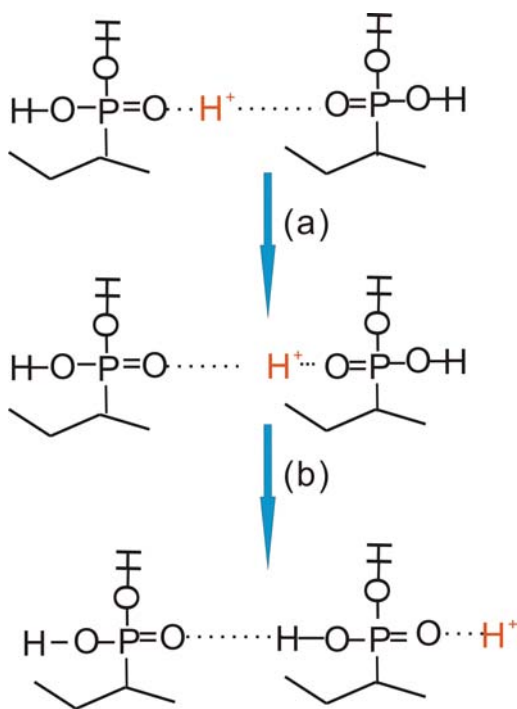
Figure 5.15: Proton conductivities of BA2, BA4 and BA6 measured under 1 bar water vapor at elevated temperatures.

CHAPTER 6

PHASE BEHAVIOR AND PROTON CONDUCTION OF PVPA/PEO BLENDS

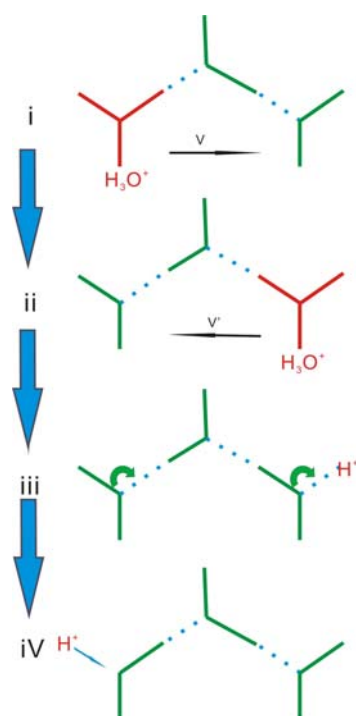
6.1 Introduction

In water free proton-containing solid polyelectrolytes, proton transfer can be carried out only by hydrogen bond breaking and forming processes because there is no mobile species other than protons. In poly(vinyl phosphonic acid), steps for proton migration via Grotthuss mechanism can be as shown in Scheme 6.1: a) displacement of H^+ along a hydrogen bond; b) transport of the H^+ from this hydrogen bond to the following one. ^[1,2]



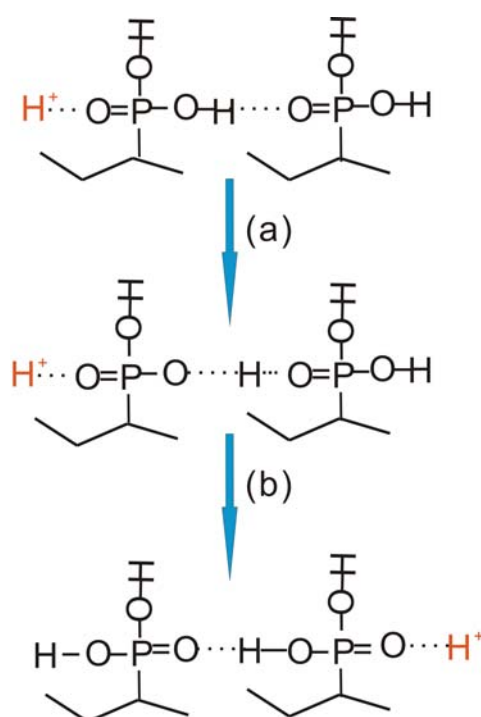
Scheme 6.1: Proton transport between phosphonic acid moieties.

In order to understand step b, Bjerrum defects were postulated in Bjerrum theory of ice conductivity.^[3] In this theory, the doubly occupied sites (D defects) and empty sites (L defects) are postulated. The necessity of having Bjerrum defects for the proton transport via hydrogen bonds is illustrated in Scheme 6.2. From (i) to (ii), two H^+ transfers occur simultaneously, in a chain sequence under an applied field V . However, in (ii), the displacement results in a creation of a reverse applied field V' , which induces the protons to hop back to their original position. Consequently, long-distance H^+ diffusion cannot occur. Consider now, the rotation of the molecules is allowed which creates a pair of L and D defects in adjacent hydrogen bond positions and on departure of H^+ from the vicinity of this L, D couple, the V' field is destroyed. Conduction can continue and the arrival of a new H^+ from the left (iv) restores the chain element into its original position. According to this theory, rotation of phosphonic moieties is necessary for proton transport in Scheme 6.1 b.



Scheme 6.2: Proton transport mechanism postulated in Bjerrum theory.

Another possible approach of proton transport in PVPA is shown in Scheme 6.3. With receiving a proton from the left side, the electronic shell of the phosphonic acid moiety shifts to the left side; the proton in the middle moves to the right side (Step a). Reorganization of the chemical bonds happens as a result of redistribution of the electrons; a proton is formed on the right side (Step b). In this procedure, molecule rotation is not involved.



Scheme 6.3: Approach of proton transport in PVPA without molecule rotation.

In both approaches, the dynamics of the hydrogen bond network is indispensable for proton conduction but in different ways. In solid polyelectrolytes, thermal induced chain motion and/or side group rotation can be expected to enhance the dynamics of hydrogen bond network. PVPA was considered to be one of the most promising anhydrous proton conductors due to the very high density of phosphonic acid moieties. However, the proton conductivity of PVPA was not as high as expected and the

activation energy was around 60 kJ/mol. ^[4] Comparing with liquid phosphonic acid which has very high proton conductivity and low activation energy, the discrepancy is probably caused by the limitation of molecular motion.

PEO has a very low glass transition temperature (-19 °C) and contains abundant oxygen atoms in the backbone chain which can form hydrogen bonds with phosphonic acid groups. These characteristic properties were considered to be helpful to build a dynamic hydrogen bond network in PVPA/PEO blends.

Miscibility of polymers is of great importance for properties such as thermal, mechanical, dielectric, and optical. The miscibility of PVPA and PEO has not been studied yet. The phase behavior of PVPA/PEO blends and the effect of blending on proton conductivity will be studied in this chapter for the first time, as to my knowledge.

6.2 Thermal analysis of PVPA and PEO blends

In the following discussion, the abbreviation of PVPE refers to PVPA/PEO polymer blends. For example, PVPE (10% PEO) means the PVPA/PEO blend contains 10% PEO by weight ratio. Figure 6.1 is the result of the TGA measurement of pure PEO and PVPEs with various compositions. In the TGA curves, there are two degradation peaks. The first step refers to the degradation of PEO and the second step comes from the degradation of PVPA. We can see that the PVPEs are stable until 250 °C. After blending with PVPA, the degradation temperature of PEO decreases as compared with pure PEO which indicates that PEO is less thermally stable under

acidic environment. This could be a hint of the interaction between PVPA and PEO.

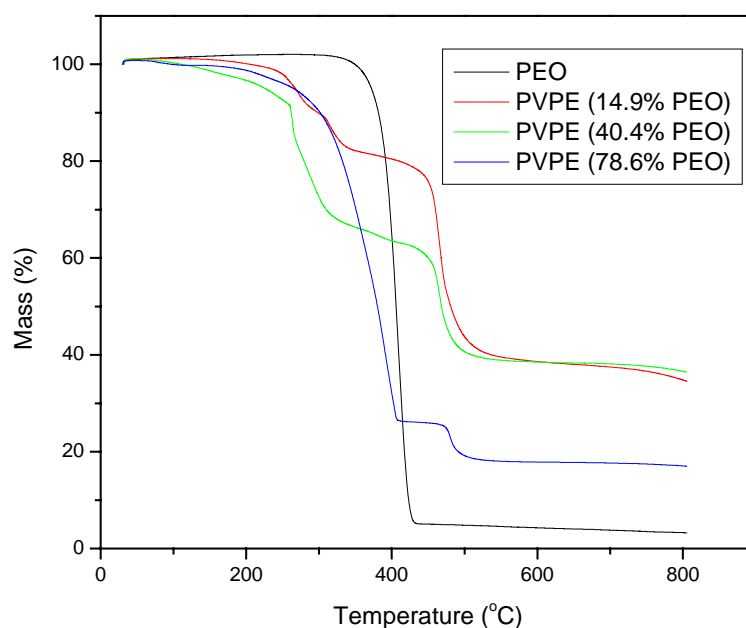


Figure 6.1: TGA curves of PEO and PVPA/PEO blends measured in nitrogen atmosphere.

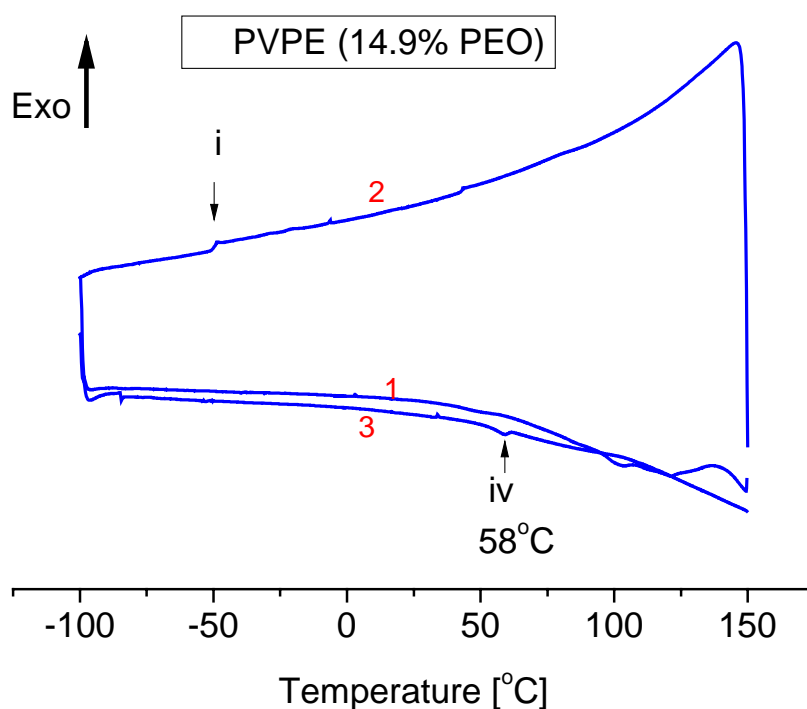
Differential scanning calorimetry DSC can be used to measure a number of characteristic properties of a sample. Using this technique, it is possible to observe fusion and crystallization events as well as glass transition temperatures (T_g). Glass transitions may occur as the temperature of a polymer melt decreases. These transitions appear as a step in the baseline of the recorded DSC signal. This is due to the sample undergoing a change in heat capacity when transformed from glassy to melt state, as the temperature increases. A melt has a higher heat capacity than a glass. In special cases, when a crystallizable polymer has been quenched to form a glassy solid, temperature increase may lead to spontaneous crystallization. At some point the

molecules may obtain enough freedom of motion to spontaneously arrange themselves into a crystalline form. This is known as the recrystallization temperature. This transition from amorphous solid to crystalline solid is an exothermic process, and results in an exothermic peak in the DSC signal. As the temperature increases the sample eventually reaches its melting temperature (T_m). The melting process results in an endothermic peak in the DSC curve. The ability to determine transition temperatures and enthalpies makes DSC an invaluable tool in producing phase diagrams for various chemical systems.

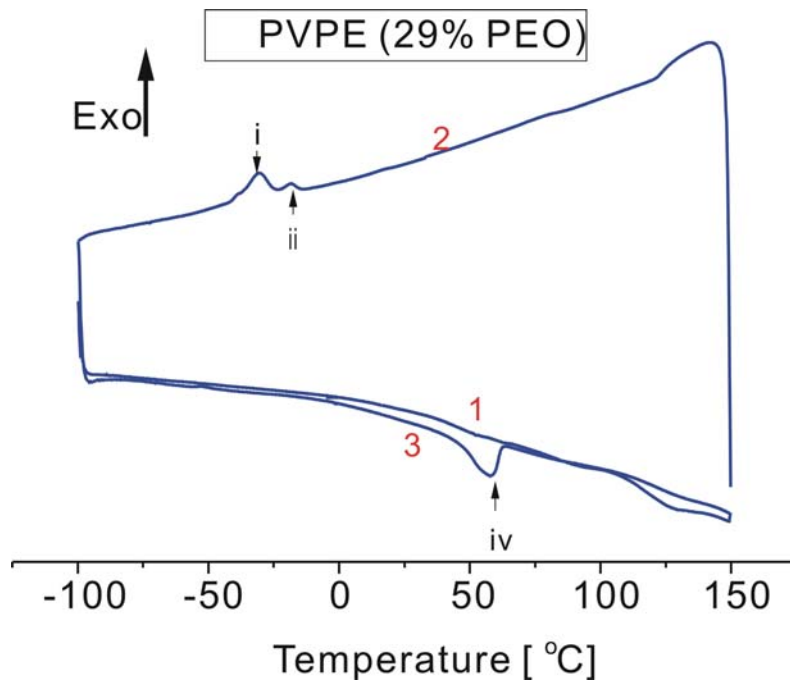
PVPA/PEO mixtures have been prepared by using water as the common solvent of PVPA and PEO. The samples for DSC measurements were dried by freeze-drying. During the DSC measurement, the samples were first heated to 150 °C (first scan) and then quenched to -100 °C (second scan) followed by the third scan (heating to 150 °C again). The DSC results are shown in Figure 6.2. There is no melting temperature of ice in all DSC curves. Therefore, it can be considered that no free water is contained in the samples.

PVPEs with low PEO content shows no peak in the first scan (See Figure 6.2(a, b)). In the second scan, one (Figure 6.2 (a)) or two exothermic peaks (Figure 6.2(b)) (peak i and ii) appear between -50 °C and -10 °C. Peak iv in the third scan is the melting peak of crystalline PEO. The total integration of peak i and ii equals to that of peak iv which indicates that crystalline PEO is formed during the cooling procedure and both peak i and ii are recrystallization peaks of PEO. However, the reason for the different crystallization temperatures (peak i and ii) is not clear yet.

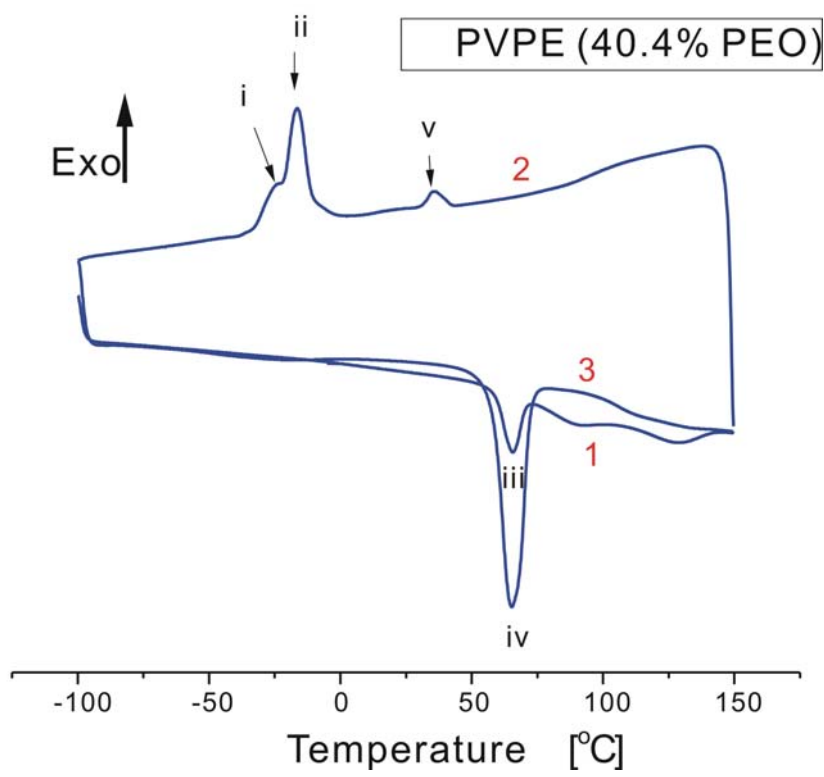
In Figure 6.2(c-e), the endothermic peak in the first scan around 60 °C (peak iii) is the melting peak of the PEO crystals which originally exist in the blends. In the second scan three crystallization peaks are observed. The integration of peak v is close to that of peak iii, which proves that the crystalline PEO crystallized in peak v is the part molten in peak iii. The total integration of the exothermic peaks (i+ii+v) is the same with that of peak iv. WAXS was applied to investigate the structure of PVPE (40.4% PEO) in the process of cooling from 90 °C to -50 °C. The result is shown in Figure 6.3. At 90 °C, the broad peak shows that there is no crystal structure in the blend; being quenched to 30 °C, the crystal structure of PEO appears and no other crystal structure appears at -50 °C. Together with Figure 6.2 (c), it can be confirmed that all of the exothermic peaks result from crystallization of PEO. The difference in crystallization temperature probably results from different droplet size and (or) shape.



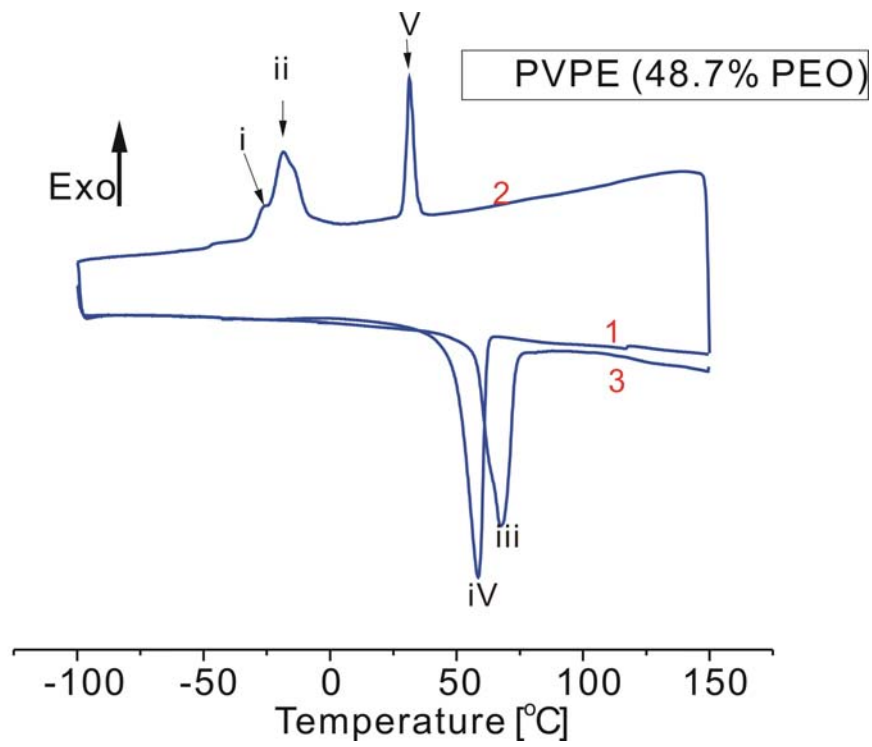
(a)



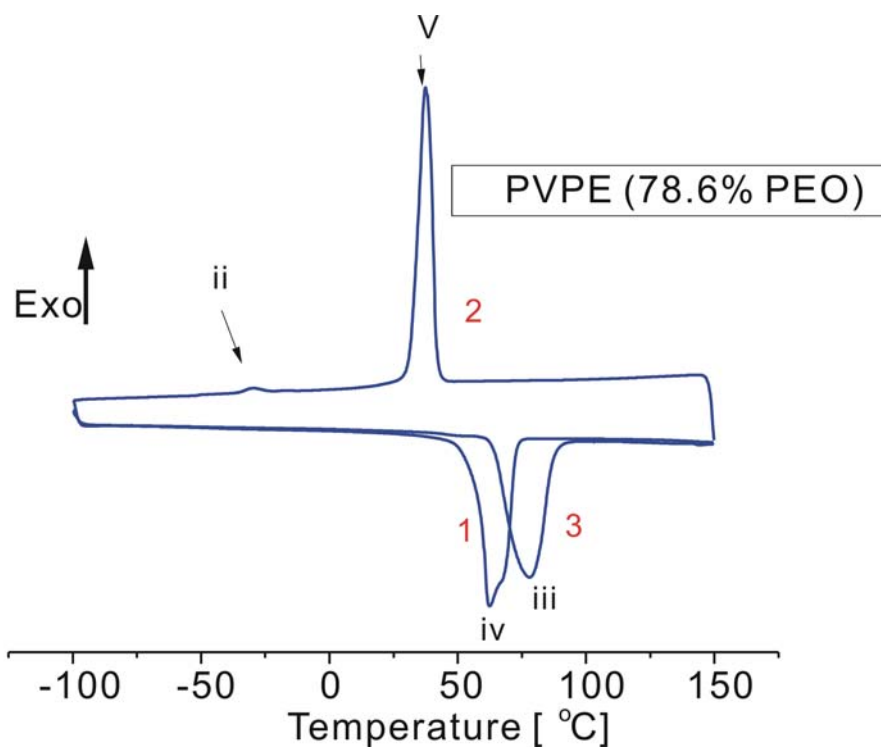
(b)



(c)



(d)



(e)

Figure 6.2: DSC curves of PVPE with various PEO contents.

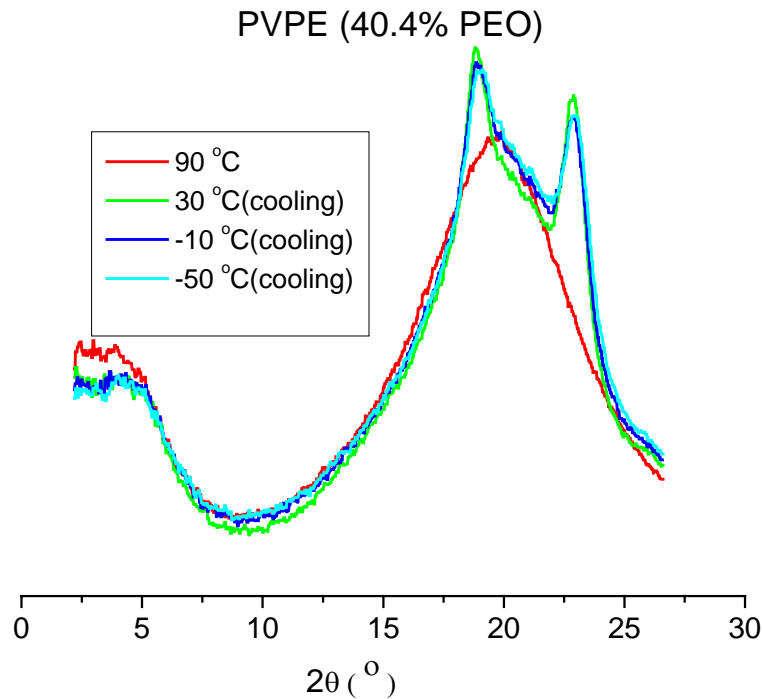


Figure 6.3: WASX of PVPE (40.4% PEO) at various temperatures.

Based on the above discussion, it can be conclude that,

a) With low PEO contents:

(1) PVPA and PEO are miscible and homogeneous PVPA/PEO mixtures can be obtained.

(2) The mixture described in (1) is metastable and phase separation can occur at $T=T_c$ (T_c is the critical temperature of phase separation), which leads to small PEO droplets dispersed in the PVPA matrix. When $T>T_m$, the PEO droplets are amorphous.

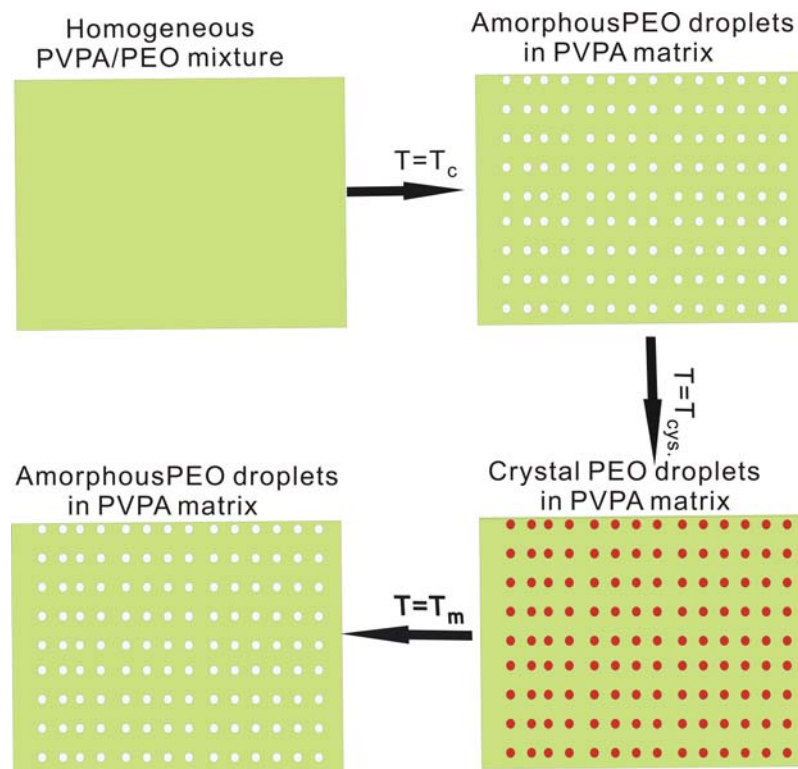
(3) The chain mobility of PEO within these droplets is restricted by the PVPA chains. Moreover, there should be hydrogen bonding on the interphase between the PEO phase and the PVPA phase. These two factors result in the two crystalline peaks (peak i and ii) at low temperatures (below -10°C) when being quenched to -50°C .

PEO crystal forms in the PEO droplets.

(4) Being heated to $T > T_m$, the PEO crystal melts.

(5) Phase separation is irreversible.

These processes are schematically shown in scheme 6.4.



Scheme 6.4: Schematic illustration of phase behavior of PVPE with low PEO content

b) With high PEO contents (< 50 wt%)

(1) PVPA and PEO are partially miscible. Homogeneous PVPA/PEO mixture and PEO crystal in the pure PEO phase coexist.

(2) The PVPA/PEO mixture is metastable and further phase separation occurs at $T = T_c$ ($T_c > T_m$), small amorphous PEO droplets disperse in PVPA matrix and the original PEO phase becomes amorphous.

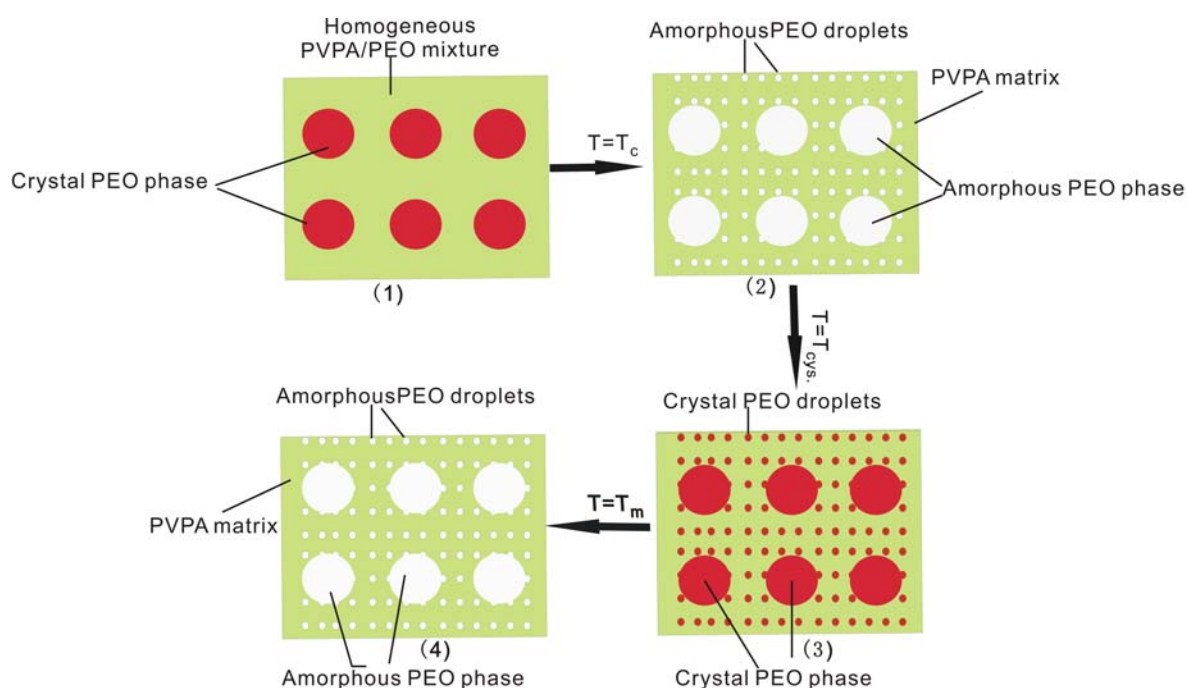
(3) Being quenched to -50 °C, crystalline PEO in the small droplets occurs at low

temperatures (below $-10\text{ }^{\circ}\text{C}$) (peak i and ii). PEO in the original pure PEO phase crystallizes at round $40\text{ }^{\circ}\text{C}$ (peak v).

(4) Being heated to $T=T_m$, the PEO crystal melts. Both small and large coexist in the blends.

(5) Phase separation is irreversible.

These processes are schematically shown in scheme 6.5.



Scheme 6.5: Schematic illustration of phase behavior of

PVPE with high PEO content (<50 wt%)

6.3 Phase diagram of PVPA and PEO blends

6.3.1 Phase separation observed by optical microscopy

Film-samples for optical microscopy were casted on a glass substrate. Diluted solutions of PVPA and PEO in water were used for casting. Afterwards, the glass

substrates were flushed with dry nitrogen for 1 week and then dried under vacuum (10^{-2} mbar) for several days in order to remove the solvent completely.

Figure 6.4 shows the image of a PVPE (31% PEO) membrane observed via the optical microscope in the polarized mode. At 20 °C, the membrane was homogeneous and transparent. After being heated to 140 °C, heterogeneity of the membrane was observed. A similar phenomenon can be observed in the blends with various PEO contents less than 50 wt%, but phase separation occurs at different temperatures (See Figure 6.5). When the PEO content exceeds 50%, PEO crystals can be observed at 20 °C without any annealing history. Figure 6.6 is an example with 78.6 wt% PEO in the blends. At 20 °C, the membrane is opaque and filled with PEO crystals (Figure 6.6 (a)). When heated to 64 °C, the PEO crystal melts (Figure 6.6 (b)). However, the heterogeneity of the membrane remains even at 150 °C (Figure 6.6 (c)). Therefore, phase separation (if there is) cannot be observed in the PVPA/PEO mixture with more than 50 wt% PEO.

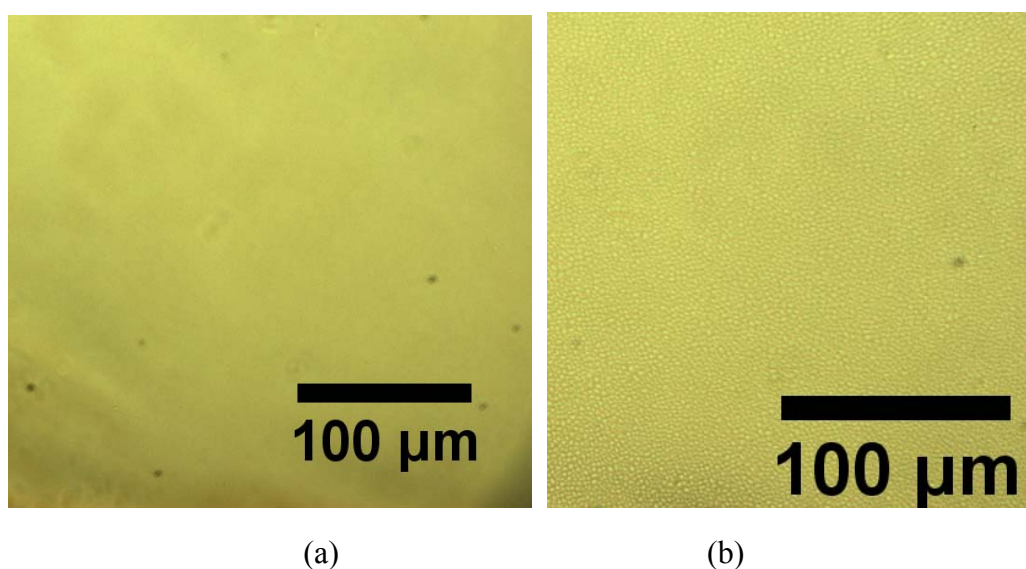


Figure 6.4: Polarized optical images of PVPE (31% PEO) at (a) 20 °C and (b) 140 °C respectively.

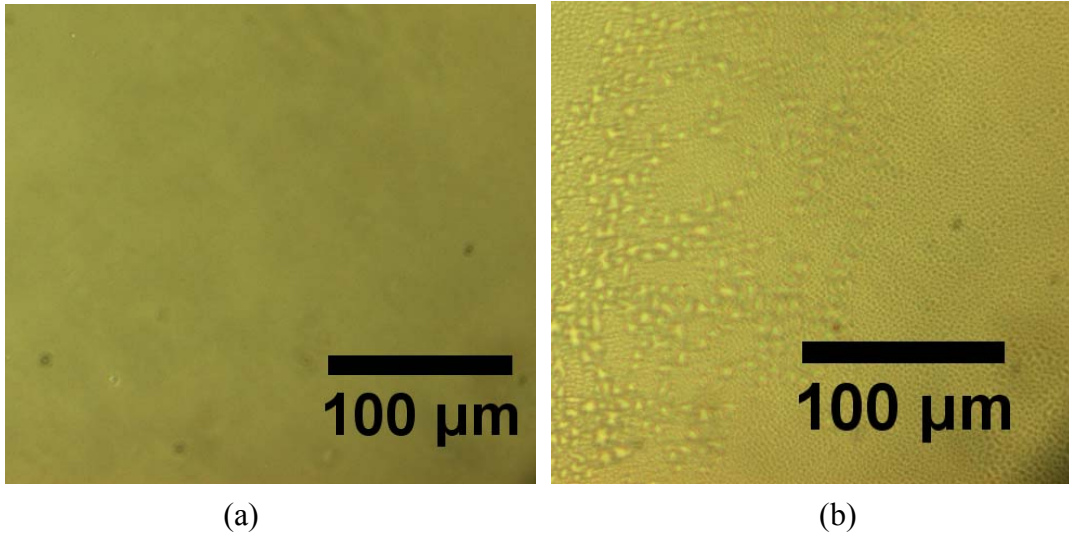
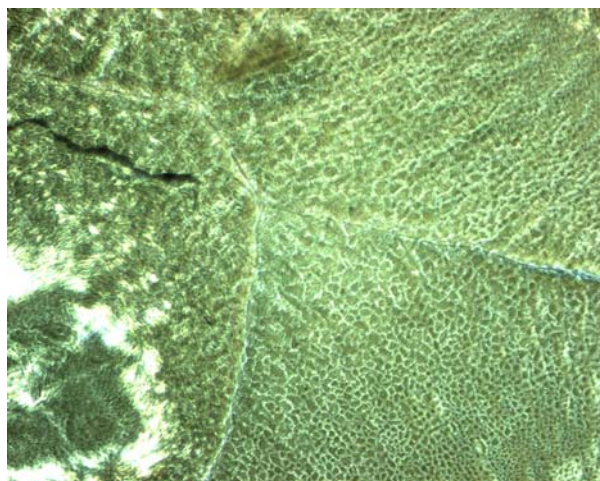
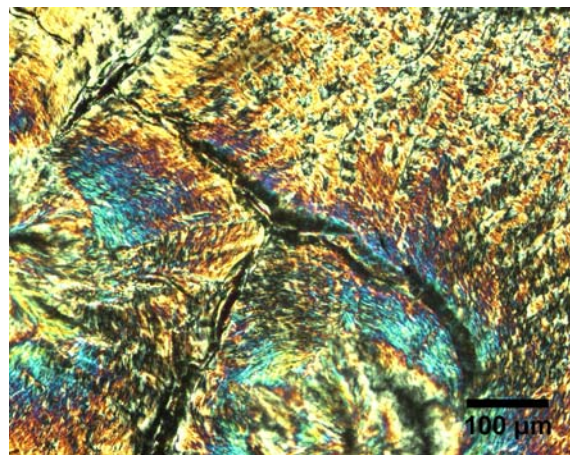
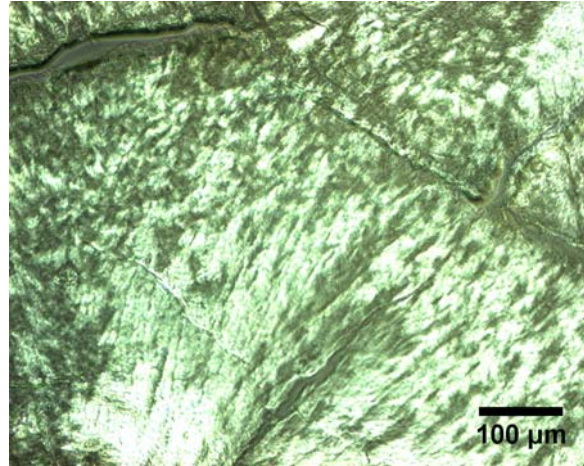


Figure 6.5: Polarized optical images of PVPE (43% PEO) at (a) 20 °C and (b) 101 °C respectively.





(c)

Figure 6.6: Polarized optical images of PVPE (78.6% PEO) at (a) 20 °C, (b) 64 °C and 150 °C, respectively.

6.3.2 Phase separation observed by DSC

As discussed in section 6.2, the mixture of PVPA and PEO was metastable. Phase separation can be induced at high temperatures. As a result, a crystallization peak of the separated PEO droplets can be detected below -10 °C. This phenomenon provides a hint of phase separation in PVPE membranes.

The temperature program for DSC measurement is like this:

- 1) Increase the temperature from -50 °C to a temperature T_1 and then cool down back to -50 °C (T_1 cycle);
- 2) Run another cycle to a temperature T_2 which is a little bit higher than T_1 (T_2 cycle);
- 3) Move on to higher temperatures cycles until the crystallization peak appears in the cooling procedure. (See Figure 6.7)

The temperature cycle in which the crystallization peak firstly appears is the

temperature at which phase separation starts (T_c). When $T > T_c$, the intensities of the crystallization peaks increase with temperature (see Figure 6.7-6.11), because phase separation is a relaxation phenomenon and the extent of phase separation increases with time and temperature. In Figure 6.8 and Figure 6.9, the crystallization peak at the relatively lower temperature shifts toward the one at higher temperature. This happens because with further phase separation, the PEO droplets become more homogeneous in size and morphology.

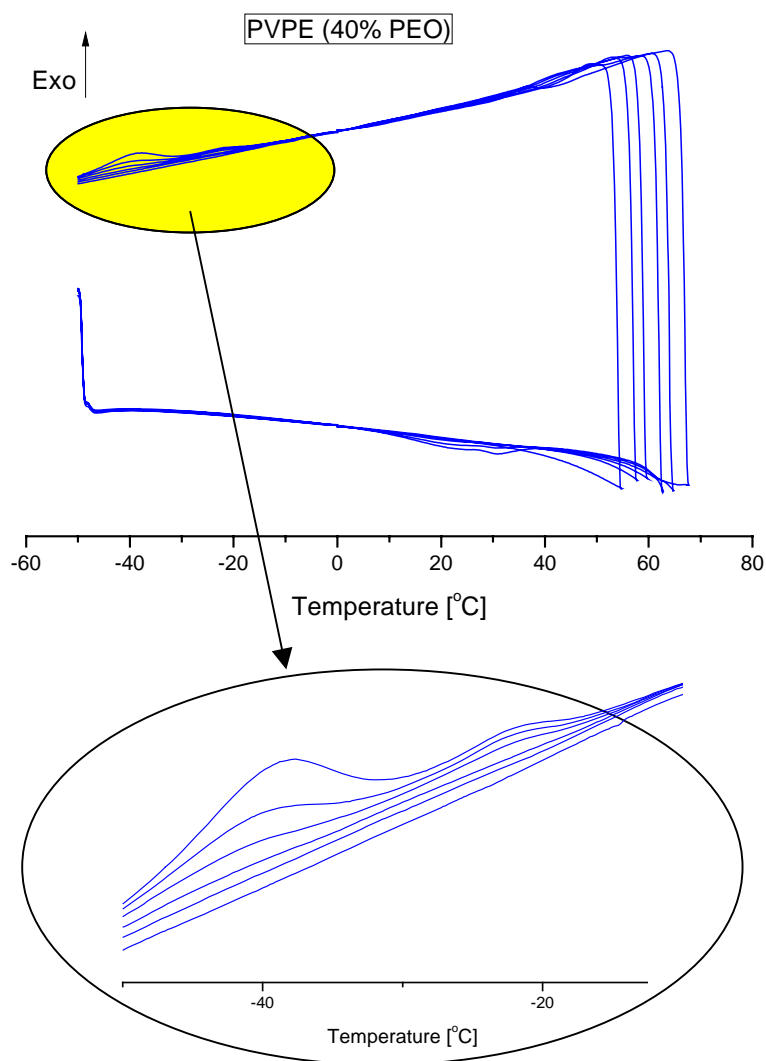


Figure 6.7: DSC curves of PVPE (40% PEO) measured in increasing temperature

cycles.

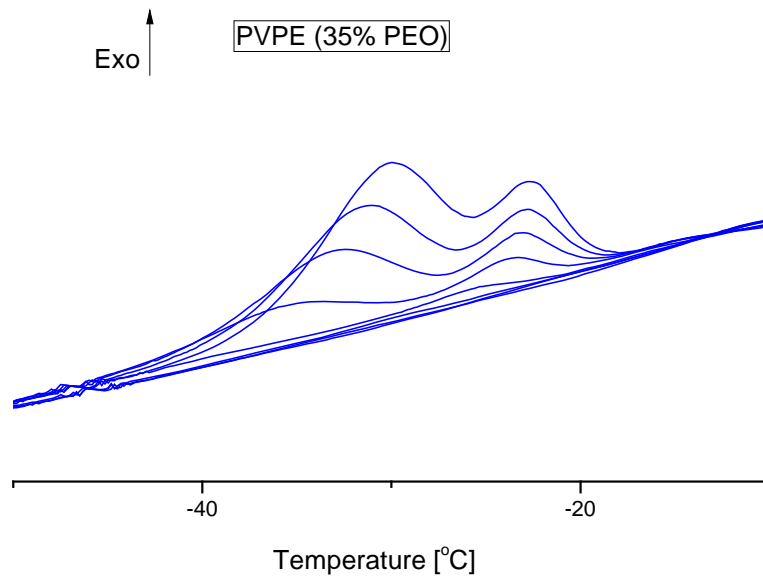


Figure 6.8: DSC curves of PVPE (35% PEO) measured in increasing temperature

cycles.

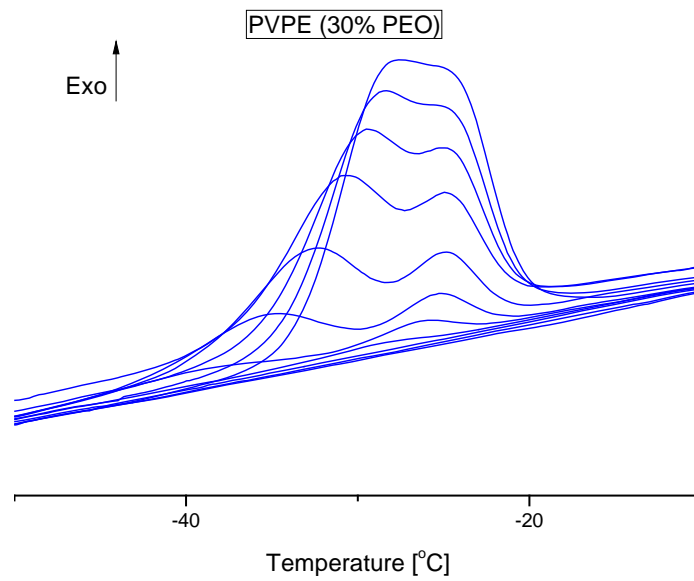


Figure 6.9: DSC curves of PVPE (30% PEO) measured in increasing temperature

cycles.

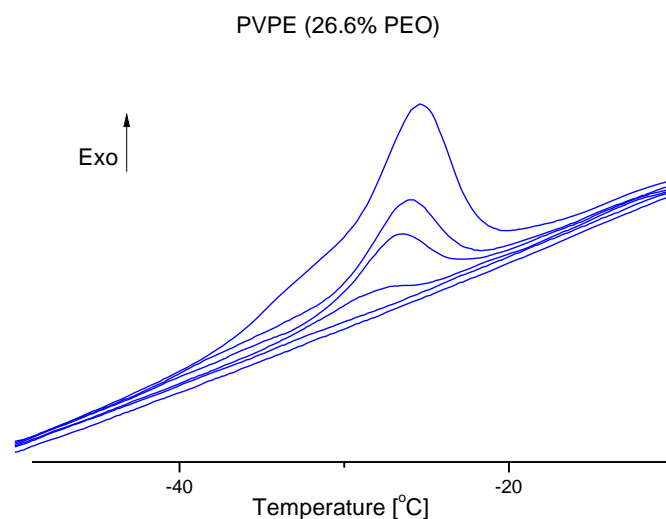


Figure 6.10: DSC curves of PVPE (26.6 % PEO) measured in increasing temperature cycles.

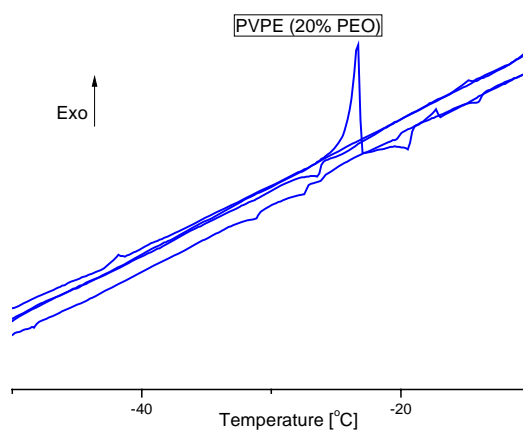


Figure 6.11: DSC curves of PVPE (20 % PEO) measured in increasing temperature cycles.

In Figure 6.10 and 6.11, phase separation occurs at high temperatures. The PEO droplets formed at high temperatures are more homogeneous than that formed at low temperatures. Therefore, only one crystallization peak was detected in Figure 6.10 and 6.11.

On the basis of phase separation temperatures observed via optical microscopy

and DSC, the phase diagram of PVPA/PEO blends was plotted in Figure 6.12. The region below the boundary is the one-phase region in which PVPA/PEO mixtures are miscible and homogenous PVPA/PEO membranes can be obtained; the region above the boundary is named two-phases region in which phase separation occurs, PVPA and PEO are immiscible. The red boundary was plotted according to the temperatures at which phase separation can be observed in the optical microscope. The black boundary was plotted according to the DSC result. The discrepancy of the two boundaries may result from the different scale at which phase separation was detected, and the lower scanning rate of DSC.

Phase separation observed by optical microscopy is of micrometer scale. With the same heating rate, the temperature for phase separation of micrometer scale is much higher than that of nanoscale. DSC is more sensitive than optical microscope for detecting phase separation. Whenever phase separation happens, it can be detected by DSC, even in the nanoscale. This explains why the phase separation temperature obtained by optical microscopy is much higher than that measured by DSC.

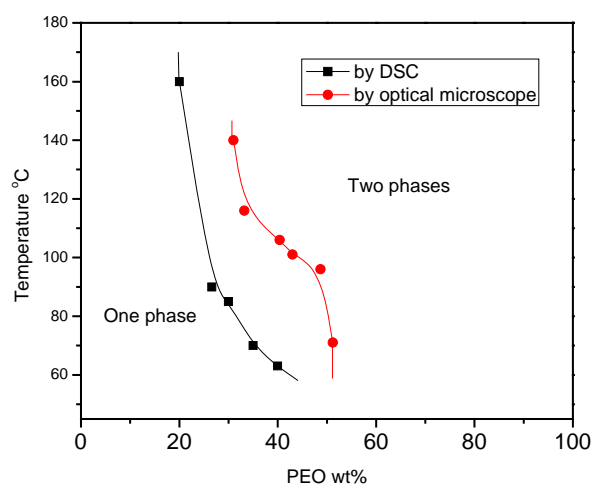


Figure 6.12: Phase diagram of PVPA/PEO blends plotted via DSC (black) and optical microscopy (red)

6.4 Proton Magic-Angle-Spinning NMR

Nuclear magnetic resonance spectroscopy (NMR) is a powerful tool to determine local structural arrangements as well as dynamics. Particularly, high resolution ultrafast proton magic-angle-spinning NMR (^1H MAS NMR) provide specific information on hydrogen bonding and various chain motions.

Proton mobility is a precondition for proton conduction. In fully solid state polyelectrolytes, proton motion is always connected with various chain motions. Therefore the detection of local chain dynamics is of great importance to understand the proton transport mechanism.

A 850 MHz NMR spectrometer was applied to study the local dynamics of the PVPA/PEO blends. ^1H MAS NMR spectra of PVPA, PEO and their blends with various compositions are shown in Figure 6.13. The peak at 10.6 ppm is the resonance peak of the proton from POH groups. The peak at around 3.8 ppm derives from CH_2 of PEO. The broad peak at 2.2 ppm refers to CH_2 and CH from the PVPA backbone chains. We can see that the CH_2 peak from PEO is very sharp which indicates fast chain motion of the PEO backbone chains. However, the resonance peak from the PVPA backbone chain is broad as compared with PEO which shows poor mobility of PVPA chains.

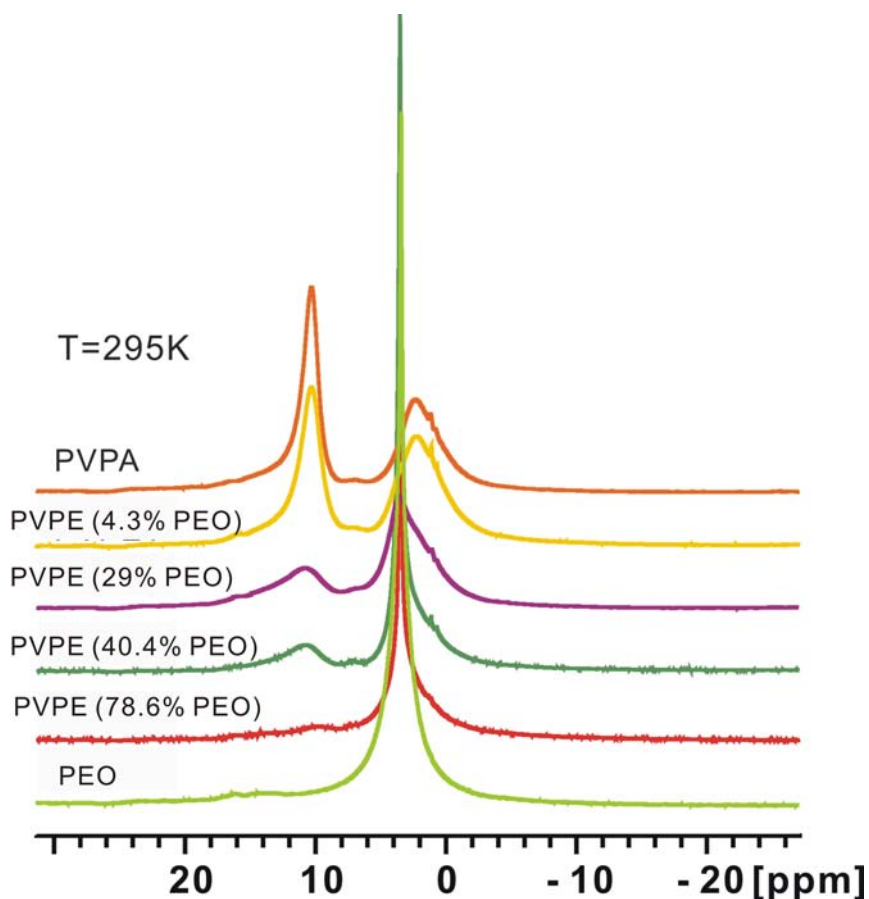


Figure 6.13: ^1H MAS NMR spectra of PVPEs at 25 °C

^1H MAS NMR spectra of PVPA measured with increasing temperatures are shown in Figure 6.14. The peak of the POH narrows with increasing temperature which means improved proton mobility at high temperatures. This proton motion is caused by rotation of the side groups. However, the peak from the PVPA backbone chain does not change with temperature because PVPA is still in the glassy state; motion of PVPA main chains is impossible.

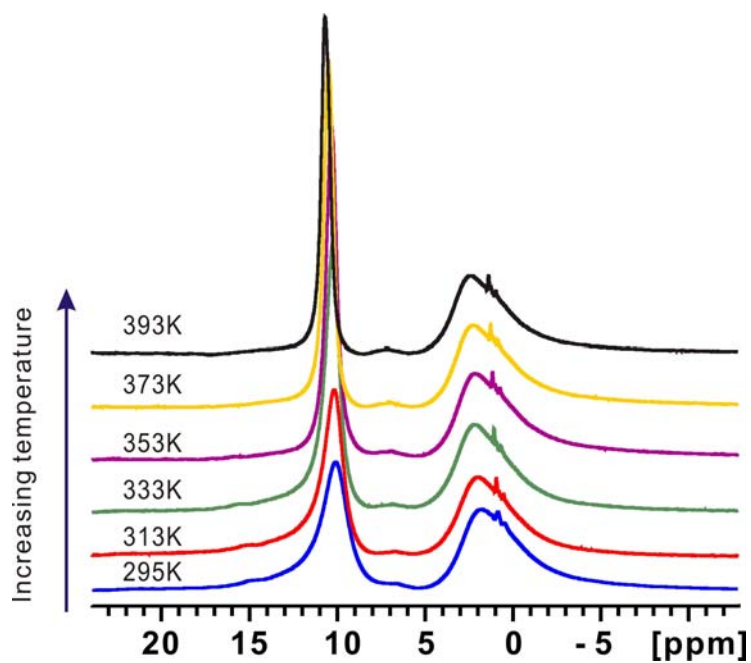


Figure 6.14: ^1H MAS NMR spectra of PVPA measured with increasing temperature.

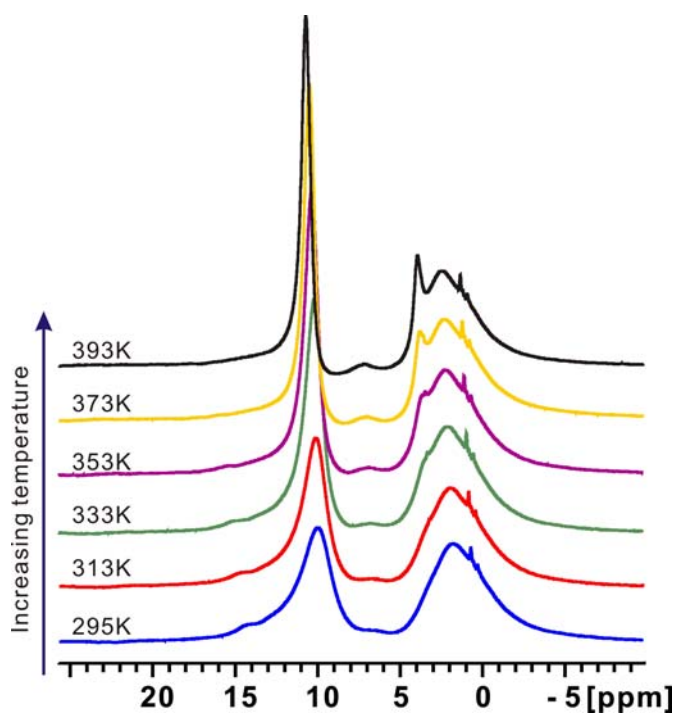


Figure 6.15: ^1H MAS NMR spectra of PVPE (4.3% PEO) measured with increasing temperature.

^1H MAS NMR spectra of PVPE (4.3% PEO) measured with increasing temperature is shown in Figure 6.15. At 295K, the CH_2 peak from PEO is embedded in the broad peak of PVPA main chain. Due to the good miscibility of PVPE (4.3% PEO), the PEO chains are surrounded by PVPA chains. Hydrogen bonding between PVPA and PEO chains is predictable. Therefore, the mobility of PEO chains is restricted which leads to a broad peak overlapped with PVPA. At elevated temperatures, the mobility of PEO main chain increases; the peak becomes sharp and narrow. The peak of PVPA main chain remains broad due to its limited mobility. After the heating procedure, the sample was cooled down to 300K, the sharp peak of PEO disappeared which means this phenomenon is reversible in PVPE (4.3% PEO) (see Figure 6.16).

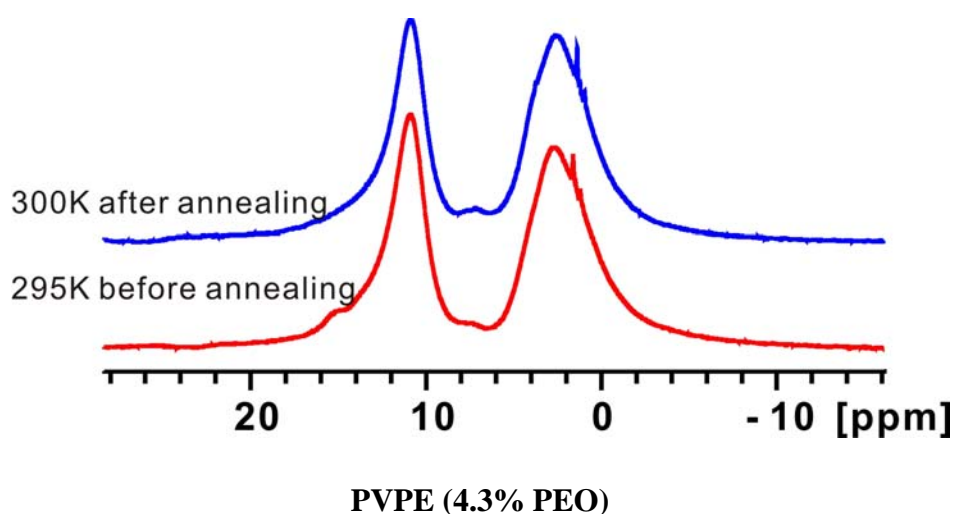


Figure 6.16: ^1H MAS NMR spectra of PVPE (4.3% PEO) before and after annealing.

With PVPE (29 % PEO), the mobility of the PEO chains also increase with temperature (Figure 6.17 (a)). In the cooling procedure, the mobility of the chains decrease and the peaks become broad again. However, the peaks of the PEO chains

remain sharp (Figure 6.17 (b)). Figure 6.18 shows the ^1H MAS NMR spectra of PVPE (29% PEO) before and after annealing. We can find that after annealing at 120 °C, the peak of the PEO is sharper than that before annealing which means that the mobility of the PEO chain is irreversibly improved. According to the phase diagram in Figure 6.12, phase separation in PVPE (29% PEO) has already happened at 120 °C which is irreversible either. Both results may be interpreted such, that annealing leads to increased phase separation which leads to improved PEO chain mobility.

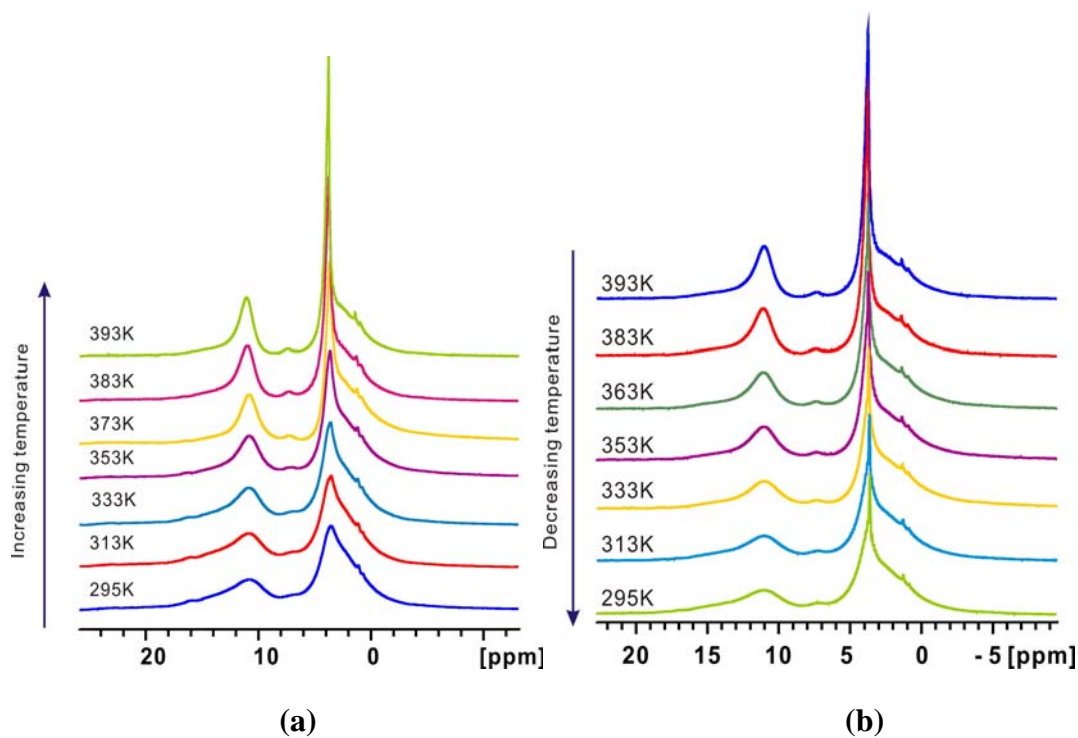


Figure 6.17: ^1H MAS NMR spectra of PVPE (29% PEO) measured in (a) heating and (b) cooling procedure.

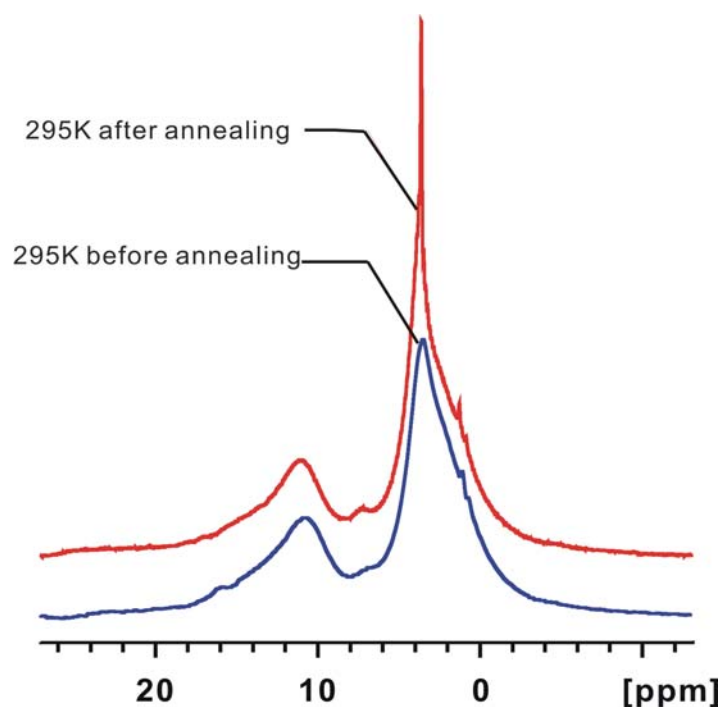
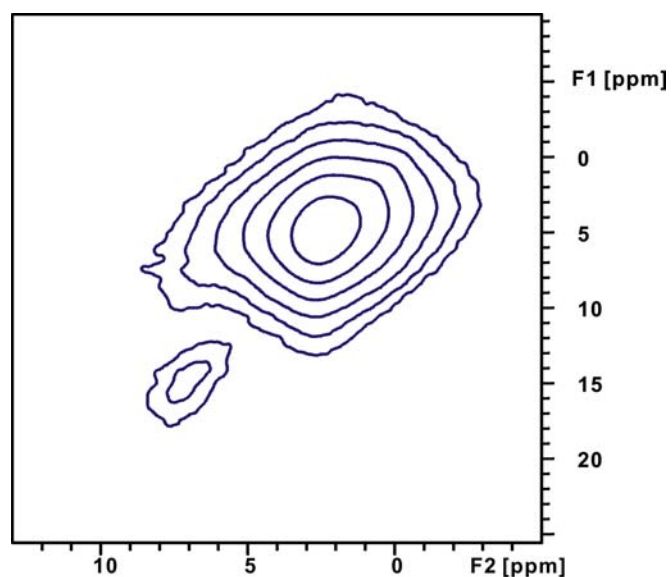


Figure 6.18: ^1H MAS NMR spectra of PVPE (29% PEO) before and after annealing.

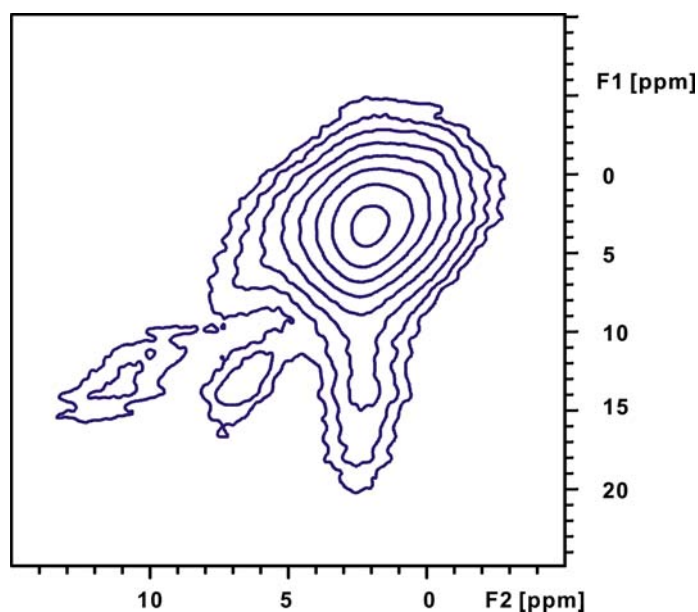
Double-quantum (DQ) NMR spectroscopy under ultrafast magic angle spinning of solids is a new tool to investigate hydrogen bonded structures in the solid state. ^[5-9]

^1H DQ/SQ correlation spectra of PVPA are shown in Figure 6.19. Rotor-synchronized back-to-back (BABA) block is used to excite the double quantum transition, which contains four 90° pulses during each rotational period. ^[10-12] The MAS frequency is 29,762 Hz. The spectra are recorded at 293 (a) and 233 K (b), respectively. The diagonal cross peaks at 2.5 ppm and 7.0 ppm correspond to self-correlation of the aliphatic protons from the PVPA main chain and aromatic protons from the end groups (diphenylethylene from anionic polymerization), respectively. Due to the fast mobility of the phosphonic acid group at room temperature, the dipolar couplings are reduced greatly and we cannot see the spatial proximities between the POH (10.6 ppm) and other protons. However, at low

temperature (233 K), as shown in Figure 6.19 b, the cross peak between POH and the aliphatic protons appears which demonstrates that the mobility is reduced of both the POH and the side group at low temperatures. The spatial proximity can be seen from the ^1H DQ/SQ correlation spectrum. The result shown in Figure 6.19 proves the fast motion of phosphonic acid side groups.



(a)



(b)

Figure 6.19: ^1H DQ/SQ correlation spectra of PVPA measured at (a) 293K and (b) 223K.

6.5 Proton conduction of PVPA/PEO blends

Anhydrous proton conductivities of PVPA/PEO blends measured in heating-cooling cycles are shown in Figure 6.20. All the samples were annealed at 50 °C under vacuum (10^{-2} mbar) for one week before measurement in order to remove residual water. The measurements were performed in a dry nitrogen atmosphere. We can see in Figure 6.20 that the proton conductivity decreases with increasing PEO content in the mixture. The lower conductivity in the cooling procedure may be due to the self-condensation of the phosphonic acid groups. All of the conductivities show Arrhenius type of behavior. For each sample, the activation energies in both heating and cooling process are exactly the same which means in these cases, self-condensation only changes the number of “mobile protons” but not the mobility. Here the “mobile protons” refers to the protons that can contribute to conductivity. In heterogeneous materials, the number of protons that can contribute to conductivity is only a small part of the total numbers. For example, in PVPA, the “mobile protons” are those which can be transported within a long distance via a dynamically hydrogen-bond network. A major part of the phosphonic acid groups are separated with each other and hardly can participate in proton conduction. Unfortunately, self-condensation prefers to happen between neighboring phosphonic acid moieties which are linked via H-bonds. As a result, some “mobile protons” vanish in the reaction when heated above 100 °C and some of them become “dead” due to the position barrier result from the formation of the phosphonic acid anhydrides. Therefore, the effect of self-condensation on proton conductivity is more notable than

can be expected, simply on the basis of charge carrier numbers.

The proton conduction activation energies were calculated from the Arrhenius plots in Figure 6.20 and shown in Figure 6.21. In figure 6.21, we can find that the activation energy increases with PEO content which obviously shows that PEO blocks the proton conduction in PVPA/PEO blends.

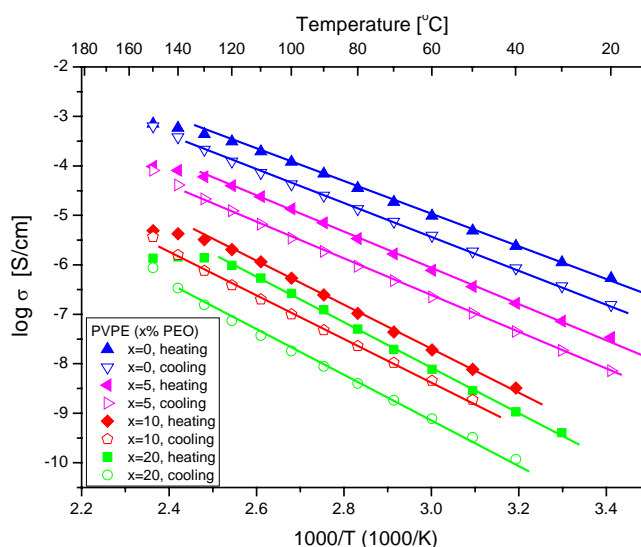


Figure 6.20: Arrhenius plots of proton conductivities of PVPA/PEO blends measured in dry conditions. (Solid: heating, hollow: cooling)

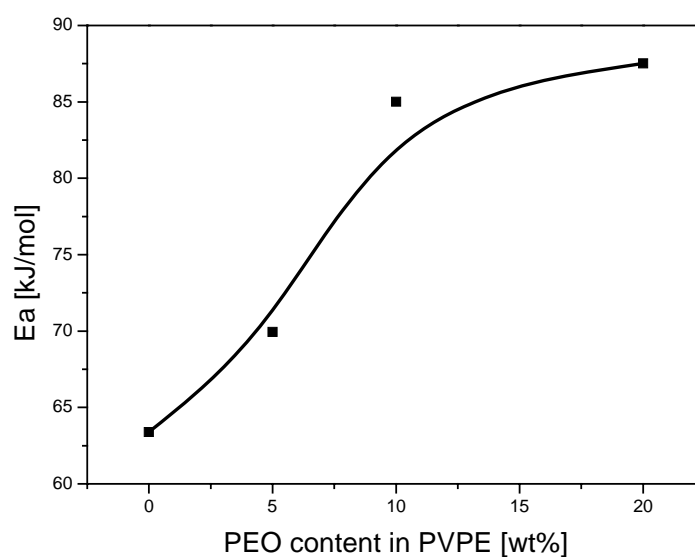
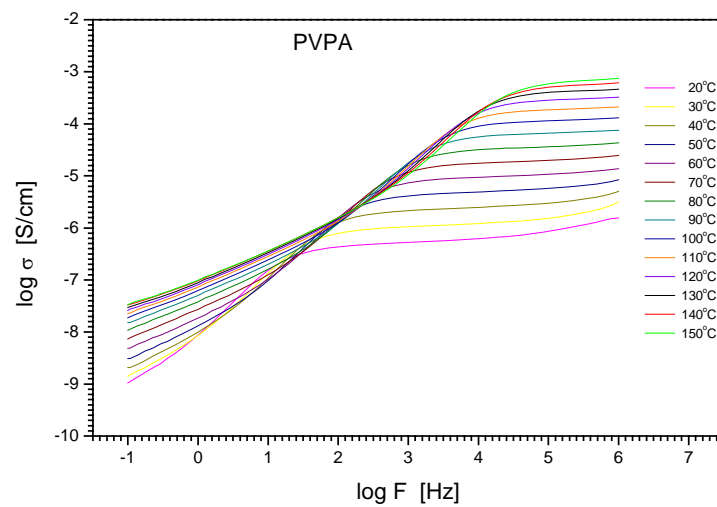


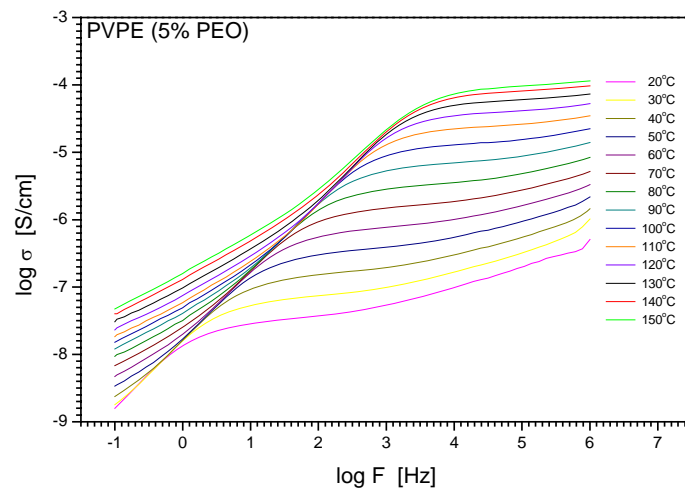
Figure 6.21: Activation energy of proton conduction in PVPEs with various PEO content.

These results can be understood in terms of the equation 5.1. According to Eq. 5.1, conductivity is determined by both the number of charge carriers and their mobility.

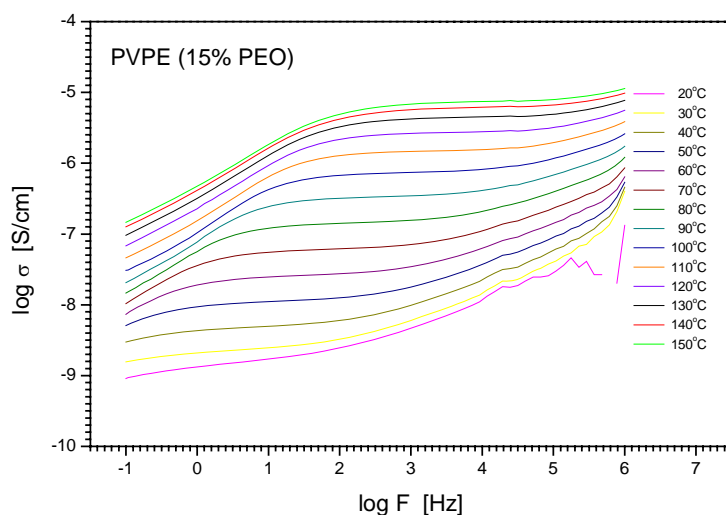
The effect of PEO content on proton mobility can be concluded from the AC conductivities (See Figure 6.22). We can see that with increasing PEO content, the plateau in the Bode plots shifts to low frequencies which directly shows that the mobility of protons decreases with increasing PEO content.



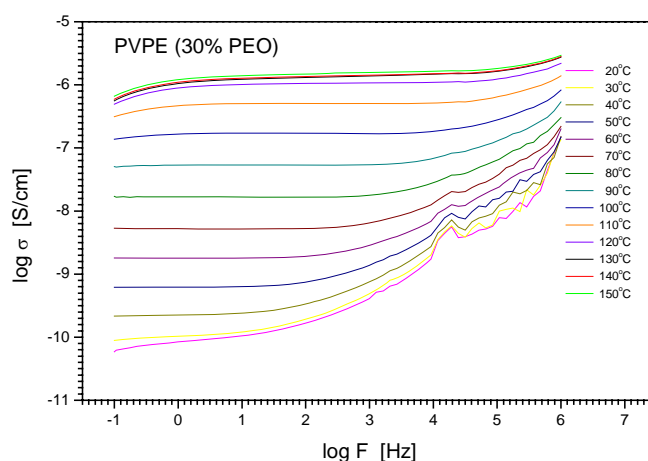
(a)



(b)



(c)



(d)

Figure 6.22: AC conductivities of (a) PVPA and (b-d) PVPEs in Bode plots.

From Figure 6.20 we can see that the proton conductivity of PVPE shows Arrhenius type behavior which means that the polymer chain motion has no notable effect on proton conductivity (the fast chain motion was detected by MAS NMR discussed in section 6.4). Figure 6.23 shows the Arrhenius plot of proton conductivities of PVPE (30% PEO) measured in a heating-cooling cycle. We can see that in the heating cycle, below 80 °C, proton conductivity still shows an Arrhenius

type behavior; however above 80 °C, the conductivity deviates from the linear part and increases faster with increasing temperature. According to the phase diagram of PVPE shown in Figure 6.12, the phase separation temperature (T_c) of PVPE (30% PEO) occurs at 80 °C. Below T_c , the blend is homogenous and shows Arrhenius type behavior as the PVPEs shown in Figure 6.20. When phase separation happens, the PEO content in the PVPA/PEO mixture decreases which consequently increases the proton conductivity. After phase separation, the $\log \sigma$ plot of the cooling cycle against reverse temperature becomes linear again. However, the activation energy decreases from 95kJ/mol to 78kJ/mol after phase separation because the PEO content in the homogenous PVPA/PEO phase decreases as a result of phase separation.

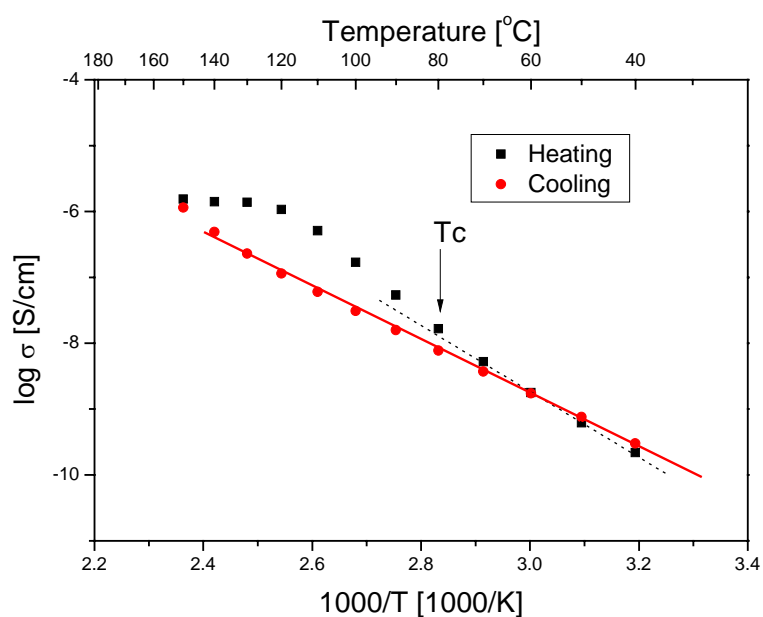
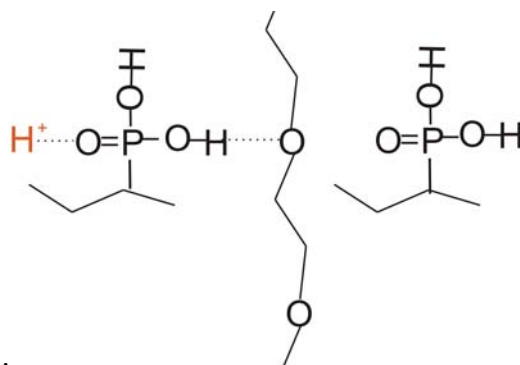


Figure 6.20: Arrhenius plot of proton conductivities of PVPE (30% PEO) measured in a heating-cooling cycle.

The reason why proton conduction activation energy increases with increasing PEO content is not sure yet. Some possibilities are discussed as following:

- 1) Proton transport in PVPA can be carried out by both rotation of side groups and hopping process as described in Scheme 6.1 and Scheme 6.3, respectively. However, the hopping process can be interrupted by PEO chains as shown in Scheme 6.6. Therefore proton conduction is based on the motion of phosphonic acid groups which leads to higher proton conduction activation energy.



Scheme 6.6: Hopping process interrupted by PEO chains in PVPE.

- 2) The average distance between phosphonic acid groups increases with increasing PEO content which makes it difficult for the phosphonic acid groups to find each other. This leads to increasing activation energy with increasing PEO content.
- 3) The hydrogen bonding between phosphonic acid group and PEO chain decreases the mobility of phosphonic acid groups.

CHAPTER 7

SUMMARY

ATRCP of DIPVBP and 4VP was carried out successfully in DMF at 90°C using the Cu^ICl/ HMTETA catalyst system. Typically, copper bromide-based ATRP catalysts provide better polymerization control than copper chloride-based systems. However, for different monomers, a unique combination of catalyst, ligand, solvent, temperature and reaction time have been applied for achieving optimal results. In this work, the reactivity ratio of DIPVBP (r_{DIPVBP}) and 4VP (r_{4VP}) were 0.69 and 1.17 respectively, calculated by the extended Kelen-Tudos method at high conversions. A series of poly(VBPA-stat-4VP)s with various copolymer compositions were obtained.

Proton conductivities of PVBPA and its copolymers were comprehensively investigated. The nominally anhydrous proton conductivities of the copolymers are very low and reach a minimum at a 1:1 molar ratio of proton donors and acceptor groups in the copolymer. The maximum value of activation energy (E_a) at a 1:1 molar ratio of proton donors and acceptor groups in the copolymer explains the minimum conductivity when only E_a is considered.

However, with the presence of humidity, even a small amount of water in these copolymers can significantly increase the proton conductivity because water can increase the charge carrier number density in the polymers and acts as a plasticizer. High proton conductivity ($>10^{-2}$ S/cm) can be obtained at a high relative humidity.

With water uptake higher than 2% in the polymer, protons can not see the underlying polymer structure anymore and proton conduction happens in water salvation which means proton conduction is based on water content.

By doping with H_3PO_4 in poly(VBPA-stat-4-VP), the proton conductivity is significantly increased. The proton conductivity of anhydrous Copo3 can reach 10^{-2} S/cm at 120°C with a doping level of $X=1.3$. With different phosphoric acid content, different temperature-dependences of proton conductivity have been observed due to the different proton conduction mechanisms involved.

P4VP was successfully grafted from the surface of SiO_2 nanoparticles using ATRP to obtain silica nanoparticles with a shell of basic polymeric layer. After blending these particles into the PVPA matrix, the self-condensation of the phosphonic acid groups decreases with increasing SiO_2 -Cl-4VP content, due to the acid-base interaction. However, proton conductivities in the composites decrease with increasing content of SiO_2 -Cl-4VP due to the increasing E_a and decreasing number of mobile protons. Water can increase the proton conductivities of these composites dramatically. At 85°C , under 80% RH, very high proton conductivity (0.5 S/cm) can be obtained with the composites although the amount of absorbed water in the sample is much lower as compared to PVPA homopolymer. Under these conditions, all the conductivities show Arrhenius type behavior; the activation energies for proton conduction are similar (~ 40 kJ/mol) because of the similar proton transport mechanism. The difference of proton conductivity, in this case, is mainly caused by different number of “free” protons.

A phase diagram of PVPA and PEO is plotted based on a DSC study and optical microscopy and homogeneous PVPA/PEO mixtures are prepared as proton-conducting polymer blends. Although the fast mobility of PEO chains was detected by ^1H -MAS-NMR, proton conductivity decreases with increasing PEO content in PVPA/PEO blends. PEO chains block the proton transport between the phosphonic acid groups and this blocking effect leads to increasing E_a for proton conduction with increasing PEO content in the blends.

CHAPTER 8

EXPERIMENTAL

8.1 Materials

N,N,N',N'',N'''-pentamethyldiethylenetriamine (PMDETA, 98%, Alfa Aesar) was freshly distilled prior to use. The monomer, 4-vinyl pyridine (4VP, 96%, Alfa Aesar) was distilled twice under reduced pressure over NaOH pellets and stored at -18 °C under Ar. Tris[2-(dimethylamino)ethyl]amine (Me₆TREN) was prepared according to the literature.^[1] Cu^IBr (99.999% Aldrich), Cu^ICl (99.999% Aldrich), vinylbenzyl chloride (97%, Aldrich), diisopropyl phosphite (98%, Alfa Aesar), potassium tert-butoxide (98%, Acros Organics), bromotrimethylsilane (BrSi(CH₃)₃, 98%, Acros Organics), silica dioxide (AEROSIL 300, Degussa) was dried at 120 °C under reduced pressure for 2 days, 4-(chloromethyl)phenyltrichlorosilane (Alfa Aesar), CuCl₂ (99.99%, Aldrich), toluene (extro dry, Aldrich), triethylamine (99%, Alfa Aesar) was refluxed over CaH₂ for 12 h and then distilled under Ar, N,N,N',N'',N''',N''''-hexamethyltriethylenetetramine (HMTETA, Aldrich), 2-bromo-2-methylpropionic acid bromide (Aldrich), ethyl 2-bromoisobutyrate (EBiB, 98%, Aldrich), 4-(chloromethyl)phenyltrichlorosilane (97%, Alfa Aesar) and the other chemicals were used as received.

8.2 Preparation of poly(vinylbenzyl phosphonic acid)

8.2.1 Synthesis of DIPVBP

The monomer diisopropyl-p-vinylbenzyl phosphonate was synthesized in a method adapted from the literature.^[2] Isopropyl phosphite (14.19g, 85.4 mmol) and vinylbenzyl chloride (10.72g, 70.25mmol) were dissolved in dry THF to obtain solution A. Potassium tert-butoxide (8.16g, 72.7mmol) was dissolved in 40ml dry THF and was then added dropwise to solution A during a period of 1 hour cooled occasionally with an ice bath. The mixture was kept stirring for another 2 hours at room temperature and then filtered, diluted with diethyl ether and washed with deionized water three times. The raw product was then purified by flash column chromatography on silica and the solvents were removed under reduced pressure. The total yield was 71.6%. ¹H NMR and ¹³C NMR were carried out on a 250MHz nuclear magnetic resonance spectrometer (Bruker, Germany) using CDCl₃ as solvent. The NMR spectra show that DIPVBP is successfully obtained: δ 7.28 (d, 2H, Ar-H), 7.21 (dd, 2H, Ar-H), 6.63 (dd, 1H, $\underline{\text{C}}\text{H}=\underline{\text{C}}\text{H}_2$), 5.69 (d, 1H, $\text{CH}=\underline{\text{C}}\text{H}_2$), 5.20 (d, $\text{CH}=\underline{\text{C}}\text{H}_2$), 4.57 (m, 2H, $\underline{\text{C}}\text{H}(\text{CH}_3)_2$), 3.06 (d, 2H, $\text{CH}_2\text{-P}$), 1.21 (d, 6H, CH_3), 1.16 (d, 6H, CH_3). ¹³C NMR: δ 23.69 (d, $\underline{\text{C}}\text{H}_3$), 23.98 (d, $\underline{\text{C}}\text{H}_3$), 33.60 (d, $\underline{\text{C}}\text{H}_2\text{-P}$), 70.53 (d, $\underline{\text{C}}\text{H-O}$), 113.41 ($\underline{\text{C}}\text{H}_2=\text{CH}$), 126.10 ($\underline{\text{C}}\text{H}=\text{CH}_2$), 130.0 (d, $\underline{\text{A}}\text{r-H}$), 131.6 (d, $\underline{\text{A}}\text{r-CH}_2$), 135.93 ($\underline{\text{A}}\text{r-CH}$), 136.42 ($\underline{\text{A}}\text{r-H}$).

8.2.2 Atom transfer radical polymerization of VBPE and hydrolysis of PVBPE

Poly(diisopropyl-p-vinylbenzyl phosphonate) (PVBPE) was synthesized by ATRP optimized from literature^[3]. A mixture of DIPVBP (5.66g, 2.0 mol), ethyl 2-bromoisobutyrate (0.0195g, 0.1mmol), HMTETA (0.1mmol), dry DMF (0.73g, 10mmol) was added to the flask and frozen in liquid nitrogen. $\text{Cu}^{\text{I}}\text{Cl}$ (0.0099g, 0.1mmol) was then added and the mixture was degassed by three freeze-pump-thaw cycles under Ar_2 . The reactions were carried out at 90°C . The obtained polymer was then isolated, purified, dried and then hydrolyzed using the method adapted from the literature.^[4] Into a round-bottom flask, PVBPE was dissolved in CH_2Cl_2 , excess of $\text{BrSi}(\text{CH}_3)_3$ (approximate 5 times of the phosphonate group) was added dropwise into the solution at 0°C . The mixtures were kept stirring under dry nitrogen for another 12h at room temperature. Then the solvent and volatile residues were evaporated under reduced pressure. Excess methanol was introduced and the mixture was stirred at room temperature for 12h. PVBPA was then obtained after purification.

The $^1\text{H-NMR}$ spectra of PVBPE and PVBPA are given in Figure 8.1. The fact that peaks with chemical shifts at 4.5ppm (CH, from isopropyl group) and 1.16 ppm, 0.97ppm (CH_3), respectively, are missing in the corresponding spectrum of PVBPA confirms that the ester groups are completely hydrolyzed. The molecular weight (M_w) of PVBPE is 31 kg/mol with a polydispersity of 2.5 according to the GPC results.

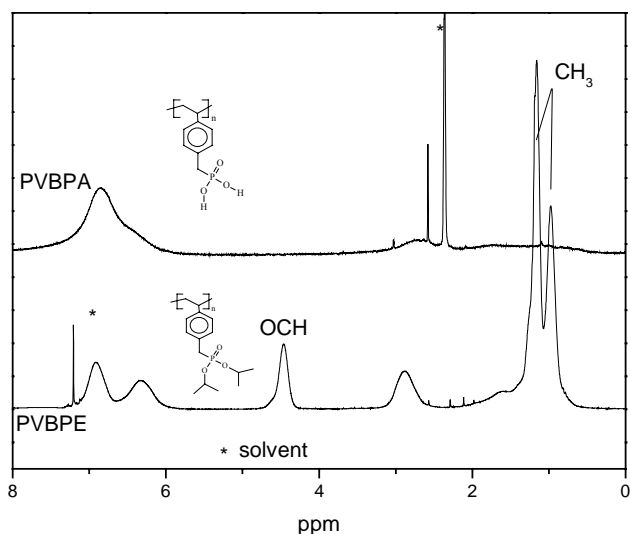


Figure 8.1: Solution ^1H -NMR spectra of PVBPE and PVBPA in CDCl_3 and DMSO-d_6 respectively.

8.3 Atom Transfer Radical Copolymerization

A mixture of 4-vinyl pyridine, DIPVBP, ethyl 2-bromoisobutyrate (0.0195g, 0.1mmol), PMDETA or HMTETA or Me_6TREN (0.1mmol), dry DMF (0.73g, 10mmol) was added to the flask and frozen in liquid nitrogen. Cu^1Cl (0.0099g, 0.1mmol) (Cu^1Br (0.0144g, 0.1mmol)) was then added and the mixture was degassed by three freeze-pump-thaw cycles under Ar. A little amount of the mixture was stringed into an Ar-degassed NMR tube and sealed. All the samples were freshly prepared and stored at -18°C shortly before the online ^1H NMR measurements and reactions were started at elevated temperatures (90°C , $\pm 0.1^\circ\text{C}$). In this work, the total monomer/initiator/catalyst/ligand/solvent molar ratio was fixed as 200/1/1/1/100. PMDETA, HMTETA and Me_6TREN were used as ligand for ATRP. All kinetic

measurements were carried out on a Bruker Avance 300 NMR spectrometer (Bruker Instruments, Germany).

8.4 Preparation of poly(vinylbenzyl phosphonic acid-stat-4VP)

The obtained copolymers can be hydrolyzed using the method adapted from the literature.^[4] Into a round-bottom flask, DIPVBP-stat-4VP copolymers were dissolved in CH₂Cl₂, excess of BrSi(CH₃)₃ (approximate 5 times of the phosphonate group) was added dropwise into the solution at 0°C. The mixtures were kept stirring under dry nitrogen for another 12h at room temperature. Then the solvent and volatile residues were evaporated under reduced pressure. Excess methanol was introduced and the mixture was stirred at room temperature for 12h. Poly(vinylbenzyl phosphonic acid-stat-4VP) was then obtained by precipitation in diethyl ether and drying under vacuum.

8.5 Initiator synthesis and immobilization

8.5.1 Synthesis and immobilization of (3-(2-Bromoisobutyryl)propyl)dimethyl chlorosilane

The processes were adjusted from the literature.^[5] 17.25g (75mmol) 2-Bromo-2-methylpropionic acid bromide was added dropwise to a stirred solution of allyl alcohol (4.35 g, 75 mmol) and triethylamine (9 g, 89.5 mmol) in dry dichloromethane (40 ml). After complete addition at 0 °C, the reaction mixture was stirred for additional 12 h at ambient temperature. The precipitated triethylamine

hydrochloride was then removed by filtration. The filtrate was diluted with diethyl ether, the solution was washed with 1% HCl, 5% NaHCO₃ and distilled water. The organic phase obtained was dried over sodium sulfate and filtered. The solvent was removed under reduced pressure and vacuum distillation of the crude product (65 °C/10 mbar) yielded 2-bromo-2-methylpropionic acid allyl ester as a colorless liquid.

¹H NMR (CDCl₃, 250 MHz): d = 5.72–5.98 (m, 1H, =CH-), 5.11–5.35 (m, 2H, =CH₂-), 4.56 (d, 2H, -CH₂O-), 1.97 (s, 1H, -CH₃-).

¹³C NMR (CDCl₃, 63 MHz): d = 170.6 (CO), 130.4 (=CH), 117.3 (=CH₂), 66.5 (CH₂O), 55.8 (C_{ter}), 29.4 (CH₃ and CH₂).

The obtained allylic ester was then mixed with 20 ml of freshly distilled dimethylchlorosilane. 40 mg of Pt/C (5 % Pt) were added and the mixture was refluxed for 15 h. The excess chlorosilane was removed under reduced pressure, yielding an oil. The oil was quickly filtered over anhydrous sodium sulfate to remove the residual catalyst to give chlorosilane initiator as colorless oil.

¹H NMR (CDCl₃, 250 MHz): d = 4.14–4.22 (m, 2H, -CH₂O-) 1.96 (s, 1H, -CH₃-), 1.64–1.80 (m, 2H, -CH₂-), 0.84 (m, 2H, -SiCH₂-), 0.46 (s, 6H, -Si(CH₃)₂-).

¹³C NMR (CDCl₃, 63 MHz): d = 170.4 (CO), 66.4 (CH₂O), 55.6 (C_{ter}), 29.4 and 20.8 (CH₃ and CH₂), 13.2 (SiCH₂), 2.1 (SiCH₃).

1g dried silica gel was suspended in 250 ml fresh distilled toluene. 10 ml dry TEA and 1.5 ml obtained chlorosilane initiator were added to the suspension. The reaction mixture was allowed to stand for 18h. After this the silica nanoparticles were isolated and washed with CH₂Cl₂ for three times, yield SiO₂-Br.

FTIR (with KBr): 2993, 2978, 2677, 2492, 1737

Elemental analysis: C 8.78%, H 1.70%.

Calculated graft density of initiator: 1.01 mmol/(g SiO₂).

8.5.2 Immobilization of 4-(chloromethyl)phenyltrichlorosilane

Silica gel was dried under vacuum at 120 °C for 48 hours to remove absorbed water. 3g dried silica nanoparticles were dispersed in the mixture of 300ml extra dry toluene and fresh distilled TEA (0.84 ml, 6mmol).

4-(chloromethyl)phenyltrichlorosilane (1.56g, 6mmol) was added dropwise to the suspension and the reaction mixture was kept on stirring for 48 hours. The functionalized silica particles were then isolated by centrifuging and washed with toluene for three times and finally dried under vacuum (10⁻² mbar) for 72 hours yielding 4.1g white powder (SiO₂-Cl).

FTIR (with KBr): 2988, 2936, 2740, 2682, 2504

Elemental analysis: C 17.25%, H 2.7%.

Calculated graft density of initiator: 2.48 mmol/(g SiO₂).

8.6 ATRP of 4-vinyl pyridine grafting from silica nanoparticles

A mixture of SiO₂-Br (or SiO₂-Cl), 4-vinyl pyridine, Me₆TREN, methanol (10 ml), deionized water (10 ml) was added to the flask and frozen in liquid nitrogen. Cu^ICl and CuCl₂ were then added and the mixture was degassed by three freeze-pump-thaw cycles under Argon. In this work, the total

monomer/initiator/CuCl/CuCl₂/ Me₆TREN molar ratio was fixed as 200/1/0.7/0.3/1. The polymerizations were carried out at 30°C for 12 hours. The grafted silica particles were ultrafiltrated in methanol for three times. The ultrafiltration membrane has a cutoff of 100 kDa.

8.7 Characterization

8.7.1 Gel Permeation Chromatography (GPC)

GPC measurements were conducted to determine the molecular weights of copolymers on the basis of polystyrene standards. Copolymers prepared by experiments 5-7 were eluted with DMF at 60 °C using a Waters 515 liquid chromatograph pump (1.0 ml/min) and three Polymer Standards Service columns (GRAM, 10000, 1000, 100). Copolymers prepared by experiments 8 and 9 were eluted with a mixture of 80% aqueous solution (0.5M Na₂SO₄, 0.5M CH₃COOH) and 20% CH₃CN at 23 °C using a Waters 515 liquid chromatograph pump (1.0 ml/min) and three Polymer Standards Service columns (TSK Gel, G6000, G5000, G3000).

8.7.2 Nuclear Magnetic Resonance (NMR)

Solution ¹H-NMR spectra were recorded at a Bruker AXS250 spectrometer.

³¹P MAS NMR experiments were performed at LARMOR frequencies of 202.45 MHz, using a BrukerASX500 spectrometer, equipped with a 2.5 mm fast MAS probe. The spinning frequency was 25 kHz.

^1H MAS NMR experiments were carried out at 500.13 MHz (BrukerASX500 spectrometer) or 850 MHz (Bruker Avance II 850 spectrometer), with the spinning frequency of 25 kHz and 30 kHz, respectively.

Spectra were referenced with respect to tetramethyl silane (^1H) or phosphoric acid (85%, ^{31}P).

8.7.3 Thermal Gravimetric Analysis (TGA)

TGA was performed on a TGA/SDTA851 (METTLER TOLEDO) under N_2 with a heating rate of 1 K/min or 10K/min.

8.7.4 Differential Scanning Calorimetric (DSC)

DSC was performed on a DSC 822 (METTLER TOLEDO) under N_2 with a heating rate of 1 K/min or 10 K/min.

8.7.5 Optical microscopy

The optical microscopy and polarized optical microscopy images were all recorded on a Zeiss Axiophot microscope equipped with a CCD camera (AxioCam). All the samples were measured on a heating plate protected by dry nitrogen atmosphere. The heating rate was set to 10K/min.

8.7.6 Elemental analysis (EA)

EA was measured on a Vario EL CUBE (Elementar, Germany).

8.7.7 Infrared spectroscopy

FT-IR spectra were obtained on a Nicolet 730 FTIR spectrometer. All pellets were measured in the pellet form with KBr.

8.7.8 Electron microscopy

Scanning electron microscopy (SEM) images were obtained by collecting the secondary electrons emitted from the sample after scanning a focused electron beam onto the sample. SEM images were obtained on field emission SEM (LEO 1530 “Gemini”) which allows obtaining images with high magnification at low operating voltages.

Transmission electron microscopy (TEM) images were obtained on a TEM (FEI Tecnai F200).

8.7.9 Proton Conductivity Measurements

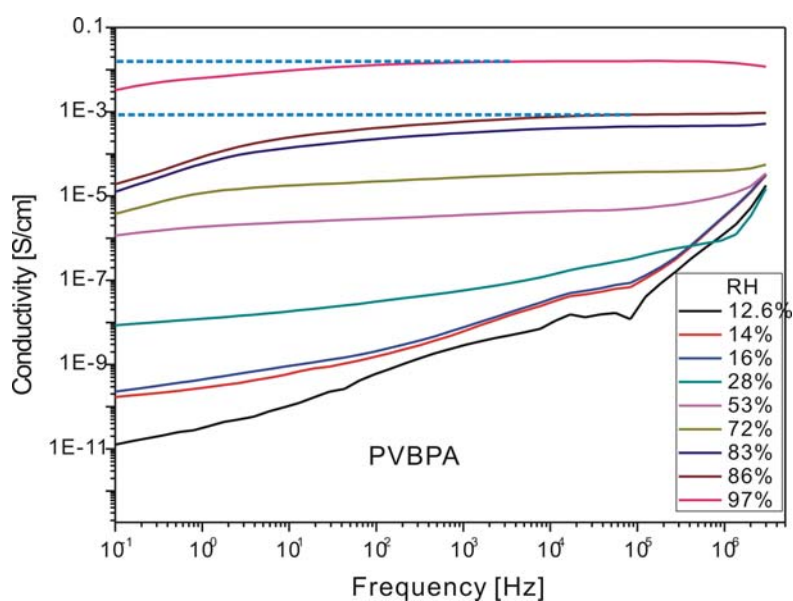
The proton conductivity was measured by dielectric spectroscopy in a two-electrode geometry using an SI 1260 impedance/gain-phase analyzer in the frequency range of 10^{-1} - 10^{-6} Hz.

The humidity of air during data acquisition was set by mixing dry nitrogen with humidity saturated nitrogen. The relative humidity (RH) was measured using a Sensiron SHT15 sensor.

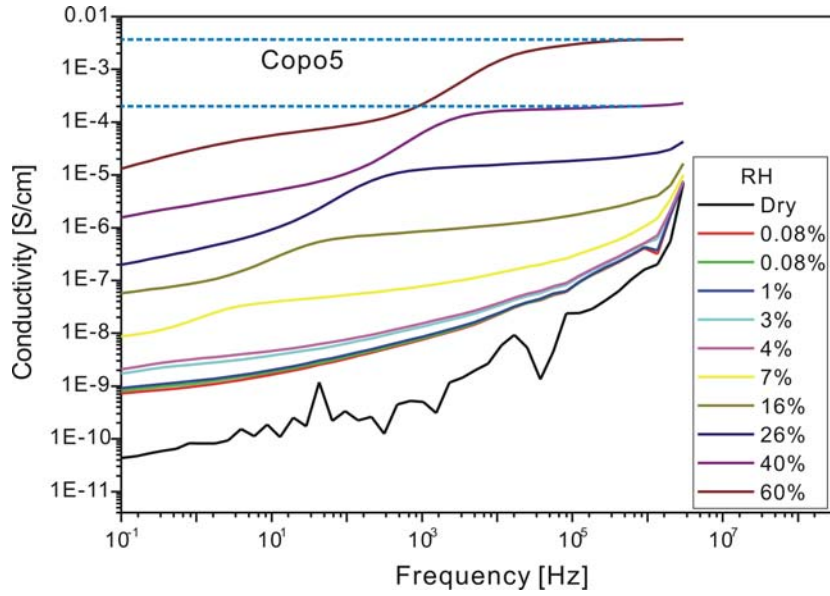
For dry-condition proton conductivity measurements, all the samples were dried at 50°C under vacuum for 4 days prior to the measurements. Completely dry N₂ was used to flush the samples during the measurements.

The samples for conductivity measurements were pressed to tablets and contacted by E-tek[®] and stainless steel electrodes.

Proton conductivities were evaluated from both Cole-Cole plots^[6] and Bode plots. Here are two examples of the bode plots. All curves have a specific frequency region in which AC conductivity is independent from frequency (plateau). (See Figure 8.2) The extrapolation (the blue dash lines in Fig.8.2) of the plateau to frequency $\omega=0$ defines the value of DC conductivity. The precision of this method was checked by comparison of the results with values obtained via Cole-Cole plot. The data obtained by both approaches are in good agreement. (See Figure 8.3)



(a)



(b)

Figure 8.2: Bode plots of AC conductivities of a) PVBPA and b) Copo5 under various RHs.

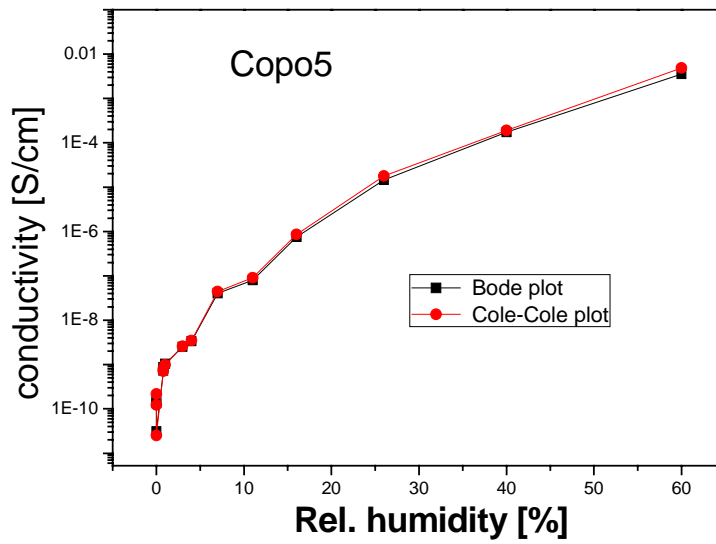


Figure 8.3: Comparison of data obtained by Bode plot and Cole-Cole plot.

REFERENCES

Chapter 1

- (1) Starz, K. A.; Auer, E.; Lehmann, T.; Zuber, R. *Journal of Power Sources*. **1999**, *84*, 167.
- (2) Johnson, Za; Pai, Andy. *Proceedings of the Intersociety Energy Conversion Engineering Conference*. **1999**, *34th*, 379.
- (3) Appleby, A. J. *Philosophical Transactions of the Royal Society of London, Series A: Mathematical, Physical and Engineering Sciences*, **1996**, *354*, 1681.
- (4) Singhal, S. C. *Industrial Ceramics*, **2008**, *28*, 53.
- (5) Van den Broeck, Hugo. *Fuel Cell Syst.* **1993**, 245.
- (6) Bischoff, Manfred. *Journal of Power Sources*. **2006**, *160*, 842.
- (7) kumura, Minoru. *Materials Integration*. **2004**, *17*, 17.
- (8) Bolufer, P. *Energia*. **2008**, *204* 72.
- (9) Schiraldi, David A.; Zhou, Chun; Zawodzinski, Thomas A. *Abstracts of Papers, 235th ACS National Meeting, New Orleans, LA, United States, April 2008*, 6.
- (10) Stoler, Emily J.; Nair, Bindu R.; Kovar, Robert F.; Ofer, David. *Proceedings of the Intersociety Energy Conversion Engineering Conference* **2001**, *36th (Vol. 2)*, 975.
- (11) Tang, H. L.; Pan, M.; Wang, F. *Journal of Applied Polymer Science*. **2008**, *109*, 2671.
- (12) Lee, Wonmok; Kim, Haekyoung; Lee, Hyunjung. *Journal of Membrane Science*. **2008**, *320*, 78.
- (13) Schauer, Jan. *Current Trends in Polymer Science*. **2006**, *10*, 19.
- (14) Grot, W. G. F.; Munn, G. E.; Walmsley, P. N.; *Presented at the Electrochemical Society Meeting, Houston, TX, May 7-11, 1972*, paper no. 154

- (15) Cable, K. M. *Tailoring Morphology-Property Relationships in Perfluorosulfonate Ionomers. Ph.D. Dissertation*, University of Southern Mississippi, **1996**
- (16) Kreuer, K. D. J. *Membr. Sci.* **2001**, *185*, 29.
- (17) Gierke, T. D.; Munn, G. E.; Wilson, F. C. *J. Polym. Sci., Polym. Phys.* **1981**, *19*, 1687
- (18) Fujimura, M; Hashimoto, T.; Kawai, H. *Macromolecules*, **1981**, *14*, 1309.
- (19) Litt, M. H. *Polym. Prepr.* **1977**, *38*, 80.
- (20) Rubatat, L.; Rollet, A. -L.; Gebel, G.; Diat, O. *Macromolecules*, **2002**, *35*, 4050.
- (21) Schmidt-Rohr K.; Chen, Q. *Nature Materials*, **2008**, *7*, 75
- (22) Mauritz, K. A., Moore, R. B. *Chemical Reviews.* **2004**, *104*, 4535.
- (23) Wei, J.; Stone, C.; Steck, A. E. *U.S Patent*, **1995**, 5422411.
- (24) Serpico, J. M.; Ehrenberg, S. G.; Fontanella, J. J.; Jiao, X.; Perahia, D.; McGrady, K. A.; Sanders, E. H.; Kellogg, G. E.; Wnek, G. E. *Macromolecules* **2002**, *35*, 5916.
- (25) Hickner Michael A; Ghassemi Hossein; Kim Yu Seung; Einsla Brian R; McGrath James E. *Chemical reviews*, **2004**, *104*, 4587.
- (26) Genies, C.; Mercier, R.; Sillion, B.; Cornet, N.; Gebel, G.; Pineri, M. *Polymer* **2001**, *42*, 359.
- (27) Einsla, B. R.; Hong, Y. T.; Kim, Y. S.; Wang, F.; Gunduz, N.; McGrath, J. E. *J. Polym. Sci., Part A: Polym. Chem.* **2004**, *42*, 862.
- (28) Kopitzke, R. W.; Linkous, C. A.; Nelson, G. L. *Polym. Degrad. Stab.* **2000**, *67*, 335.
- (29) Kobayashi, T.; Rikukawa, M.; Sanui, K.; Ogata, N. *Solid State Ionics* **1998**, *106*, 219.
- (30) Powers, E. J.; Serad, G. A. *High Performance Polymers: Their Origin and Development*; Elsevier: Amsterdam, **1986**, 355.

- (31)Noaki, Y.; Shiroki, H. Ext. Abstr., *183rd Meeting of the Electrochemical Society*, **1993**, *93*, 1293
- (32)Kreuer, K. D.; Paddison, S. J.; Spohr, E.; Schuster, M. *Chem. Rev.*, **2004**, *104*, 4637
- (33)Daycock, J.T.; Jones, G.P.; Evans, J.R.N.; Thomas, J.M. *Nature* **1968**, 218, 673.
- (34)Kawada, A.; McGhie, A.R.; Labes, M.M. *J. Chem. Phys.* **1970**, *52*, 3121.
- (35)Dippel, T.; Kreuer, K. D.; Lassègues, J. C.; Rodriguez, D. *Solid State Ionics* **1993**, *61*, 41.
- (36)Buckley, A.; Stuetz, D. E.; Serad, G. A. *Encyclopedie des polymeres*, vol. *11*, 572.
- (37)Daletou, M. K.; Gourdoupi, N.; Kallitsis, J. K. *Journal of Membrane Science*. **2005**, *252*, 115.
- (38)Pu, H.; Meyer, W. H.; Wegner, G. *Journal of Polymer Science, Part B: Polymer Physics*. **2002**, *40*, .663.
- (39)Jiang, Fengjing; Pu, Hongting; Meyer, Wolfgang H.; Guan, Yisi; Wan, Decheng. *Electrochimica Acta*. **2008**, *53*, 4495.
- (40)Schuster, M.; Rager, T.; Noda, A.; Kreuer K. D.; Maier, J. *Fuel Cells*, **2005**, *5*, 355.
- (41)Kreuer, K. D.; *J. Membr. Sci.*, **2001**, *185*, 29.
- (42)Schuster, M.; Meyer, W. H.; Wegner, G.; Herz, H. G.; Ise, M.; Kreuer K. D.; and Maier J. *Solid State Ionics*, **2001**, *145*, 85.
- (43)Schuster, M. F. H.; Meyer, W. H.; Schuster, M.; Kreuer, K. D. *Chem. Mater.*, **2004**, *16*, 329.
- (44)Schuster M. F. H.; and Meyer, W. H. *Annu. Rev. Mater. Res.*, **2003**, *33*, 233.
- (45)Perrson J. C.; Jannasch, P. *Chem. Mater.*, **2003**, *15*, 3044.
- (46)Steininger, H.; Schuster, M.; Kreuer, K. D.; Kaltbeitzel, A.; Bingöel, B.; Meyer, W. H.; Schauff, S.; Brunklaus, G.; Maier, J.; Spiess, H. W. *Physical chemistry Chemical Physics*, **2007**, *9*, 1764.

- (47) Bozkurt, A.; Meyer, W. H. *Solid State Ionics*. **2001**, *138*, 259.
- (48) Bozkurt, A.; Meyer, W.H.; Gutmann, J.; Wegner, G. *Solid State Ionics* **2003**, *164*, 169.
- (49) Bingöel, B. *Synthesis and characterization of Poly(vinylphosphonic acid) for Proton Exchange Membranes in Fuel Cells*, PhD thesis, Mainz, **2007**
- (50) Kreuer K. D.; Paddison, S. J.; Spöhr, E.; Schuster, M. *Chemical Review*, **2004**, *104*, 4637
- (51) Tuckerman, M.; Laasonen, K.; Sprik, M.; Parrinello, M. Zurich Res. Lab., IBM Res. Div., Rüschlikon, Switz. *Journal of Chemical Physics* **1995**, *103*, 150.
- (52) Tuckerman, M. E.; Marx, D.; Klein, M. L.; Parrinello, M. *Science*. **1997**, *275*, 817.
- (53) Agmon, N. *Chem. Phys. Lett.* **1995**, *244*, 456.
- (54) Kreuer, K. D. *Solid State Ionics*. **2000**, *136-137*, 149.
- (55) Münch, W.; Kreuer, K. D.; Silvestri, W.; Maier, J.; Seifert, G. *Solid State Ionics* **2001**, *145*, 437.
- (56) Kreuer, K. D.; Fuchs, A.; Ise, M.; Spaeth, M.; Maier, J. *Electrochim. Acta* **1998**, *43*, 1281.
- (57) Munson, R. A. *J. Phys. Chem.* **1964**, *68*, 3374.

Chapter 2

- (1) Guenday, S. T.; Bozkurt, A.; Meyer, H.M.; Wegner, G. *J. Appl. Polym. Sci., Polym. Phys.* **2006**, *44*, 3315.
- (2) Kufaci, M.; Bozkurt, A.; Tuelue, M. *Solid State Ionics*. **2006**, *17*, 1003.
- (3) Bozkurt, A.; Meyer, W.H.; Gutmann, J.; Wegner, G. *Solid State Ionics*. **2003**, *164*, 169.
- (4) Sevil, F.; Bozkurt, A. *J. Phys. Chem. Solids*. **2004**, *65*, 1659.
- (5) Jiang, F.; Pu, H.; Meyer, W. H.; Guan, Y.; Wan, D. *Electrochimica Acta*. **2008**, *53*, 4495.

Chapter 3

- (1) Gao, H.; Matyjaszewski, K. *Macromolecules*. **2007**, *40*, 399.
- (2) Gao, H.; Ohno, S.; Matyjaszewski, K. *J. Am. Chem. Soc.* **2006**, *128*, 15111.
- (3) Adams, D. J.; Butler, M. F.; Weaver, A. C. *Langmuir*. **2006**, *22*, 4534.
- (4) Matyjaszewski, K.; Nakagawa, Y.; Gaynor, S. G. *Macromol. Rapid Commun.* **1997**, *18*, 1057.
- (5) Coessens, V.; Nakagawa, Y.; Matyjaszewski, K. *Polym. Bull.* **1998**, *40*, 135.
- (6) Matyjaszewski, K.; Ziegler, M. J.; Arehart, S. V.; Greszta, D.; Pakula, T. J. *Phys. Org. Chem.* **2000**, *13*, 775.
- (7) Greszta, D.; Matyjaszewski, K.; Pakula, T. *Polym. Prepr. (Am. Chem. Soc., Div. Polm. Chem.)* **1997**, *38*, 709.
- (8) Kotani, Y.; Kamigaito, M.; Sawamoto, M. *Macromolecules*. **1998**, *31*, 5582.
- (9) Zhao, Y.; Shuai, X.; Chen, C.; Xi, F. *Macromolecules*. **2004**, *37*, 8854.
- (10) Runge, M. Brett; Dutta, Samrat; Bowden, Ned B. *Macromolecules*. **2006**, *9*, 498.
- (11) Whittaker, Michael R.; Urbani, Carl N.; Monteiro, Michael J. *J. Am. Chem. Soc.* **2006**, *128*, 11360.
- (12) Peleshanko, S.; Gunawidjaja, R.; Petrash, S.; Tsukruk, V. V. *Macromolecules*. **2006**, *39*, 4756.
- (13) Patten, T.; Matyjaszewski, K. *Adv. Mater.* **1998**, *10*, 901.
- (14) Jiang, G.; Wang, L.; Chen, W. *European Polymer Journal*. **2006**, *42*, 3333.
- (15) Chen, Y.; Shen, Z.; Barriau, E.; Kautz, H.; Frey, H. *Biomacromolecules*. **2006**, *7*, 919.
- (16) Arehart, S. V.; Matyjaszewski, K. *Macromolecules*. **1999**, *32*, 2221.
- (17) Uegaki, H.; Kontani, Y.; Kamigaito, Sawamoto, M. *Macromolecules*. **1998**, *31*, 6756.
- (18) Mayo, F. R.; Lewis, F. M.; *J. Am. Chem. Soc.* **1944**, *66*, 1594.
- (19) Teoh, R. L.; Guice, K. B.; Loo, Y. *Macromolecules*. **2006**, *39*, 8609.
- (20) Nguyen, S.; Marchessault, R. H. *Macromolecules*. **2005**, *38*, 290.

- (21) Haddleton, D. M.; Crossman, M. C.; Hunt, K. H.; Topping, C.; Waterson, C.; Suddaby, K. G. *Macromolecules*. **1997**, *30*, 3992.
- (22) Ziegler, M. J.; Matyjaszewski, K. *Macromolecules*. **2001**, *34*, 415.
- (23) Matyjaszewski, K. *Macromolecules*. **1998**, *31*, 4710.
- (24) Steininger, H.; Schuster, M.; Kreuer, K. D.; Maier, J. *Solid State Ionics*. **2006**, *177*, 2457.
- (25) Li, S.; Zhou, Z.; Abernathy, H.; Liu, M.; Li, W.; Ukai, J.; Hase, K.; Nakanishi, M. *J. Mater. Chem.* **2006**, *16*, 858.
- (26) Yamada, M.; Honma, I. *Polymer*. **2005**, *46*, 2986.
- (27) Bingoel, B.; Meyer, W. H.; Wagner, M.; Wegner, G. *Macromol. Rapid Commun.* **2006**, *27*, 1719.
- (28) Fineman, M.; Ross, S. D. *J. polym. Sci.* **1950**, *5*, 259.
- (29) Fineman, M.; Ross, S. D. *J. polym. Sci. Part A: Gen. Pap.* **1964**, *2*, 1687.
- (30) Kelen, T.; Tudos, F. *J. Macromol. Sci. Chem.* **1975**, *9*, 1.
- (31) Kelen, T.; Tudos, F.; Turcsanyi.; Kennedy, J. J. *Macromol. Sci. Chem.* **1977**, *5*, 3047.
- (32) Kelen, T.; Tudos, F. *J. Macromol. Sci. Chem.* **1981**, *16*, 1238.
- (33) Tidwell, P. W.; Mortimer, G. A. *J. polym. Sci. Part A: Gen. Pap.* **1965**, *3*, 369.
- (34) Mao, R.; Huglin, M. B. *Polymer*. **1993**, *34*, 1709.
- (35) Mahdavian, A. R.; Abdollahi, M.; Mokhtabad, L.; Bijianzadeh, H. R.; Ziaee, F. *J. polym. Sci.* **2006**, *101*, 2062.
- (36) Cui L., Lattermann G. *Macromol. Chem. Phys.* **2002**, *203*, 2432.
- (37) Tsarevsky, N.; Braunecker, W. A.; Brooks, S. J.; Matyjaszewski, K. *Macromolecules*. **2006**, *39*, 6817.

Chapter 4

- (1) Greenspan, I. *Journal of Research of the National Bureau of Standards A.* **1977**, *81*, 89.

- (2) Funke, K. *Solid State Ionics* **1986**, 18-19, 183.
- (3) Funke, K.; Hoppe, R. *Solid State Ionics* **1990**, 40, 200.
- (4) Fontanella, J. J.; Wintersgill, M. C.; Wainright, J. S.; Savinell, R. F.; Litt, M. *Electrochimica Acta*, 1998, **43**, 1289.
- (5) Rikukawa, M.; Morita, J.; Sanui, K.; Ogata, N.; Proceedings of the Fifth International Symposium on Polymer Electrolytes, Upsala, **1996**, P.32
- (6) Ward, I. M. *Mechanical properties of solid polymers (second edition)*. ISBN: 0 471 90011 7.
- (7) Williams M. L.; Landel, S. F.; Ferry, J. D. *JACS*, **1995**, 77, 3701.
- (8) Schuster, M. *Dissertation*. Mainz **2002**.

Chapter 5

- (1) Bingoel, B. *Synthesis and characterization of poly(vinylphosphonic acid) for Proton Exchange Membranes in Fuel Cells*, PhD thesis, Mainz, **2007**
- (2) Tang, H.; Pan, M. *Journal of Physical Chemistry C*. **2008**, 112, 11556.
- (3) Sahu, A. K.; Selvarani, G.; Pitchumani, S.; Sridhar, P.; Shukla, A. K. *Journal of the Electrochemical Society*. **2007**, 154, B123.
- (4) Kim, H.; Chang, H. *Journal of Membrane Science* **2007**, 288, 188.
- (5) Su, Y.; Wei, T.; Hsu, C.; Liu, Y.; Sun, Y.; Lai, J. *Desalination*. **2006**, 200, 656.
- (6) Shao, Z.; Joghee, P.; Hsing, I. *Journal of Membrane Science*. **2004**, 229, 43.
- (7) Staiti, P.; Arico, A. S.; Baglio, V.; Lufrano, F.; Passalacqua, E.; Antonucci, V. *Solid State Ionics*. **2001**, 145, 101.
- (8) Miyake, N.; Wainright, J. S.; Savinell, R. F. *Journal of the Electrochemical Society*. **2001**, 148, A905.
- (9) Miyake, N.; Wainright, J. S.; Savinell, R. F. *Journal of the Electrochemical Society*. **2001**, 148, A898.
- (10) Habicht, J.; Park, I. *Materials Science and Engineering*. **1999**, C 8-9, 291.
- (11) Prucher, O.; Ruehe, J. *Macromolecules* **1998**, 31, 592

- (12) Tovar, G.; Paul, S.; Knoll, W.; Prucker, O.; Ruehe, J. *Supramol. Sci.* **1995**, *2*, 89.
- (13) Prucker, O.; Schimmel, M.; Tovar, G.; Knoll, W.; Ruehe, J. *Adv. Mater.* **1998**, *10*, 1073.
- (14) Huang, X.; Wirth, M. J. *Macromolecules* **1999**, *32*, 1694.
- (15) Zhao, B.; Brittain, W. J. *J. Am. Chem. Soc.* **1999**, *121*, 3557.
- (16) Husseman, M.; Malmstrom, E. E.; McNamara, M.; Mate, M.; Mecerreyes, D.; Benoit, D. G.; Hedrick, J. L.; Mansky, P.; Huang, E.; Russell, T. P.; Hawker, C. J. *Macromolecules* **1999**, *32*, 1424.
- (17) Matyjaszewski, K.; Miller, P. J.; Shukla, N.; Immaraporn, B.; Gelman, A.; Luokala, B. B.; Siclovan, T. M.; Kickelbick, G.; Vallant, T.; Hoffmann, H.; Pakula, T. *Macromolecules* **1999**, *32*, 8716.
- (18) Von Werne, T.; Patten, T. E. *J. Am. Chem. Soc.* **1999**, *121*, 7409.
- (19) De Boer, B.; Simon, H. K.; Werts, M. P. L.; Van der Vegte, E. W.; Hadziioannou, G. *Macromolecules* **2000**, *33*, 349.
- (20) Kim, J.B.; Bruening, M. L.; Baker, G. L. *J. Am. Chem. Soc.* **2000**, *122*, 7616.
- (21) Ejaz, M.; Yamamoto, S.; Ohno, K.; Tsujii, Y.; Fukuda, T. *Macromolecules* **1998**, *31*, 5934.
- (22) Yamamoto, S.; Ejaz, M.; Tsujii, Y.; Matsumoto, M.; Fukuda, T. *Macromolecules* **2000**, *33*, 5602.
- (23) Yamamoto, S.; Ejaz, M.; Tsujii, Y.; Fukuda, T. *Macromolecules* **2000**, *33*, 5608.
- (24) Yamamoto, S.; Tsujii, Y.; Fukuda, T. *Macromolecules* **2002**, *35*, 6077.
- (25) Urayama, K.; Yamamoto, S.; Tsujii, Y.; Fukuda, T.; Neher, D. *Macromolecules*. **2000**, *35*, 9459.
- (26) Zhao, B.; Brittain, W. J. *Prog. Polym. Sci.* **2000**, *25*, 677.
- (27) Pyun, J.; Kowalewski, Y.; Matyjaszewski, K. *Macromol. Rapid. Commun.*

- 2003**, 24, 1043.
- (28) Edmondson, S.; Osborne, V. L.; Huck, W. T. S. *Chem. Soc. Rev.* **2004**, 33, 14.
- (29) Matyjaszewski, K.; Xia, J.; *Chem. Rev.* **2001**, 101, 2921.
- (30) Chiefari, J.; Chong, Y. K.; Ercole, F.; Krstina, J.; Jeffrey, J.; Le, P. T.; Mayadunne, R. T. A.; Meijs, G. F.; Moad, C. L.; Moad, G.; Rizzardo, E.; Thang, S. H. *Macromolecules* **1998**, 31, 5559.
- (31) Tsarevsky, N.; Braunecker, W. A.; Brooks, S. J.; Matyjaszewski, K. *Macromolecules*. **2006**, 39, 6817.
- (32) Matyjaszewski, K.; Miller, P. J.; *Macromolecules*. **1999**, 32, 8716.

Chapter 6

- (1) Lee, Y. J.; Murakhtina, T.; Sebastiani, D.; Spiess, H. W. *Journal of the American Chemical Society*. **2007**, 129, 12406.
- (2) Jiang, F.; Kaltbeitzel, A.; Meyer, W. H.; Pu, H.; Wegner, G. *Macromolecules*. **2008**, 41, 3081.
- (3) Bjerrum, N. *Science*. **1952**, 115
- (4) Bingöel, B. *Synthesis and characterization of Poly(vinylphosphonic acid) for Proton Exchange Membranes in Fuel Cells, PhD thesis, Mainz, 2007*
- (5) Geen, H.; Titman, J. J.; Gottwald, J.; Spiess, H. W. *Chem. Phys. Lett.*, **1994**, 227, 79
- (6) Gottwald, J.; Demco, D. E.; Graf, R.; Spiess, H. W. *Chem. Phys. Lett.*, **1995**, 243, 314
- (7) Schnell, I.; Brown, S. P.; Low, H. Y.; Ishida, H.; Spiess, H. W. *J. Am. Chem. Soc.*, **1998**, 120, 11784.
- (8) Haeblerlen, U. ‘ *Advances in Magnetic Resonance Suppl. 1* ’ Academic Press: San Diego, CA, **1976**
- (9) Ishida, H.; Low, H. Y. *Macromolecules*, **1997**, 30, 1099
- (10) Feike, M.; Demco, D. E.; Graf, R.; Gottwald, J.; Hafner, S.; Spiess, H. W.

Journal of Magnetic Resonance A. **1996**, 122, 21.

(11) Demco, D. E.; Gottwald, J.; Graf, R.; Feike, M.; Hafner, S.; Spiess, H. W.

EPF/AMPERE Workshop, September 25–26, Mainz, 1995.

(12) Sommer, W.; Gottwald, J.; Demco, D. E.; Spiess, H. W. *Journal of Magnetic*

Resonance A. **1995**, 113, 131.

Chapter 8

(1) Ciampolini, M.; Nardi, N. *Inorg. Chem.* **1966**, 5, 41-44.

(2) Wyman, P.; Crook, V.; Hunt, B. J.; Ebdon, J. *Designed Monomers and Polymers*. **2004**, 7, 01-309.

(3) Markova, D.; Kumar, A.; Muellen, K.; Klapper, M. *Preprints of Symposia - American Chemical Society, Division of Fuel Chemistry*. **2006**, 51, 651.

(4) Huang, J.; Matyjaszewski, K. *Macromolecules*. **2005**, 38, 3577.

(5) Ramakrishnan, A.; Dhamodharan, R.; Ruehe, J. *Macromolecular Rapid Communications*. **2002**, 23, 612.

(6) Powles, J. G. *Proc. Phys. Soc.* 1951, B **64**, 81.